The White Dwarf Initial-Final Mass Relation: Ultramassive White Dwarfs Ejected from Young Open Star Clusters

by

David Ross Miller

B.Sc. Physics, Simon Fraser University, 2020

A THESIS SUBMITTED IN PARTIAL FULFILLMENT
OF THE REQUIREMENTS FOR THE DEGREE OF

Master of Science

in

THE FACULTY OF GRADUATE AND POSTDOCTORAL STUDIES

(Astronomy)

The University of British Columbia

(Vancouver)

August 2022

The following individuals certify that they have read, and recommend to the Faculty of Graduate and Postdoctoral Studies for acceptance, the thesis entitled:

The White Dwarf Initial-Final Mass Relation: Ultramassive White Dwarfs Ejected from Young Open Star Clusters

submitted by **David Ross Miller** in partial fulfillment of the requirements for the degree of **Master of Science** in **Astronomy**.

Examining Committee:

Harvey Richer, Professor, Physics and Astronomy, UBC
Supervisor

Jeremy Heyl, Professor, Physics and Astronomy, UBC
Supervisory Committee Member

Abstract

Intermediate mass stars either end their lives as a white dwarf (WD) or a neutron star, depending almost entirely on star's mass. The mass limit between these two fates is critical for a number of astrophysical quantities, including galactic heavy element enrichment and compact object formation rates. Unfortunately, this mass limit is not well constrained, with different methodologies suggesting this limit could reasonably be anywhere from 8 to 12 $M_{\odot}$. The mass limit for WD production can be constrained by developing the WD initial-final mass relation (IFMR). Determining the mass of a WD precursor requires identifying WDs that are members of young open star clusters. Extensive searches of open clusters have left a significant gap in the high mass region of the IFMR, this dearth may be the result of the WDs receiving a small velocity kick in the late stages of stellar evolution. In this work, we search the Gaia DR2 and EDR3 databases for ultramassive white dwarfs whose kinematics suggest they may have escaped from young open star clusters. Using a series of methods, we identified 13 candidate ultramassive WDs whose kinematics agreed with past cluster membership. Each of these candidates was followed up with spectroscopy to determine the WDs atmospheric parameters and better assess potential cluster membership. We determine that three of these candidates are high-confidence cluster members, four are questionable members, and the remaining six are non-members. The three high-confidence cluster member WDs are each more massive than any previous cluster WD known, with some of the most massive known progenitors. The most massive of these WDs has a progenitor of approximately 8.5 $M_{\odot}$, supporting an increased mass limit for WD production.

Lay Summary

When a star no longer produces thermal energy from ongoing fusion, gravitational collapse is held back by outward pressure from electrons. If the star is massive enough, gravity overcomes this pressure, resulting in a supernova explosion and the formation of a neutron star. If not, it will instead form a white dwarf. The limiting mass separating these two fates is critical. We examine this limit via the white dwarf initial-final mass relation, which relates the mass of the white dwarf and its precursor. Determining the precursor mass requires that the white dwarf was born in a star cluster. Extensive searches have been largely unable to populate the high-mass region of the initial-final mass relation. We search for white dwarfs which have escaped from star clusters. We identified several escaped white dwarfs, including one formed from the most massive known precursor star, pushing the limit for white dwarf production.

Preface

This thesis is the result of original research I performed under the supervision of Dr. Harvey Richer at the University of British Columbia. Dr. Jeremy Heyl provided significant additional guidance. Unless otherwise stated, every figure and analysis presented is my own work. I wrote and prepared this manuscript alongside feedback from Dr. Harvey Richer, which was used to clean up the text.

The initial Gaia archive wide search candidate list detailed in Sec.3.1 was found with the support of Helen Du. The list of white dwarfs was narrowed down and analyzed as my original work, with early results published in Richer et al. [112]. I also developed the reddening method used in that work, and helped with some of the finishing work. Fig. 3.1 of this thesis is a slightly modified version of Richer et al. [112] Fig. 16, both figures are my own work. Fig. 1.6 is a recreation of Richer et al. [112] Fig. 17. The data used for this initial IFMR is also included in the final IFMR in Fig. 5.13.

The reconstructed velocity method given in Sec. 3.2 was developed by Dr. Jeremy Heyl and published in Heyl et al. [56]. This technique was applied to four other clusters and published in Heyl et al. [55], of which I am a co-author. The Alpha Persei escapee catalogue shown in Fig. 3.7 was made by Dr. Jeremy Heyl using this method. The figure was my work using his catalogue. Alpha Persei was the focus of follow-up work I first authored and published in Miller et al. [87]. Dr. Jeremy Heyl did the original candidate search of the Fusillo catalogue for this work. In preparing this manuscript, I developed my catalogue from the full Fusillo catalogue using the same methodology as Dr. Heyl. The results of the Hyades WD spectra are being prepared for publication, of which I am a co-author. As with Alpha Persei, the original Fusillo catalogue candidate selection was made

by Dr. Heyl, and I recreated that catalogue using the same methodology for this manuscript.

I performed the reduction and characterization of every spectrum presented in this work. The original code to fit the Balmer lines of the spectra was supplied to me by Dr. Ilaria Caiazzo. Dr. Caiazzo was instrumental in helping to develop my understanding of the data reduction and fitting process. Dr. Caiazzo obtained the spectra for Alpha Persei WDs 3 through 5, as mentioned in Sec. 3.2.1, the results of which are included in Tab. 5.1 and the final IFMR in Ch. 5. We also include results from Heyl et al. [56] in the final IFMR.

Table of Contents

Abstract . . . . . **iii**

Lay Summary . . . . . **iv**

Preface . . . . . **v**

Table of Contents . . . . . **vii**

List of Tables . . . . . **x**

List of Figures . . . . . **xi**

Acknowledgments . . . . . **xvi**

Dedication . . . . . **xviii**

1 Introduction **1**

1.1 Stellar Evolution to a White Dwarf 3

1.1.1 Pre-Main Sequence 4

1.1.2 Main Sequence 6

1.1.3 Subgiant and Red Giant Branches 7

1.1.4 Horizontal and Asymptotic Giant Branches 10

1.1.5 Post-Asymptotic Giant Branch 13

1.2 White Dwarfs 14

1.2.1 Atmosphere 17

1.2.2 Core Composition 18

1.3 Gaia 20
1.4 Star Clusters 22
1.4.1 White Dwarfs in Open Clusters 23
1.4.2 Open Cluster White Dwarf Deficiency 25
1.5 White Dwarf Natal Kicks 26

2 General Procedure 29
2.1 Candidates 29
2.2 Atmospheric Parameters 33
2.3 Cooling Models 36
2.4 Progenitor Mass 37

3 Escapee Candidate Selection 38
3.1 Wide Search 38
3.2 Reconstructed Young Clusters 43
3.2.1 Alpha Persei 48
3.2.2 Hyades 50

4 Observations 54
4.1 Data Reduction 55
4.2 Observation Details 56

5 Results and Discussion 63
5.1 Alessi 21 65
5.2 NGC 2422 65
5.3 NGC 2451B 68
5.4 NGC 2516 70
5.5 Alpha Per 72
5.6 Hyades 74
5.7 vdB Hagen 99 77
5.8 Binary Mergers and Chance Encounters 80
5.9 Implications and State of the IFMR 82

6 Conclusions 85

Bibliography **88**

A Supporting Materials **102**

List of Tables

Table 3.1 Wide Search Clusters 40
Table 3.2 Wide Search Escapee Candidates Select Parameters 44
Table 3.3 Reconstructed Cluster Escapee Candidates 53

Table 4.1 Observation Details 58

Table 5.1 Spectroscopic and Derived Quantities For All Candidates . . . 64

Table A.1 Wide Search Escapee Candidates 103
Table A.1 Wide Search Escapee Candidates 104
Table A.1 Wide Search Escapee Candidates 105
Table A.1 Wide Search Escapee Candidates 106

List of Figures

Figure 1.1 HR diagram for a 1 $M_\odot$ solar metallicity model computed with MESA. Different colour labels show the approximate primary phases of stellar evolution, starting from initial protostar contraction (blue) and ending on the WD cooling sequence (yellow). 4

Figure 1.2 *Left*: HR diagram of PARSEC stellar isochrones for 10 Myr steps between 20 (blue) and 300 (green) Myrs. Isochrones computed using Kroupa [77] IMF, solar metallicity, and no reddening. The black line shows the approximate MSTO of the isochrones. *Right*: Mass at the estimated MSTO for the left panel isochrones compared with isochrone age. 8

Figure 1.3 Abundance profile of H, He, C, and O for three key phases of the 1 $M_\odot$ evolutionary model displayed in Fig. 1.1. *Left*: Main sequence turnoff. *Middle*: Tip of the red giant branch. *Right*: Tip of the asymptotic giant branch. 15

Figure 1.4 Sample of WDs within 200 pc from the Gentile Fusillo et al. [49] catalogue. The approximate Q branch overdensity is indicated in red. 16

Figure 1.5 Partial Gaia DR2 CMD coloured by density, from low (purple) to high (yellow) density. 21

Figure 1.6 The IFMR from R21. Includes WDs discovered in their work as well as those they included from Cummings et al. [29]. . . 24

Figure 2.1 Gaia EDR3 CMD of NGC 2422 for corrected excess factor cuts of 1σ (far left), 3σ (middle left), 5σ (middle right), and 10σ (far right). 31

Figure 3.1 Full uncut CMD of candidate cluster member WDs identified in the wide search. Objects dereddened using the cluster reddening values determined by R21. Horizontal tracks are for cooling ages from 10 Myr to 1 Gyr (top to bottom), while vertical tracks display mass models from 0.2 to 1.28 $M_{\odot}$ (right to left). 41

Figure 3.2 Cumulative distribution of the square of the distance from the associated cluster center for the wide search WDs, scaled by the cluster's radius. The blue curve displays the 151 candidates retained after initial cuts, while the red curve shows the 841 discarded candidates. 43

Figure 3.3 CMDs of the Alessi 21 cluster. *Left*: Cluster member candidates from R21 (black), with wide search candidate escapees before data cuts (red). Horizontal tracks are for cooling ages from 10 to 250 Myr (top to bottom), while vertical tracks display mass models from 0.7 to 1.28 $M_{\odot}$ (right to left). *Middle*: As in left graph, but with post-cut escapee candidates including 1σ error bars. *Right*: Zoom in of the WD cooling sequence from the middle graph, with select candidates for follow-up observation in blue. 45

Figure 3.4 Wide search cluster CMDs as in Fig. 3.3, but for NGC 2422. . 46

Figure 3.5 Wide search cluster CMDs as in Fig. 3.3, but for NGC 2451B. 46

Figure 3.6 Wide search cluster CMDs as in Fig. 3.3, but for NGC 2516. . 47

Figure 3.7 Gaia EDR3 CMDs for Alpha Persei cluster from H21b search. *Left*: Cluster members. *Middle*: Escapee candidates. Horizontal tracks are for cooling ages from 10 to 250 Myr (top to bottom), while vertical tracks display mass models from 0.7 to 1.28 $M_\odot$ (right to left). *Right*: Zoom in of the WD cooling sequence from the middle gtaph, with selected candidates for follow-up observation in blue. 49
Figure 3.8 White dwarf cooling sequence with potential escapees from the Alpha Persei cluster identified in the Gentile Fusillo et al. [49] WD catalogue. Candidates selected for follow-up observations indicated in blue. Cooling tracks are as in Fig. 3.7. . . 50
Figure 3.9 Gaia EDR3 CMDs for Hyades cluster. *Left*: Cluster members from Lodieu et al. [84] crossmatch. *Middle*: Escapee candidates from H21a method. Horizontal tracks are for cooling ages from 50 to 700 Myr (top to bottom), while vertical tracks display mass models from 0.7 to 1.28 $M_\odot$ (right to left). *Right*: Zoom in of the WD cooling sequence from the central graph, with selected candidate for follow-up observation in blue. . . 52
Figure 3.10 As in Fig. 3.8, but for the Hyades cluster. Cooling tracks are as in Fig. 3.9. 52

Figure 4.1 WD cooling sequence of the vdB Hagen cluster, whose Gaia EDR3 CMD shown in Fig. 2.2b. Candidate WD is to the left of the cooling sequence, along with 1σ error bars. Cooling sequences are as in Fig. 3.8. 57
Figure 4.2 Reduced spectra for WDs identified in the wide search. We normalize the flux at 4400 $\AA$. The different spectra are shifted vertically arbitrarily for comparison. The central wavelength of the Balmer lines Hβ through Hε are indicated with blue vertical lines on the left panel, while the right panel shows the same for Hα. 59
Figure 4.3 As in Fig. 4.2, but for Alpha Persei escapee candidates. 60
Figure 4.4 As in Fig. 4.2, but for Hyades escapee candidate. 61

Figure 4.5 As in Fig. 4.2, but for vdB Hagen 99 cluster member candidate. 62

Figure 5.1 Balmer line fits of Hβ through Hε for the wide search WD spectra shown in Fig. 4.2. Hα is not included due to insufficient SNR. Alessi 21 WD1 and NGC 2422 fit with Gianninas et al. [50] metal polluted H-dominated atmosphere models, while the remainder use pure H models from Tremblay et al. [132]. 66

Figure 5.2 Alessi 21 EDR3 CMD, with PARSEC [13] isochrones computed with the Kroupa [77] IMF and no extinction, at solar metallicity. Ages as indicated on the diagram. 67

Figure 5.3 As in Fig. 5.2, but for NGC 2422 computed with metallicity of $[\mathrm{Fe/H}] = +0.09$. 68

Figure 5.4 As in Fig. 5.2, but for NGC 2451B. 69

Figure 5.5 As in Fig. 5.2, but for NGC 2516 computed with metallicity of $[\mathrm{Fe/H}] = +0.05$. An additional extinction of $\mathrm{Ag} = 0.1$ has been added when computing the PARSEC isochrones. 70

Figure 5.6 As in Fig. 5.1, but for Alpha Persei WDs 1 and 2. WD1 uses pure H models while WD2 uses metal polluted ones. 72

Figure 5.7 As in Fig. 5.2, but for Alpha Persei. 73

Figure 5.8 As in Fig. 5.1, but for the Hyades using pure H models. 75

Figure 5.9 As in Fig. 5.2, but for the Hyades with a metallicity of $[\mathrm{Fe/H}] = +0.24$. 76

Figure 5.10 Comparison of Hyades WD spectra to GD50 spectra from Guo et al. [53]. Hyades data and fit are as in Fig. 5.8. GD50 Balmer lines were extracted and fit using the same methodology as the Hyades. The purple line illustrates a fit using the GD50 log g along with the Hyades T_{eff}. 78

Figure 5.11 As in Fig. 5.1, but for vdB Hagen 99 using metal polluted models. 79

Figure 5.12 As in Fig. 5.2, but for vdB Hagen 99. 80

Figure 5.13 Updated IFMR. Hyades, Various, and M44 from R21 as in Fig. 1.6. Pleiades points are from H21a found via their reconstructed velocity method. The remainder are as described in this work. Alpha Persei and NGC 2516 points are for ONe cores, while the remainder are for CO. 83

Figure A.1 As in Fig. 3.3, but for Alessi 5. 106
Figure A.2 As in Fig. 3.3, but for Alessi 8. 107
Figure A.3 As in Fig. 3.3, but for Alessi 12. 107
Figure A.4 As in Fig. 3.3, but for Alessi 19. 108
Figure A.5 As in Fig. 3.3, but for Alpha Persei. 108
Figure A.6 As in Fig. 3.3, but for ASCC 113. 109
Figure A.7 As in Fig. 3.3, but for Collinder 121. 109
Figure A.8 As in Fig. 3.3, but for Collinder 132. 110
Figure A.9 As in Fig. 3.3, but for IC 2391. 110
Figure A.10 As in Fig. 3.3, but for NGC 5662. 111
Figure A.11 As in Fig. 3.3, but for NGC 6025. 111
Figure A.12 As in Fig. 3.3, but for NGC 7063. 112
Figure A.13 As in Fig. 3.3, but for Pismis 4. 112
Figure A.14 As in Fig. 3.3, but for Pleiades. 113
Figure A.15 As in Fig. 3.3, but for vdB Hagen 164. 113

Acknowledgments

This work would not have been possible without the support of my supervisor, Dr. Harvey Richer, whose guidance was instrumental throughout the last two years. Even as the world was turned upside down by a global pandemic, and my life was doubly so due to newfound fatherhood, Dr. Richer's support was unwavering. I also want to thank the others in our research group that helped me along the way. The results of this project would not have been possible without helpful discussions with Helen Du, Steffani Grondin, and James Hegarty. Special thanks to Dr. Ilaria Caiazzo, who helped me learn the ins-and-outs of Gemini data reduction and subsequent analysis, and to Dr. Jeremy Heyl, who provided so many ideas, questions, and results that guided the direction of this work.

I acknowledge the support of the Natural Sciences and Engineering Research Council of Canada (NSERC).

This research has made use of the SIMBAD and Vizier databases, operated at CDS, Strasbourg, France, the Montreal White Dwarf Database produced and maintained by Prof. Patrick Dufour (Université de Montrèal) and Dr. Simon Blouin (LANL), and the WEBDA database, operated at the Department of Theoretical Physics and Astrophysics of the Masaryk University.

This work has made use of data from the European Space Agency (ESA) mission *Gaia* (https://www.cosmos.esa.int/gaia), processed by the *Gaia* Data Processing and Analysis Consortium (DPAC,https://www.cosmos.esa.int/web/gaia/dpac/consortium). Funding for the DPAC has been provided by national institutions, in particular the institutions participating in the *Gaia* Multilateral Agreement.

Based on observations obtained at the international Gemini Observatory, a program of NSF's NOIRLab, which is managed by the Association of Universities for

Research in Astronomy (AURA) under a cooperative agreement with the National Science Foundation on behalf of the Gemini Observatory partnership: the National Science Foundation (United States), National Research Council (Canada), Agencia Nacional de Investigación y Desarrollo (Chile), Ministerio de Ciencia, Tecnología e Innovación (Argentina), Ministério da Ciência, Tecnologia, Inovações e Comunicações (Brazil), and Korea Astronomy and Space Science Institute (Republic of Korea).

Gemini spectra were processed using the Gemini IRAF package.

Dedication

For my wife Lisa and daughter Astra, whose unceasing love makes all the late nights worth it.

Chapter 1

Introduction

Every star eventually loses the ability to produce thermal radiation from fusion, losing much of its mass along the way to end its life as a stellar remnant. The most common of these remnants is a white dwarf (WD), which is a primarily electron-degenerate compact object that will steadily reduce in temperature for the rest of its lifetime as the ions, which are the source of the stellar luminosity, slowly cool. WDs are the expected final evolutionary state for the vast majority of stars in the Universe [41]. The maximum mass of a stable WD is known to be approximately 1.4 $M_\odot$ [94]; the maximum mass of the progenitor star that formed it, however, is not so well understood. Estimates from theoretical considerations suggest the high mass cutoff for WD production should be at around 8 $M_\odot$ [136]. Horiuchi et al. [61] examined the rate of type II supernovae (SN II) compared with massive star formation rates. They found that the measured rate of SN II was a factor of two smaller than the rate of formation of stars with $M > 8$ $M_\odot$. One potential way to solve this discrepancy is by allowing for a higher upper mass limit for WD production, which would lead to an increase in WD formation and corresponding reduction in the number of neutron stars. Kroupa and Weidner [78] studied the stellar initial mass function and found that extending the upper mass limit for WD production as high as 12 $M_\odot$ could potentially resolve the discrepancy.

The maximum mass of a WD progenitor is critical as it has a significant impact on several important aspects of astronomy, including but not limited to the formation rates of compact objects, the star formation rate of galaxies, and the

enrichment rate of heavy elements in galaxies. As such, resolving the aforementioned tension and better constraining this upper mass limit is paramount. This limit can be examined by relating the mass of a WD to its progenitor through the WD initial-final mass relation (IFMR). While significant progress has been made in developing the IFMR in the last few decades (e.g. [29], [23], [35], [70], [111]), the IFMR remains sparse, notably lacking in stars in the high mass region.

Populating this high mass region is critical but remains a difficult task as the most massive WDs tend to be both rare and typically faint. As an additional challenge, determining the WD progenitor mass requires identifying WDs which are bonafide members of young open star clusters. Every star in a cluster was born at approximately the same time, so the cluster's age reveals the total age of any object born with it. By determining the age of the cluster from stellar isochrones, and the age of the WD from cooling models, one can subtract the two and determine the age of the progenitor and, subsequently, its mass. Without confident cluster association, we cannot determine the age of the progenitor nor its mass. Clusters must both be sufficiently old to have had time to produce massive white dwarfs and yet young enough for those WDs to have not cooled beyond detectability.

In recent years, the development of the IFMR has accelerated with the launch of the Gaia observatory [44]. The Gaia observatory has given unprecedented data access for stellar astronomy by precisely measuring the astrometry of more than a billion stars in the Milky Way. This data has allowed for extensive searches of Milky Way open star clusters for WDs that could potentially populate the high mass region of the IFMR. Despite unprecedented data breadth, the high mass region remains vastly underpopulated, with no previously known cluster member WDs with masses above 1.1 $M_\odot$ or progenitors above 6.2 $M_\odot$ (see e.g. [29], [112], [106]). The lack of WDs in young clusters might result from being ejected from their host clusters due to aspherical mass loss in the late stages of stellar evolution or from dynamical interactions. In this work, we search for massive WDs that may have been ejected from their host clusters in an attempt to populate the high mass region of the IFMR and better constrain the maximum mass of a WD progenitor.

The remainder of this thesis is arranged as follows: the rest of this chapter reviews relevant aspects of stellar evolution, white dwarfs, the Gaia observatory, star clusters, and WD natal kicks. Ch. 2 details the general methodology for identi-

fying and characterizing ultramassive WDs. Ch. 3 explains specific searches and the resulting candidate selection. Ch. 4 describes follow-up observations obtained for these selected candidates, with the results of these observations analyzed and discussed in Ch. 5. Finally, Ch. 6 summarizes and concludes the main results while mentioning ongoing work and future considerations.

1.1 Stellar Evolution to a White Dwarf

In this section, we describe the main phases of stellar evolution, from the earliest birth stages until the final stages as a white dwarf. While we will attempt to detail the evolutionary path to becoming a WD, we emphasize that this is not an exhaustive description of stellar evolution; an interested reader is referred to the literature for such an examination (see e.g. [117]). While we probe many vital differences in the evolution of stars of various masses, we will not generally focus on the features of particularly low ($M < 0.5$ $M_\odot$) and high ($M > 12$ $M_\odot$) mass stars. We neglect the low mass stars as their main sequence lifetimes exceed the current age of the Universe [120], while we exclude high mass stars because they are beyond even the most radical mass limits for WD production [78].

Stellar evolution is often illustrated using a Hertzsprung-Russell (HR) diagram, which shows the relationship between a star's luminosity L and its effective surface temperature $T_{\rm eff}$, with luminosity increasing upwards along the y-axis and temperature increasing to the left along the x-axis. In Fig. 1.1, we show an HR diagram for the evolution of a 1 $M_\odot$ star at solar metallicity of $Z = 0.2$, with solar initial He fraction of 0.278 [121]. Models were computed using the Modules for Experiments in Stellar Astrophysics (MESA) version 12778 (see MESA instrument papers [101], [102], [103], [104], and [105]). Evolution begins with the onset of protostellar contraction and terminates in the WD cooling sequence when the WD reaches a lower limit of $\log(L/L_\odot) = -1$. We will examine the critical phases of stellar evolution illustrated by this figure in the proceeding sections of this chapter.

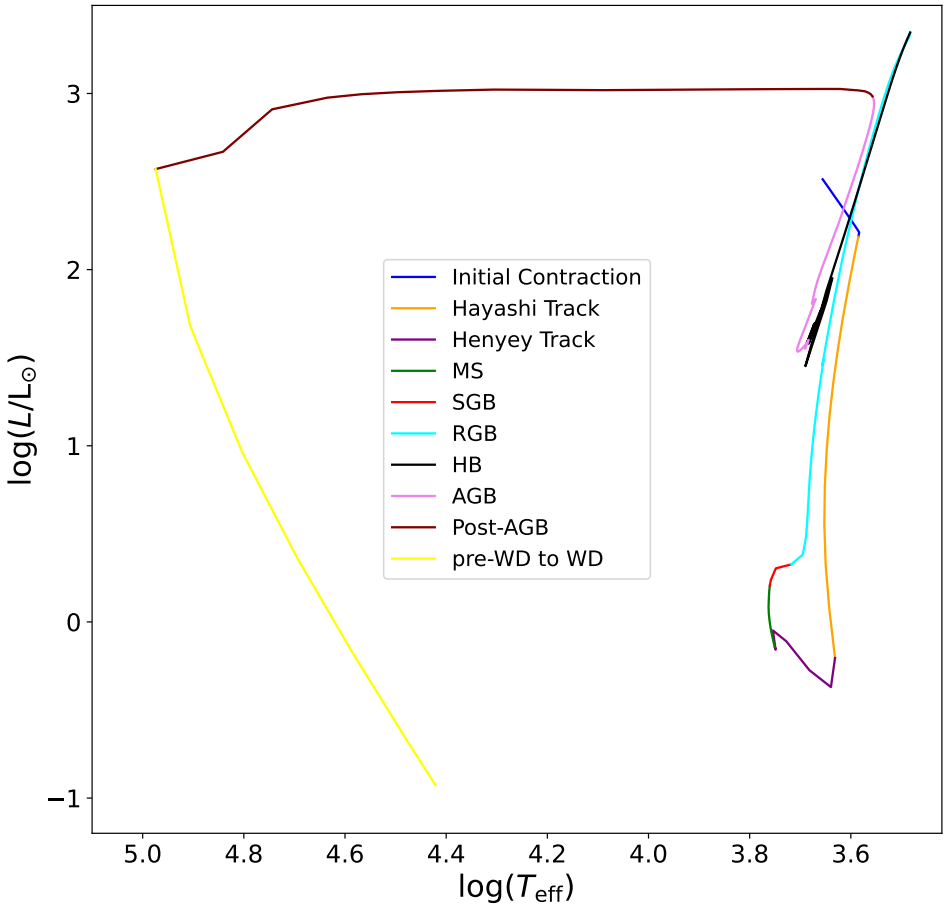

Figure 1.1: HR diagram for a 1 $M_\odot$ solar metallicity model computed with MESA. Different colour labels show the approximate primary phases of stellar evolution, starting from initial protostar contraction (blue) and ending on the WD cooling sequence (yellow).

1.1.1 Pre-Main Sequence

Stellar evolution begins when a cool molecular cloud's mass exceeds the Jeans mass, given by

$$M_{\rm J} = \left(\frac{5k_{\rm B}T}{{\rm G}\mu}\right)^{3/2}\left(\frac{3}{4\pi\rho}\right)^{1/2} \tag{1.1}$$

where k_B is the Boltmann constant, G is the gravitational constant, and μ and ρ are the mean molecular weight and density of the cloud, respectively [39]. The molecular cloud's inward gravitational pull then exceeds the outward pressure, resulting in the collapse of the inner regions of the cloud. Perturbations in the density of different regions lead to isolated collapsing cores in the cloud. Each of these overdense regions may collapse to form a protostar surrounded by a protoplanetary disc. The protostar will continue to gain mass as it accretes from the surrounding disc. As material accretes onto the protostar, gravitational energy heats the surrounding gas, causing it to emit infrared (IR) radiation [58].

The collapsing region has extremely low pressure and is transparent to radiation, so the radiation typically escapes, and the collapse continues largely unopposed. This rapid free-fall collapse continues until the protostar becomes opaque in the IR [124]. At this point, the escaping IR radiation is trapped and begins to heat the centre of the protostar, increasing the pressure. Eventually, the pressure reaches a point where it prevents the infall of additional gas into the core. At this stage, the protostar has blown away its envelope and ceases accreting material, stabilizing its mass until the late stages of its lifetime.

The subsequent stages of evolution depend almost entirely on the mass of the protostar. The most massive protostars will have already contracted to the point where they can fuse hydrogen (H) to helium (He) in their cores and will evolve from the protostar stage directly to the main sequence (MS) defined by the onset of H core burning. For stars less massive than about 8 $M_\odot$, the core temperature is not yet sufficiently hot to initiate H burning; these stars will go through additional stages as pre-main sequence (pre-MS) stars. Throughout the rest of the pre-MS, these stars will continue to contract, albeit at a reduced pace compared with the free-fall collapse associated with early protostar formation.

Stars between 3 and 8 $M_\odot$ are fully radiative at the start of the pre-MS [71]. Stars less than 3 $M_\odot$ are initially fully convective and go through a period of evolution known as the Hayashi track [71], where they stay at roughly the same temperature but see their luminosities drop by several orders of magnitude as they contract. The least massive of these stars, those below 0.5 $M_\odot$, retain this convective core until the onset of H burning [71]. Stars between 0.5 and 3 $M_\odot$ develop a radiative core at the end of the Hayashi track [71]. At this point they enter the Henyey track,

where the star continues to contract while maintaining hydrostatic equilibrium and a near-constant luminosity. The temperature steadily increases during this stage until the onset of H burning. The least massive protostars, those below about 0.08 $M_{\odot}$, will never reach the temperature necessary for H fusion, thus never becoming a star and instead forming a brown dwarf [6].

1.1.2 Main Sequence

Though these different initial tracks lead to significantly different lifetimes in these pre-MS stages for stars of varying mass, all stars will eventually reach a point in their evolution where they are first able to fuse H to He in their core. This phase is known as the zero-age main sequence (ZAMS). Stars remain on the MS until the core has been exhausted of hydrogen fuel; most stars will spend the vast majority of their lifetime in this phase [124]. Duration on the MS depends primarily on star's mass, with the most massive stars burning through their core H first. Initial chemical composition and certain mixing processes additionally have only a minor impact on MS lifetime. In this phase, outward pressure from thermal radiation produced by core H fusion balances gravity and prevents collapse, keeping the star in hydrostatic equilibrium [6]. This keeps the star at a roughly constant size throughout the phase.

Two separate nuclear reaction channels allow for the transformation of H into He; the proton-proton (PP) chain and the carbon-nitrogen-oxygen (CNO) cycle. While these two reaction channels take very different paths, the net result is similar, H is converted to Helium-4 with a significant release of energy. In nearly all MS stars, both channels occur simultaneously, though reaction efficiencies will depend on the star's mass. The nuclear reaction rate of each channel also depends heavily on the temperature of the star's core. For a star of the Sun's mass, the PP chain accounts for more than 90% of the total energy generation [124]. The CNO cycle becomes the leading energy generator for stars with masses around 1.3 $M_{\odot}$, becoming more and more dominant as the mass, and thus core temperature, of the star increases [124]. When the CNO cycle dominates the energy generation, the centre of the star becomes convective, with the size of the convective core steadily increasing with mass [36].

Though most stars spend $> 80\%$ of their lifetime on the MS [63], their location in the HR diagram changes only slightly during this phase, shifting upwards and to the right due to an increase in luminosity and decrease in temperature. Luminosity increases as a result of the change in the chemical composition of the core as H converts into He. Luminosity scales with molecular weight to the 4th power (μ^4) [6], increasing as the star becomes increasingly dominated by the heavier He. The radius increases modestly as the envelope expands. Once a star has exhausted the H in its core, it will leave the MS at what is known as the main sequence turnoff (MSTO).

The main sequence lifetime of a star depends sensitively on its mass. A excellent way to illustrate this is via stellar isochrones, which are curves on an HR diagram of stars with the same age but different masses. This is appropriate for a star cluster where stars of various masses formed all at the same time. The left panel of Fig. 1.2 shows PARSEC stellar isochrones [13][1] for ages from 20 to 300 Myrs. We illustrate the MSTO mass vs lifetime on the right panel. We see the 20 Myr isochrone has a MSTO mass of approximately 9.5 $M_\odot$, compared to under 3 $M_\odot$ at 300 Myrs.

1.1.3 Subgiant and Red Giant Branches

At the MSTO, shown as the brightest point in green in Fig. 1.1, core hydrogen has been exhausted and converted to helium. Thick shells of H surround the inert He core in all but the lowest mass stars, which are composed entirely of He by the end of the MS [120]. The temperature of these shells is less than the core, below the necessary levels for He fusion in stars above 1.2 $M_\odot$ [6]. For these higher mass stars, the core contracts slightly until the ignition of the H shell, giving a characteristic hook on an HR diagram as the star shifts to a higher temperature before H shell burning. Stars below 1.2 $M_\odot$ burn H in these shells immediately after the MS and lack this hook [6]. The phase of H shell burning is known as the subgiant branch (SGB) and is dominated by the CNO cycle. During the SGB the envelope of the star expands, causing the star to cool and shift further to the right in the HR diagram. As the outer layers of the star cool and the envelope

[1] PARSEC isochrones are available at http://stev.oapd.inaf.it/cgi-bin/cmd

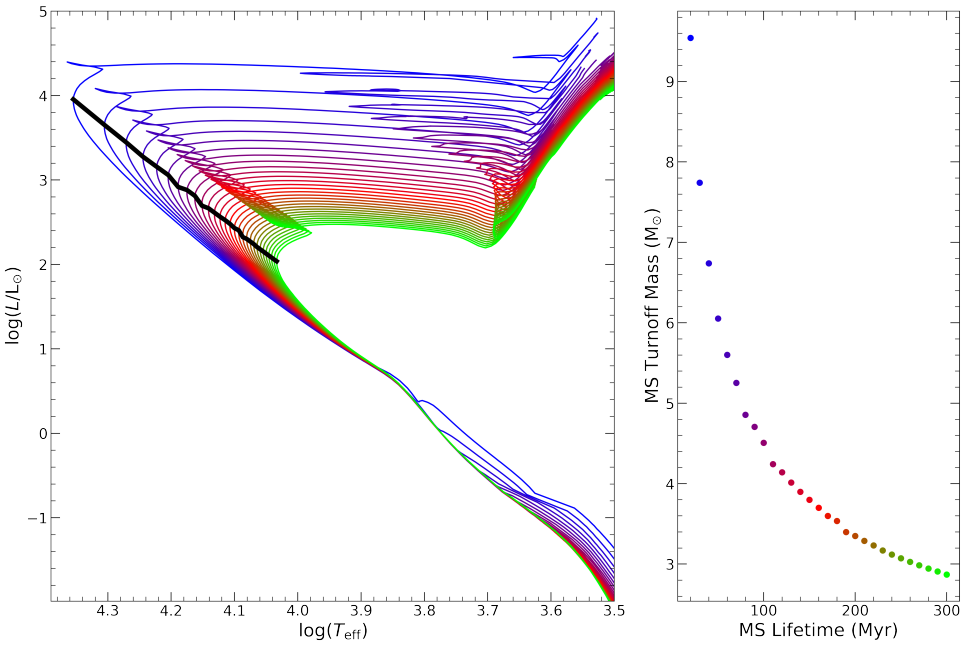

Figure 1.2: *Left*: HR diagram of PARSEC stellar isochrones for 10 Myr steps between 20 (blue) and 300 (green) Myrs. Isochrones computed using Kroupa [77] IMF, solar metallicity, and no reddening. The black line shows the approximate MSTO of the isochrones. *Right*: Mass at the estimated MSTO for the left panel isochrones compared with isochrone age.

expands, newly produced He material sinks into the star's central regions, growing the isothermal He core.

Depending on the star's mass, the core at this stage of evolution may reach a critical mass known as the Schönberg Chandrasekhar limit, given by

$$\left(\frac{M_{\rm ic}}{M}\right) = 0.37\left(\frac{\mu_{\rm env}}{\mu_{\rm c}}\right)^2, \tag{1.2}$$

where $M_{\rm ic}$ is the mass of the isothermal core and $\mu_{\rm env}$ and $\mu_{\rm c}$ are, respectively, the envelope's and core's mean molecular weights [142]. If the star's mass is > 6 M$_\odot$, the mass of the isothermal core will already exceed the Schönberg Chandrasekhar limit at the end of the MS, leading to an extremely short or nonexistent SGB phase

[6]. Stars between 2.2 and 6 $M_\odot$ will start the SGB below this critical mass but will eventually surpass it as the inert He core grows [6]. Stars less massive than 2.2 $M_\odot$ have partially degenerate He cores which have sufficient pressure to support the growing envelope and do not reach the Schönberg Chandrasekhar limit [6].

For stars above 2.2 $M_\odot$, when the core surpasses this critical mass, it cannot support its outer layers and it falls out of hydrostatic equilibrium [6]. The He core rapidly contracts and releases energy which heats the envelope. The envelope greatly expands, typically increasing the size of the star by at least one hundred times. The star leaves the SGB and begins its life on the red giant branch (RGB) when it surpasses the Schönberg Chandrasekhar limit. During the RGB, the star's luminosity greatly increases, while the temperature decreases only gradually, leading to a near vertical evolutionary path in the HR diagram. Stars below 2.2 $M_\odot$ become more and more degenerate as the core mass slowly increases during the SGB, eventually becoming fully degenerate [6]. The cooling outer layers of the star become fully convective as the temperature decreases. This convection allows material to be carried towards the stellar surface, significantly increasing the stellar luminosity. At this stage, these stars have left the SGB, following a similar evolutionary path up the RGB as their higher mass counterparts.

Near the beginning of the RGB, stellar surface convective zones expand inwards, eventually coming into contact and mixing with regions of the star that have undergone H fusion. Material leftover from fusion is transported to the surface, altering the composition of the stellar surface in a process referred to as the first dredge up [36]. H shell fusion continues until the core temperature is sufficient to ignite He via the triple-α nuclear burning process, at which point the star reaches the tip of the RGB, signalling the end of the phase. The triple-α process is more straightforward than the PP and CNO ones, with only two steps. In the first step, two Helium-4 particles combine to form Beryllium-8. In the second, a third Helium-4 particle combines with the Beryllium-8 to create Carbon-12. The first step in this process costs a small amount of energy, while the 2nd releases a much higher amount, leading to a significant net energy gain [17].

Before reaching the tip of the RGB, the H burning shell in stars below 2 $M_\odot$ expands enough to reach the discontinuity in the star's H abundance resulting from the first dredge up, at which point its luminosity briefly decreases [71]. Once the

H-burning shell passes the discontinuity, the luminosity increases again and the star continues towards the tip of the RGB. This brief decrease in luminosity leads to an overabundance of stars in that region of an HR diagram known as the red bump. Stars more massive than 2 $M_\odot$ reach sufficient temperatures to activate the triple-α process before reaching this discontinuity and avoid the red bump. The time spent in this phase depends greatly on mass, with low mass stars spending hundreds of millions of years on the RGB while the most massive stars, those above 15 $M_\odot$, fuse He on the MS and avoid the RGB altogether [6].

The characteristics of the onset of He burning at the tip of the RGB vary sensitively with mass. Lower mass stars below 2.2 $M_\odot$ have partially or fully degenerate cores [36]. As He fusion begins in the core, the temperature increases, but, due to this degeneracy, the pressure essentially does not. As such, although the temperature increases, the core does not expand. The increased temperature increases the He reaction rate, which further increases the temperature. The result is a brief thermonuclear runaway event of He core fusion called a helium flash. This thermonuclear event raises the temperature to the point where thermal pressure in the core overtakes degenerate pressure, allowing the core to expand and shut off the He flash. The degeneracy of the core declines after the He flash but it remains partially degenerate. The primary He flash is followed by a series of secondary flashes, completely removing the core degeneracy. Once the core is no longer degenerate, stable core He fusion begins. Stars more massive than 2.2 $M_\odot$ are non-degenerate at the tip of the RGB and do not experience a He flash. [36].

1.1.4 Horizontal and Asymptotic Giant Branches

At this stage, the He-burning non-degenerate core of the star has expanded, causing the H-burning shell to grow, reducing its temperature and density. Stellar emission is dominated by this outer burning shell, decreasing the star's luminosity notably compared with the tip of the RGB [6]. This core He and H shell burning phase is referred to as the horizontal branch (HB) and is the second longest for most stars. The HB lifetime is substantially shorter than the MS due to the increased luminosity associated with He burning. Stars with degenerate cores at the tip of the RGB tend to cluster close together in the HR diagram in the early stages of

the HB, leading to an overdensity of stars in the diagram known as the red clump. Stars remain on the HB until their core He has been exhausted, leaving behind a primarily carbon-oxygen (CO) core.

For most stars, their core temperature is too low to ignite C; as a result, the core again contracts and rises in temperature. As the core shrinks, the surrounding shell of He increases in temperature until it eventually surpasses the temperature necessary for He ignition. This burning phase causes the star to significantly expand while its surface temperature declines and its luminosity increases. The evolutionary path approaches the RGB asymptotically as the temperature increases. Appropriately, this phase of stellar evolution is called the asymptotic giant branch (AGB). The AGB evolutionary track gets very close to the RGB for lower mass stars, while the gap is far more substantial for higher mass stars. In addition to He shell burning outside the core, H shell burning begins again farther out in the star, with the two burning layers separated by an inert He layer.

In the early stages of the AGB, He shell burning dominates energy production. For stars with $M > 4$ $M_\odot$, the convective outer envelope reaches deep into the star and crosses the H burning shell, carrying nuclear processed material to the surface resulting in a second dredge up [10]. As He burns, the shell becomes depleted of material, allowing for the thicker H-burning shell to dominate the energy generation of the star. As this shell burns, additional He is deposited onto the inert layer separating the two burning layers. As this layer is partially degenerate, when it becomes massive enough it ignites in a helium flash, analogous to the one experienced at the tip of the RGB, albeit not as extreme. After the flash, He shell burning continues, decaying as fusionable material is consumed. This again leads to H-burning dominating the star's nuclear energy generation [36]. As that H layer deposits more He into the intermediate inert layer, another He flash occurs; this process repeats, leading to periodic thermal pulsations of the star.

Convective outer layers penetrate deeper into the star as the envelope cools, while simultaneously thermal pulse driven internal convection carries He burning remnants outwards. These He burning materials cross the outer convective layer, carrying heavy elements such as carbon and oxygen to the surface in a third dredge up [71]. Every star massive enough to proceed along the AGB experiences the third dredge up. If $M > 5$ $M_\odot$, the star undergoes a event called hot bottom

burning, where high temperatures at the bottom of the convective envelope trigger secondary CNO cycle reactions in the H burning shell [6]. These secondary reactions can create elements as heavy as aluminum in the most massive AGB stars [6]. Throughout the AGB phase, weakly bound extended outer layers of the star lead to significant mass loss from stellar winds, with the rate of mass loss steadily increasing as the envelope expands outward. He shell flash driven thermal pulsations continue until the mass loss has caused the outer H shell to approach the stellar surface at the tip of the AGB.

During the AGB, if the mass of the inert CO core exceeds ~ 1.05 $M_{\odot}$, which occurs for a total stellar mass of ~ 6.5 $M_{\odot}$, the partially degenerate CO core reaches temperatures sufficient for C burning [31]. This initial C ignition occurs off-centre and proceeds as a violent carbon flash analogous to the He flash during the RGB. Stars that ignite C are said to have reached the super-AGB phase. The C flash reduces the core temperature and its degree of degeneracy, eventually shutting off the flash. The core then contracts again, increasing its temperature and leading to an additional off-centre C flash in the partially degenerate core. This second carbon flash forms a convective C ring that burns until it reaches the centre of the star, leaving behind a primarily oxygen-neon (ONe) core. Carbon burning continues radially outward through the star, generating secondary C flashes as the convective burning region crosses regions of high C concentration. Once C burning has ceased, the core consists of a large ONe central core surrounded by a thin shell of CO. The star's outer layers are similar to the AGB phase, with a He burning shell surrounded by an inert He layer, a H burning shell, and an increasingly extended H-rich envelope.

If the mass of the ONe core exceeds the Chandrasekhar limit, carbon burning is followed by Ne and all successive stellar burning stages. If at any point during the AGB phase the core grows to this limit, the star will end its life after nuclear burning as a supernova, becoming either a neutron star or a black hole, depending on the mass of the precursor star. Given that these massive stars do not become WDs, we will not consider them further. Stars massive enough to ignite carbon but not neon proceed similarly to their lower mass AGB counterparts once C-burning ceases. Successive periods of dominance by the He-burning and H-burning layer lead to He shell flashes and thermal pulsation of the inner regions of the star. Compared

with AGB stars, super-AGB thermal pulses experience reduced pulse duration and temporal separation [31]. Particularly low metallicity high mass super-AGB stars can undergo thousands of thermal pulses before the end of the super-AGB phase [31]. As in the AGB phase, the super-AGB phase ends when the outer H shell approaches the stellar surface due to the loss of most of the star's envelope from stellar winds.

1.1.5 Post-Asymptotic Giant Branch

At the tip of the AGB, the mass of the envelope has been almost entirely lost due to stellar winds, and the star can no longer sustain its remaining convective envelope. The star radiatively contracts, steadily shrinking while simultaneously increasing its temperature. H continues to burn in the outer shell, keeping the star at roughly constant luminosity and leading it to move predominantly horizontally towards higher temperature in the HR diagram. The central star is surrounded by unbound material lost from the envelope during the AGB, referred to as the circumstellar envelope. Once H fusion sufficiently increases the central star's temperature, it emits ultraviolet (UV) radiation that destroys dust in the circumstellar envelope and may ionize the surrounding gas [9]. If the central star heats up too quickly, it will not have time to fully ionize the gas, while prolonged evolution leads to the circumstellar envelope dissipating before ionization [71]. In most cases the star will heat at a pace that allows the gas in the circumstellar envelope to become fully ionized and begin to emit as a planetary nebula (PN). The remaining envelope is rapidly lost as the central star increases its temperature. The star continues to heat until its H shell burning is extinguished, signaling the start of its evolution as a white dwarf. Once the post-AGB phase is complete, the star will spend the rest of its life cooling as a WD.

Sometimes, a star can experience an additional He flash thermal pulse soon after leaving the AGB phase. This late thermal pulse (LTP) causes the star to briefly return to the AGB phase before the flash shuts off, and the star loops back to the post-AGB phase, again forming a PN [62]. Compared with other post-AGB stars, those that experience the LTP have meager H mass fraction after returning to the post-AGB phase. Late in the post-AGB phase or early in the WD cooling

phase, post-AGB stars can experience another LTP known as the very late thermal pulse (VLTP). The VLTP returns the star to the AGB phase once again before looping back towards the WD cooling phase. The increased delay before the onset of the VLTP results from reduced H shell mass. The VLTP leaves the star nearly entirely depleted of H on its surface [54]. The H deficiency of post-AGB stars that experience the LTP and VLTP leads to them forming He-dominated WDs. The conditions necessary for a star to undergo the LTP and VLTP are not currently well understood.

In Fig. 1.3, we show the abundance profile of primary elements throughout the star towards the end of three key phases of the evolutionary model displayed in Fig. 1.1. At the end of the MS, the total stellar mass remains exceptionally close to its initial mass of 1 $M_\odot$. The core is entirely He, while the outer layers are a mixture of He and H, with H increasingly dominating towards the surface. Note that the abundance of He on the surface is due to the initial He fraction, which is distributed evenly throughout the star. At the end of the RGB the He core has increased in mass, while the total stellar mass has dropped from the initial mass down to ~ 0.65 $M_\odot$. At the end of the AGB, the total stellar mass has fallen to ~ 0.5 $M_\odot$, nearly entirely in the CO core. Outside the core there is a shell of He, followed by a thin H envelope.

1.2 White Dwarfs

White dwarfs have a relatively simple structure, consisting of a degenerate core surrounded by a partially degenerate envelope of one or multiple layers of lighter elements, generally hydrogen and/or helium. At the start of the WD phase, these stellar remnants are amongst the hottest objects in the Universe, with surface temperatures exceeding $200,000$ K [25]. WDs radiate thermal energy from the previous burning but no longer generate new thermal energy through ongoing fusion. As these objects are very compact, they have small surface areas and slowly radiate heat, leading to gradual cooling over time, decreasing the WD's luminosity in turn. The WD's radius remains roughly constant as its temperature and luminosity decrease. The most massive WDs are also the smallest, where the mass-radius

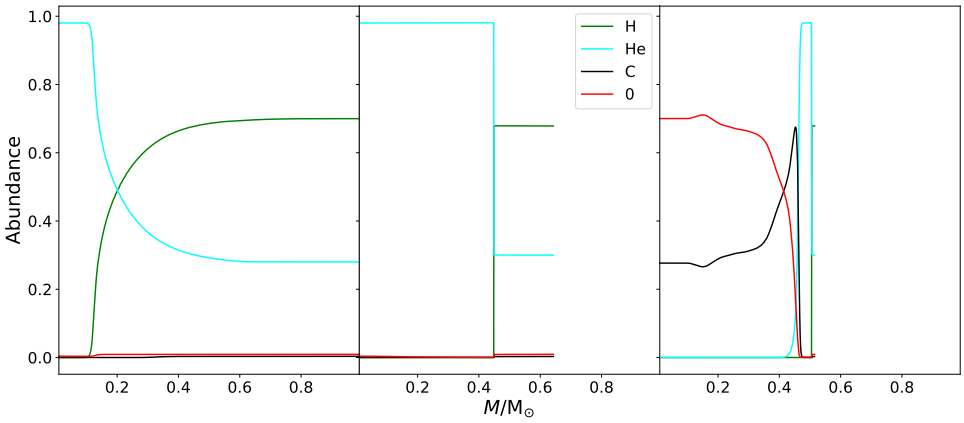

Figure 1.3: Abundance profile of H, He, C, and O for three key phases of the 1 $M_\odot$ evolutionary model displayed in Fig. 1.1. *Left*: Main sequence turnoff. *Middle*: Tip of the red giant branch. *Right*: Tip of the asymptotic giant branch.

relationship can be approximated as

$$R \approx M^{-1/3} \tag{1.3}$$

[6]. This inverse relationship between the mass and radius of a WD happens due to increased gravitational pressure for more massive WDs. The most massive theoretical WD, which would be just below the Chandrasekhar limit, would compress the electron-degenerate core to its minimal possible size; any smaller would activate runaway nuclear burning en route to going SN. WDs are the expected final evolutionary stage of more than 97% of stars in the Milky Way [41].

The cooling process of WDs is mostly straightforward, given their relatively simple structure. As WDs cool, however, the motion of ions in the core is influenced more and more by Coulomb interactions. An important quantity is the Coulomb coupling parameter

$$\Gamma = \frac{Z^2 e^2}{k_B T} \left(\frac{4\pi n_i}{3} \right)^{1/3}, \tag{1.4}$$

for atomic number Z, electon charge e, and ion number density n_i [64]. Γ is a

measure of the kinetic energy of particles in a system and their ability to move unimpeded. As the ions cool, they will eventually pass a threshold value of Γ, estimated to be around 175 [133], at which point the core will begin to crystallize as the ions arrange themselves in a lattice. This crystallization process releases energy as latent heat during the liquid to solid phase transition. This release of latent heat leads to a delay in the cooling of the WD, resulting in a buildup of WDs on the HR diagram known as the Q branch [133], illustrated in Fig. 1.4 using WDs within 200 pc from the Gentile Fusillo et al. [49] catalogue. WDs have been dereddened using each sources mean A_V from the catalogue.

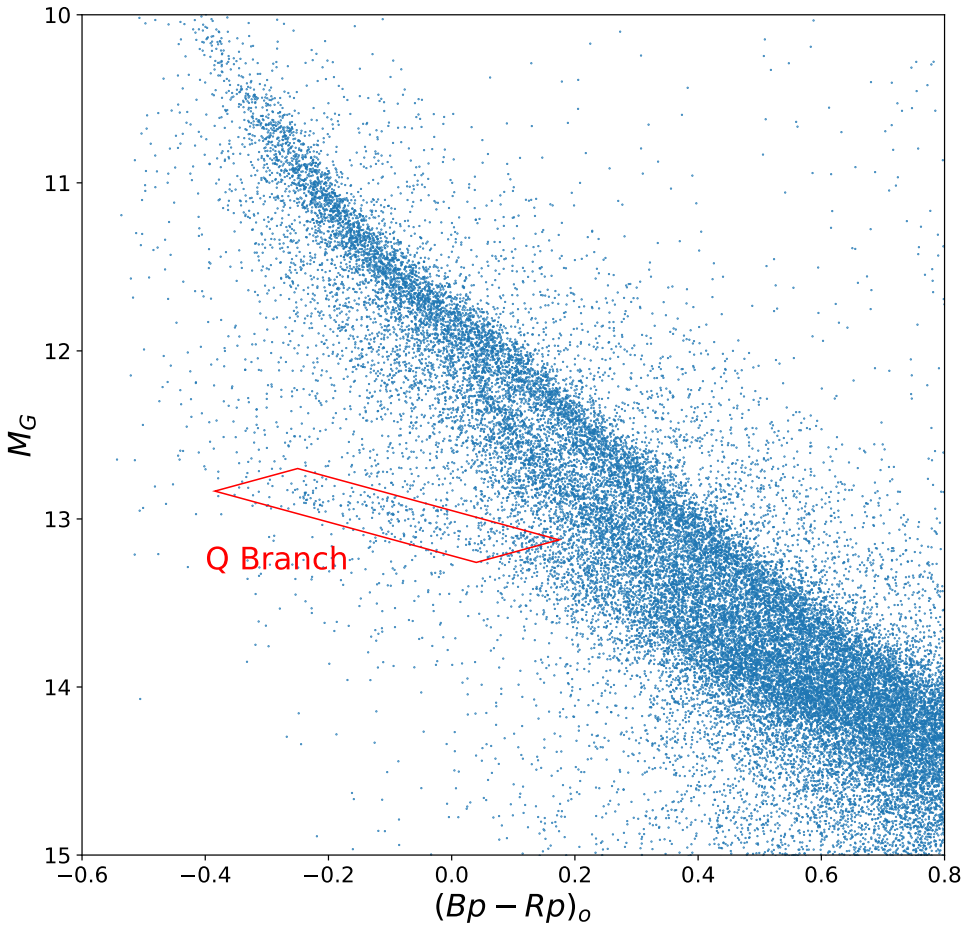

Figure 1.4: Sample of WDs within 200 pc from the Gentile Fusillo et al. [49] catalogue. The approximate Q branch overdensity is indicated in red.

Recent evidence suggests that a fraction of ultramassive white dwarfs, defined here as those with $M > 1.05$ $M_{\odot}$, experience an additional delay of 8 Gyr compared with their lower mass counterparts [18]. Latent heat from crystallization had already been considered for WD cooling models, but a second aspect was largely missed; gravitational energy released due to phase separation. One potential explanation for this additional cooling delay in ultramassive WDs is Ne sedimentation due to phase separation [18]. The most massive WDs have either primarily CO cores with smaller amounts of Ne, or primarily ONe cores. Depending on the makeup of the core, Ne may settle towards the centre of the WD as a result of experiencing increased gravitational forces. Camisassa et al. [19] examined this possibility and found that Ne sedimentation does not account for the increased cooling delay for ONe core WDs but that it could for ultramassive WDs with primarily CO cores and lower Ne fractions. Determining the white dwarf's progenitor mass relies on accurately determining both the WD and its host cluster's ages. As such, additional studies on WD crystallization and phase separation are crucial for developing accurate WD cooling models.

1.2.1 Atmosphere

The atmospheric composition of a WD is a critical component as it is the only part of the WD that is visible to observers through spectroscopy. The composition of the stellar atmosphere allows one to model properties of the atmosphere to study critical aspects of the WD, including its effective temperature and the strength of its surface gravity. In a 1948 paper, Schatzman [119] showed that gravitational settling due to high surface gravity led to elements in WD envelopes being largely separated, with the lightest elements in the outermost layers. As a result, the atmosphere of the majority of WDs is primarily H-rich, dominating stellar emission. These hydrogen atmosphere WDs are called DA WDs, with approximately 80% of WDs being spectroscopically confirmed to have this atmospheric composition. [1].

Of the remaining WDs, the vast majority have He-dominated spectra [26]; we refer to these as DB WDs if only He I lines are present and DO if He II lines additionally appear. He atmosphere WDs form due to the remaining H burning in

the post-AGB phase in stars that experience the late thermal pulse. He atmosphere WDs also form from the evolution of low mass stars with M$<$ 0.5 $M_{\odot}$, as a result of these stars burning all of their H on the MS but being unable to fuse He. The Universe is too young to have formed any of these low mass helium WDs via single star evolution, though some have been formed due to experiencing mass loss in a binary system [65]. Particularly cool He WDs often have no identifiable emission lines and are called DC WDs. When the very late thermal pulse occurs early in the WD cooling phase, it leads to convective mixing of heavier elements from the core into the atmosphere [32]. This rare situation can create He WDs with notable carbon emission classified as DQ WDs.

Though high surface gravity leads to most WD atmospheres being dominated by a single element (H or He), between 25 and 50% reveal trace amounts of heavier metals in their spectra [75]. The presence of these metals is believe to be a result of circumstellar debris through accretion of tidally disrupted planets [134]. Accurate modeling of WD atmospheres has to take into account the potential presence of these traces of heavy elements. In this work, we will focus primarily on DA WDs due to model availability of these types of WDs and their high overall occurrence fractions.

1.2.2 Core Composition

While all WDs possess electron-degenerate cores, the composition of the core varies, depending primarily on the mass of the star that generated it. The atmosphere of a WD is easy to determine from its emission; the core of the WD, however, is not visible to observers due to the opacity of the outer layers [32]. Estimating the composition of a WD core relies on understanding stellar evolutionary processes that led to the formation of the WD.

Stars below $\sim$ 0.3 $M_{\odot}$ are fully convective on the MS [5]. This convection carries He to the surface, pushing H down into the core leading to the entirety of the star's H burning while still on the MS. After burning through all available H, these stars will contract but will not reach the point where core temperatures are sufficient for He burning. These stars will continue to contract until electron degeneracy pressure stabilizes the star, forming a He core WD. While this is the

expected fate for all low mass stars, the MS lifetime for this mass range exceeds the current age of the Universe [120]. Hence, no WDs of such low mass have formed from single stellar evolution. The only discovered He WDs with masses lower than 0.3 $M_{\odot}$ are known to come from binary mass loss and are known as extremely low mass WDs (see e.g. [108], [16], and [80]).

If an evolving star has a mass sufficient to ignite He but not C, it will end its life as a CO WD. The specific CO core mass for carbon ignition has a high degree of uncertainty as a result of uncertainties in potential C+C rates in super-AGB stars, with various authors suggesting the minimum CO core mass for off-centre carbon ignition could be as low as 0.93 $M_{\odot}$ or even as high as 1.10 $M_{\odot}$ [24]. More massive stars reaching sufficient temperatures to burn C but not surpass the Chandrasekhar limit typically form ONe core WDs. Ultramassive WDs are generally expected to have ONe cores, although recent studies suggest that CO WDs can enter the ultramassive regime [20]. This might happen because of a reduction in wind rates during the thermally pulsing AGB or due to rotation of the WD progenitor [3]. The fate of super-AGB stars on the cusp of becoming WDs or neutron stars is poorly understood, primarily because of uncertainty in the critical mass loss rate [122].

In rare cases in the AGB phase, a star can reach a high enough temperature in its core for C ignition, but either the second C flash does not occur, or the carbon flame fails to reach the centre of the core. Both cases result in the formation of a CO-Ne core. The mass range required for this hybrid core is likely very narrow [31]. While this limited range could create some exciting hybrid CO-Ne WDs, we will not focus on them due to the scarcity of studies modeling their evolution.

If a WD accretes matter from a companion and surpasses the Chandrasekhar limit, it results in a runaway nuclear reaction and thermonuclear explosion eventually forming a neutron star. Stars exploding in this manner are called type Ia supernovae (SN Ia). Studies suggest that in some cases, deflagration is not strong enough to trigger detonation, in which case the original WD can survive [67]. This failed SN enriches the WD in heavy elements, leaving behind an iron (Fe) core WD.

1.3 Gaia

The development of the white dwarf IFMR has long been a topic of interest in the scientific community. Although WDs are the expected final evolutionary state of approximately 97% of Milky Way stars [41], their low luminosity makes them challenging to identify, with just a few thousand confirmed WDs identified by the end of the 20th century. The launch of the Sloan Digital Sky Survey (SDSS) [141] in the year 2000 increased the number of known WDs to approximately $36,000$ within its first few data releases [34]. Despite this massive increase in known WDs, progress on the IFMR remained slow [23].

The Gaia mission [44] revolutionized stellar astronomy with its first data release in 2016. Gaia is tasked with constructing a 3D map of the Milky Way by measuring astrometry of more than a billion stars with unprecedented precision. The goal includes measuring the parallax, position on the sky, and proper motion of the majority of targeted objects, giving a 5-parameter astrometric solution. Complete 6-parameter phase space information via the inclusion of the radial velocity is expected for a small percentage of targets but not generally those in the magnitude range of most WDs. Gaia measures the G band magnitude for all targets, with a limiting magnitude of G$\sim$ 21. Additionally, Bp and Rp band magnitudes are measured for a subset of targets.

The combination of G, Bp, and Rp band magnitudes allows one to construct a colour-magnitude diagram (CMD), which shows the difference between two band magnitudes on the x-axis and a single magnitude on the y-axis. A CMD is analogous to an HR diagram in that the magnitude difference between two bands is related to the object's temperature and the single magnitude is related to the luminosity. The main stellar evolutionary features on an HR diagram also appear on a CMD. In Fig. 1.5, we show a Gaia DR2 CMD where the observed apparent G band magnitude has been distance corrected to absolute magnitude using each object's parallax.

This CMD was created by querying the Gaia DR2 archive using the data filtering technique described in Gaia Collaboration et al. [45]. The Gaia DR2 archive limits search results to the first three million sources, so while this is not a complete filtered Gaia CMD, it does illustrate the main features. The main sequence is

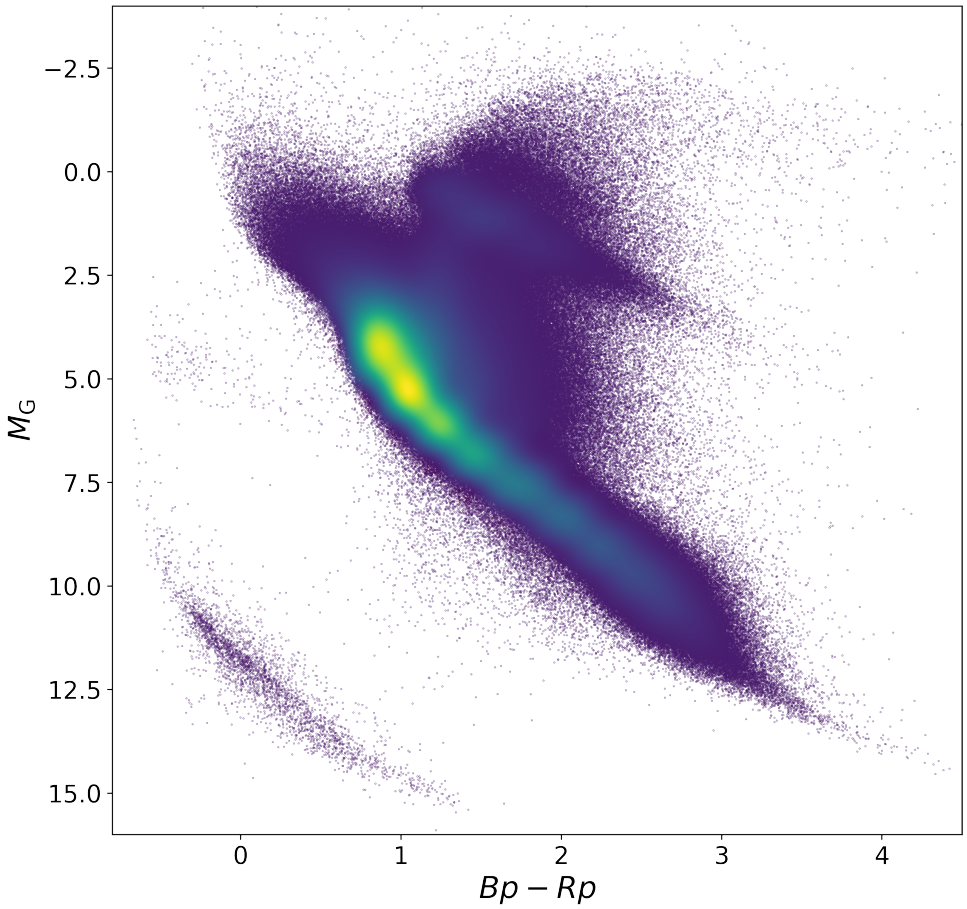

Figure 1.5: Partial Gaia DR2 CMD coloured by density, from low (purple) to high (yellow) density.

identifiable as the plot's densest region, a clustering of likely WDs is seen in the bottom left, and the giant branches are on the top right. Dust along the line of sight between us and observed stars leads to their light becoming redder and dimmer. Only a subset of Gaia sources include estimates of the sources extinction and reddening, include none of the sources dimmer than G $= 17$ [37]. As a result, we do not correct this plot for extinction or reddening. Were we able to, the overall width of the apparent MS would likely be significantly reduced.

Gaia DR1 includes over 1.1 billion sources, but only ~ 2 million have full position and proper motion data, and none of them have Bp or Rp band magnitudes.

Gaia DR2 [46] increased the total number of sources to approximately 1.6 billion, with 5-parameter solutions for more than 1.3 billion and Bp and Rp band magnitudes for a similar number. Gentile Fusillo et al. [48] used a sample of confirmed WDs identified with SDSS to develop a catalogue of WDs in the full Gaia DR2 dataset. They identified $\sim 260,000$ high-confidence WDs, defined as sources given at least a 75% probability of being a WD from their comparison with known SDSS WDs. They replicated this work with the subsequent Gaia data release, Gaia EDR3 [47], and were able to increase their catalogue to $\sim 359,000$ high-confidence WDs [49].

Fleury et al. [40] estimated the mass and cooling age of all high-confidence WDs from the Gentile Fusillo DR2 WD catalogue within 200 pc of the Sun. They estimated that there are $\sim$ 100 WDs with M$>$ 0.95 $M_{\odot}$ and ages less than 250 Myr in this volume. Kilic et al. [74] analyzed massive WDs in the Montreal White Dwarf Database (MWDD, [33]), based on Gaia DR2, and identified 25 WDs that they estimate have masses above 1.3 $M_{\odot}$ if they all possess H atmospheres and CO cores. Gaia has increased the number of known WDs tenfold and also led to the identification of a number of likely ultramassive WDs. However, one issue remains in developing the IFMR; the WD precursor must have been born in a star cluster to determine its initial mass.

1.4 Star Clusters

Collapsing cores in overdense regions of cool molecular clouds are the first stage of star formation. Each of these collapsing cores can form one or multiple protostars, which evolve into stars after appropriate accretion levels. These cool molecular clouds tend to have total masses between $\sim 10^3$ and 10^7 $M_{\odot}$, which can form hundreds or even millions of stars as they use up their available stellar material [76]. Stars born from these clouds tend to have approximately the same age and initial chemical composition, primarily varying only in their initial mass. Many of these groups of similar stars will form gravitationally bound systems after birth, known as star clusters. As these clusters are filled with stars of the same age and chemical composition, they provide the perfect environment to study the different evolutionary paths followed by stars of varying masses.

There are two prominent types of star clusters; globular clusters and open star clusters. Globular clusters are compact, tightly bound associations containing anywhere from tens of thousands to millions of stars. These tightly bound systems were formed from giant molecular clouds early in the galaxy's history and contain among the oldest stars in the Universe [100]. On the other hand, open star clusters are loosely bound associations of hundreds or thousands of stars that formed much more recently. Milky Way globular clusters are primarily found in the galactic halo, while open star clusters tend to lie in the galactic plane.

Globular clusters are characterized by high velocity dispersions, as is expected from the virial theorem, due to their high total stellar mass [107]. This makes it difficult for individual stars to reach the required escape velocity to leave the cluster and, as such, mostly tend to remain within the cluster over cosmic time. By contrast, open star clusters are weakly bound with low velocity dispersions, on the order of 1 to 2 km s^{-1} for young clusters [125], making these systems prone to lose member stars as they age due to low escape velocities. Despite being unbound gravitationally, stars that leave the clusters tend to stay along roughly the same path as the cluster through the interstellar medium.

1.4.1 White Dwarfs in Open Clusters

Ultramassive white dwarfs are the first formed due to the short main sequence lifetime of their progenitor stars. Globular clusters are not ideal for identification of such stars since these high mass WDs will generally have cooled well below the detectability thresholds of modern telescopes. On the other hand, the young age of open clusters makes them a excellent environment to search for ultramassive WDs. The unprecedented breadth of Milky Way astrometric data provided by the Gaia mission makes for an ideal domain to examine open star clusters in search of these rare objects.

There are at least 375 known open clusters within 1.5 kpc of the Sun younger than 1.5 Gyr. Early in this project, I was involved in the late stages of a study by Richer et al. [112] (hereafter R21) that manually identified 219 of these clusters that were evident in proper motion space using Gaia DR2. They searched the entire Gaia DR2 [46] database for high-confidence cluster member WDs for each

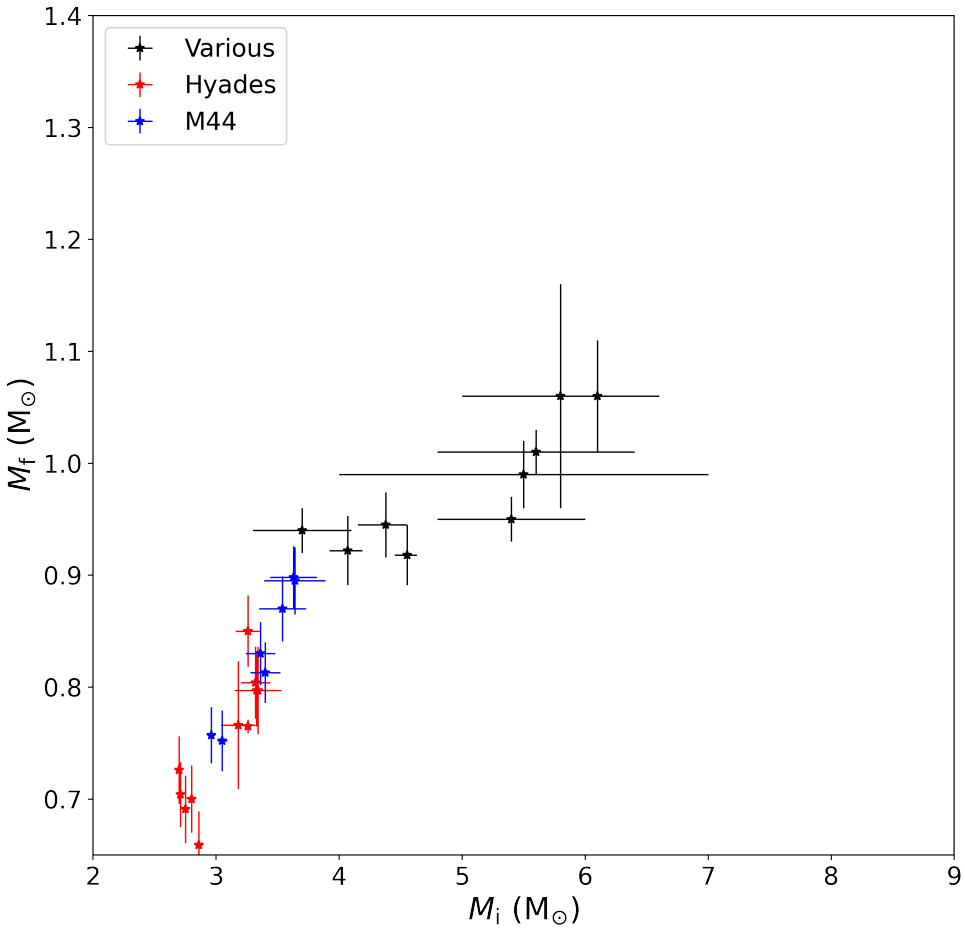

Figure 1.6: The IFMR from R21. Includes WDs discovered in their work as well as those they included from Cummings et al. [29].

identified cluster, where high-confidence required that the WD be within 2σ of the cluster centre in both proper motion and parallax. Despite the large sample of clusters and breadth of data available with Gaia, this search returned just 24 total WDs, with the most massive well below the Chandrasekhar limit. Fig. 1.6 shows the WD IFMR from this work. No WDs with initial masses above 6.1 $M_\odot$ or final masses above 1.06 $M_\odot$ were discovered.

1.4.2 Open Cluster White Dwarf Deficiency

Having identified just 24 WDs in more than 200 clusters, R21 examined the potential WD deficiency by estimating the expected number of WDs which should have formed for a subset of 163 of these clusters. They selected the subset based on the ability to confidently determine the cluster's age, a mandatory prerequisite for estimating the expected WD output. For each of these clusters, they assumed a Kroupa [77] (IMF). They integrated the IMF up to a defined maximum WD progenitor mass to determine an expected number of WDs that should have formed, scaling the results for each cluster based on the number of identified stars. For a maximum progenitor mass of 8 $M_{\odot}$, they estimated these 163 clusters should have produced approximately 1100 WDs; a higher maximum mass would only increase the number of expected WDs. While the Gaia detection threshold of $G = 20.7$ [44] would lead to some WDs being undetected, the gap between the detected WDs and the expected WDs suggests a large deficiency.

Evidence for a deficiency of WDs in open clusters was presented as early as 1977 by Weidemann in a study of mass loss in the Hyades cluster, suggesting that approximately half the cluster WDs were missing [135]. In follow-up work in 1992, Weidemann estimated that the Hyades should have formed at least 28 WDs, with just seven confirmed at the time [137]. Recent extensive studies of the Hyades with Gaia DR2 have slightly increased this number to 11 high-confidence cluster member WDs [116]. The estimate of 28 WDs was determined using a very conservative estimate of 6 $M_{\odot}$ as the cutoff mass for WD formation. Using the Kroupa IMF, the expected number of WDs would increase to roughly 36 and 47 for 8 $M_{\odot}$ and 12 $M_{\odot}$ cutoffs, respectively [77]. If the upper limit for WD production is somewhere between 8 and 12 $M_{\odot}$, these findings suggest that between 75 and 81% of Hyades WDs are missing. Extensive studies of other young open clusters have returned similar deficiencies (see e.g. [110], [68], [69], and [139]).

A significantly lower limit for WD production could explain the deficiency, but that would only further increase the discrepancy between theory and observed SN II rates [78]. This would also not be consistent with the most massive cluster WDs identified thus far [112]. Another possible explanation comes from considering the percentage of WDs that are in binary systems. Prior estimates suggest anywhere

from 20 to 50% of WDs may be in binary systems [38]. A study of the full sample of Gaia DR1 WDs in the local neighborhood estimated the binary fraction as approximately 25% [131]. The authors of that work note that the binary fraction of WDs seems to lag behind the MS-MS binary fraction of roughly 50%, suggesting that the difference is primarily a result of mergers in WD binary systems.

Evidence suggests that the binary fraction of WDs is heavily related to WD mass. Multiple studies of WDs with $M \leq 0.25$ $M_\odot$ found that the binary fraction for these extremely low-mass WDs is 100% (see [72] and [15]), while studies of $M \leq 0.45$ $M_\odot$, $0.5 \leq M \leq 0.7$ $M_\odot$, and $0.7 \leq M \leq 1.1$ $M_\odot$ WDs find binary fractions of 70% [14], > 36%, and > 6% [60], respectively. These results suggest that binaries may account for many of the missing lower mass WDs but that the high mass WDs missing from the WD IFMR are not similarly accounted for. While binarity and the detectability threshold of Gaia would likely account for many of the missing WDs, these do not seem to tell the whole story. Something else must cause for the dearth of high mass WDs in open clusters.

1.5 White Dwarf Natal Kicks

To explain the deficiency of white dwarfs in open clusters, Fellhauer et al. [38] considered an alternative where the dearth occurs due to the white dwarf receiving a natal velocity kick of a few km s^{-1}. The low velocity dispersion of open clusters would allow even a modest kick all the star to exceed the cluster escape velocity and propel the WD out of the cluster. WD natal kicks could occur due to asymmetric mass loss in the AGB phase that precedes WD formation [42].

Periodic expansion and contraction happens in the AGB phase because of thermal pulsation driven by helium shell flashes. This stellar pulsation leads to atmospheric shock waves propagating outwards and levitating gas from the stellar surface [86]. The levitated material reaches distances above the surface, where lower temperatures and increased density enable the material to cool and condense into dust grains [82]. The newly formed dust grains are then accelerated outwards by interactions with stellar photons, transferring momentum to the dust and forming a stellar wind [82].

These winds collide with the interstellar medium, enriching it in chemical ele-

ments and driving mass loss in the AGB phase. The mass loss rate is largely driven by pulsation amplitude and not as a result of the strength of the radiation pressure [86]. Developed stellar winds have velocities of approximately 5 to 30 km s^{-1}, with typical mass loss rates of 10^{-7} to 10^{-4} $M_{\odot}$ yr^{-1} [99]. Given these rates, even a small deviation from spherically symmetric mass loss can lead to a velocity kick of a few km s^{-1} for the most massive formed WDs. AGB winds have not been directly observed, but the resulting mass loss has been. Both spectroscopic observations and imaging of AGB stars reveal a non-spherically symmetric distribution of gas and dust around these stars, supporting asymmetric mass loss (see e.g. [95], [140], [127], [109], and [96]).

Fellhauer et al. [38] performed N-body simulations of intermediate-mass open clusters with differing levels of asymmetric mass loss in the AGB phase. They showed that just a 1% asymmetry in mass loss rate in the AGB phase would lead the newly formed WD to receive a sufficient velocity kick to escape the cluster. For a kick of just a few km s^{-1} a loosely bound cluster, consistent with most open clusters, would lose nearly all of its WDs. They found that the required speed for the cluster to lose most of its WDs is roughly twice the velocity dispersion of the cluster.

Loyola and Hurley (2013) studied the dissolution of star clusters using N-body simulations of clusters that evolved for 4 Gyr. [90]. They found that the most likely escapees within this 4 Gyr period were MS stars with $M \leq 0.7$ $M_{\odot}$ and WDs. They also found that the WDs were more likely to receive a high velocity ejection because they tend to form in the cluster's centre. This factor is vital for the most massive WDs, as the most massive stars in a cluster tend to gravitate towards the centre of clusters, where they impart energy onto their lower mass counterparts, pushing them away from the cluster centre. Their results support that the most massive WDs will likely leave open clusters rather quickly.

Observational and theoretical studies support WDs receiving a sufficient velocity kick at birth to escape their birth clusters. These natal velocity kicks could be the reason for the scarcity of high mass WDs found in clusters. Searches for cluster WDs must extend beyond the cluster virial radius. A kick of just 5 km s^{-1} could take the WD roughly 500 pc away from the cluster in 100 Myrs, so many of these massive WDs may be found very far from their birth clusters. Evidence strongly

suggests that escaped cluster member ultramassive WDs are out there; we merely have to locate them.

Chapter 2

General Procedure

In this chapter we describe the general procedure we used to identify and characterize candidate WDs.

2.1 Candidates

We use data from Gaia DR2 [46] and later Gaia EDR3 [47] to search for candidate ultramassive white dwarfs. R21 previously considered the survey of nearby young open clusters for cluster member massive WDs with Gaia DR2. Gaia EDR3 improves the accuracy of proper motion and parallax measurements by approximately a factor of two compared with DR2. While we primarily focus on identifying potentially escaped WDs, we allow for the possibility that some WDs may have been missed by R21 but appear in similar searches of the EDR3 database. To be considered a cluster member, a candidate must be within 2σ of the cluster centre in parallax and proper motion space. While search criteria ensure that candidates are close to the cluster in position space, no strict cut in this space was made.

Here we outline the cluster identification process, mainly following the technique used in R21. We start with the cluster centre position and parallax as determined in R21. One drawback to the manual identification method employed by R21 is that it requires that the cluster is visually identifiable in proper motion space, which was not the case for 167 of the 386 nearby young clusters surveyed. If the cluster was not manually identifiable in proper motion space, R21 instead used

centre parameters determined from the automated method of Cantat-Gaudin et al. [21], although this only included approximately 50 of the 167 missed clusters.

Using this cluster centre, we search the entire Gaia DR2 database for sources within a circle of 2x the cluster diameter from the centre, where the diameter is as defined by WEBDA[1]. In rare cases, the search returned more than the three million source maximum of the Gaia archive, in which case we add a restriction on the parallax. We remove sources further than 2σ from the centre in either parallax or proper motion, accounting for both the source and cluster centre error. Sources with Gaia photometric excess factor $C \geq 1.5$ are removed, given by

$$C = \left(\frac{I_{\mathrm{Bp}} + I_{\mathrm{Rp}}}{I_G} \right), \tag{2.1}$$

for flux I [37]. C significantly greater than one indicates high photometric imprecision [37]. Particularly faint sources with imprecise photometry tend to have high photometric excess factors and can be confused with candidate massive WDs. Removing these sources reduces contamination and provides a cleaner CMD.

Gaia EDR3 [47] was released after this project had begun. During this project, it was sometimes necessary to reexamine a particular young cluster with EDR3. For these, we start by searching 2x the WEBDA diameter around the R21 cluster centre as with DR2. G band magnitudes for results with 6-parameter solutions fainter than $G = 13$ are corrected using the algorithm recommended by Riello et al. [113] (see the appendix of [47]). While cutting based on the photometric excess factor was recommended for DR2, Riello et al. [113] suggest a more involved process with EDR3 data to overcome potential bias from the colour dependence of the DR2 cut method. To do so, one should calculate the corrected flux excess factor, as in

$$C^* = C - f(G_{\mathrm{Bp}} - G_{\mathrm{Rp}}), \tag{2.2}$$

where the function f corrects for the expected colour excess at a given colour for high-quality sources [113]. The specifics of the colour correction function were determined by Riello et al. [113] using a sample of $\sim 200,000$ well-observed sources; the form of this correction factor and its python implementation is given in the

[1] https://webda.physics.muni.cz/

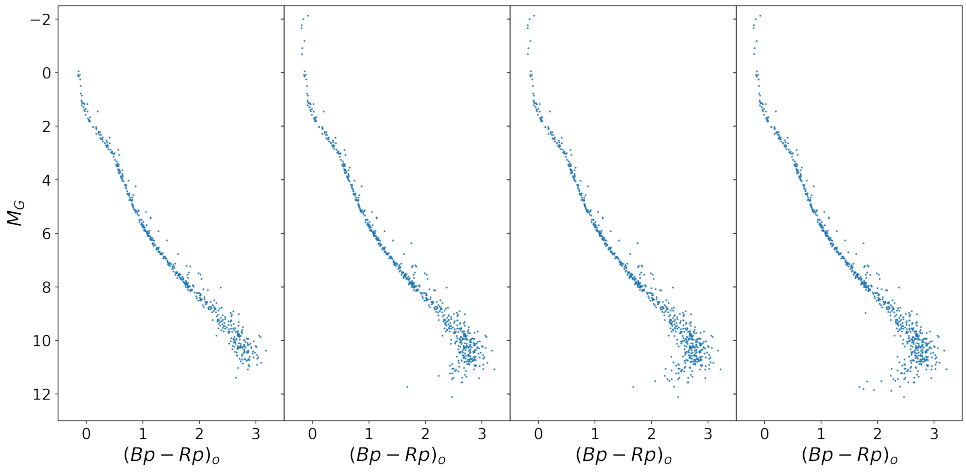

Figure 2.1: Gaia EDR3 CMD of NGC 2422 for corrected excess factor cuts of 1σ (far left), 3σ (middle left), 5σ (middle right), and 10σ (far right).

appendix of Gaia Collaboration et al. [47]. Filtering based on C^* requires first determining the 1σ scatter for well-behaved stellar sources calculated from

$$\sigma_{C^*}(G) = 0.0059898 + 8.817481 \times 10^{-12} G^{7.618399}, \tag{2.3}$$

where the fit parameters were found from a simple power law fit [113] to the bright standards from Stetson [126] and Ivezić et al. [66]. Riello et al. [113] recommend cutting based on $N\sigma_{C^*}$ for objects with $G < 4$, as brighter sources have unreliable colours due to saturation. More restrictive cuts on $N\sigma_{C^*}$ tend to provide a cleaner CMD at the cost of completeness.

Fig. 2.1 illustrates the impact of excess factor cuts on the CMD of the NGC 2422 open cluster. While the most restrictive cut (far left) returns the cleanest CMD, it also loses most of the stars near the MSTO. We find that a cut of 3σ (middle left) gives the best balance between completeness and reducing contaminates. A cut of this level tends to retain the majority of upper main sequence stars while significantly reducing lower MS contaminates. For consistency, we use this cut for all EDR3 analyses in this work. As a final correction, we adjust for the Gaia EDR3 parallax zero-point as described in Lindegren et al. [83].

After performing these corrections, we redetermine the cluster's centre. Fol-

lowing the procedure of R21, we fit Gaussian functions to a kernel density estimate (KDE) of the cluster proper motion to identify the cluster centre using a least square fitting method. We cut the data set to only sources within 2σ of the determined cluster centre. We repeat this process for the parallax using this newly restricted dataset, again imposing a 2σ cut. Finally, we fit a Gaussian to a KDE of the positions of the remaining sources to determine the location of the cluster centre. While we employ a position cut to determine the cluster centre, note that the final cluster membership list is based on those that survive the first two cuts in proper motion and parallax. The original search region ensures that no cluster member stars are found far from the cluster.

Correcting the colour and magnitude for extinction along the line of sight between source and observer is necessary. For sources in a given cluster, the extinction is approximately the same for all stars; once the cluster reddening and extinction are determined, they can be applied to each source associated with the cluster in the same manner, even if that specific source lacks reddening information. Gaia DR2 only includes estimates for the reddening and extinction of sources with $G \geq 17.068788$ [4], while EDR3 does not include any reddening data. We use estimates for the cluster reddening and extinction developed with DR2 for both DR2 and EDR3 samples. As described in R21, we estimate the reddening and extinction for each cluster using the variance-weighted mean of the cluster member sources which have complete reddening and extinction data, including 1σ errors, in DR2. The error in the determined mean values was found from the reliability weight-based unbiased sample variance, accounting for the number of sources. This method helps to account for statistical error due to small sample sets. However, we note that the determined values are not particularly reliable in clusters with only a handful of sources with extinction data. We correct the cluster CMD for extinction and distance using

$$M_G = G + 5 - 5\log_{10}(1000/\text{parallax}) - A_G, \tag{2.4}$$

and

$$(\text{Bp}-\text{Rp})_\text{o} = (\text{Bp}-\text{Rp}) - \text{E}(\text{Bp}-\text{Rp}) \tag{2.5}$$

where A_G and E(Bp-Rp) are the cluster centre extinction and reddening, respec-

tively. For stars that meet 2σ cuts in parallax and proper motion, we use the cluster centre parallax, while for escaped former members, we use the source parallax since the source may have travelled far from the cluster centre.

As an example, we show the Gaia EDR3 CMD of the vdB Hagen 99 open cluster in Fig. 2.2b. The tight MS gives strong support for cluster membership of the identified stars. We see that no giant stars are present in the cluster, although it appears the brightest cluster stars are reaching the main sequence turnoff and preparing to ascend towards the giant branches. There is a single candidate cluster member ultramassive WD in the bottom left corner. Fig. 2.2a shows the position, parallax, and proper motion of the identified cluster member stars relative to the cluster centre. Some cluster members are more than 2σ away from the cluster since no cut was made in position space, though we see that none are more than 2.5σ away.

Gaia colours and magnitudes are useful for initial candidate selection from CMDs. A slight colour change can significantly impact estimates of the WD's mass and cooling age, so reducing this error is essential. Precise mass and age estimates dictate the use of high signal-to-noise ratio (SNR) spectroscopic observations of the source. Once identified from a Gaia CMD, we observe particularly compelling candidates with an appropriate telescope, reducing and analyzing the resulting spectra. We detail the methodology and resulting observations in Ch. 4.

2.2 Atmospheric Parameters

The next step is determining the observed candidates' surface gravity log g and effective temperature $T_{\rm eff}$. Thanks largely to techniques developed by Bergeron et al. [8], accurate atmospheric parameters can be obtained by comparing model atmospheres to spectroscopic observations. Before modeling, the WD atmosphere type is determined by examining the absorption features of the spectra. Since gravitational settling leads to a single element typically dominating WD atmospheres [119], the type is generally readily apparent from the presence of specific absorption lines and rarely requires detailed analysis. In this work, every WD we observed and analyzed was a H atmosphere DA WD indicated by the presence of Balmer lines and no other dominant features. We will focus on analyzing these DA

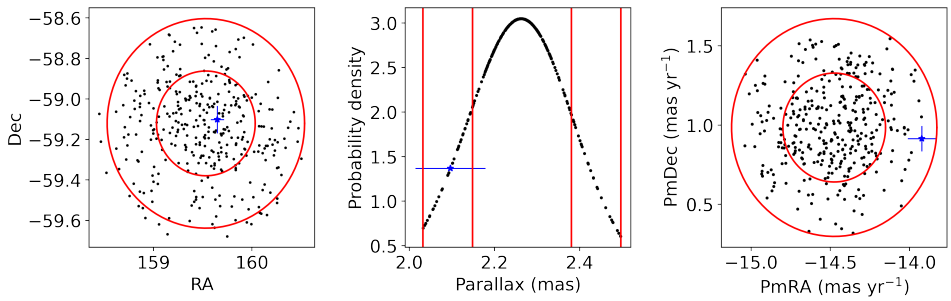

(a) Position (left), parallax (middle), and proper motion (right) relative to cluster centre for identified cluster members, with cluster centre 2σ bounds in red. Candidate ultramassive WD and its error bars indicated in blue.

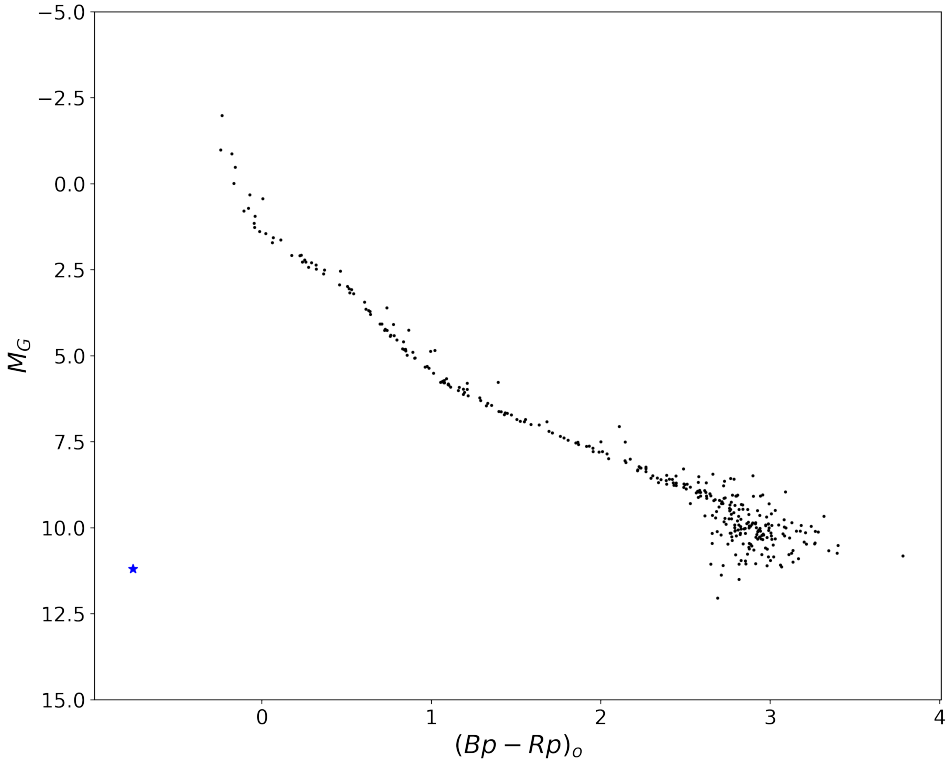

(b) Dereddened colour-magnitude diagram for identified cluster members. Candidate ultramssive WD indicate in blue in bottomn left corner of diagram.

Figure 2.2: Gaia EDR3 cluster members for vdB Hagen 99.

WDs for the remainder of this work. Our search in no way dictated that candidates must have a H-dominated atmosphere; this result is merely a product of the vast majority of WDs possessing these atmospheres [1].

We employ a fitting technique to the Balmer lines similar to that described in Liebert et al. [81]. We start by fitting a grid of spectroscopic models multiplied by a polynomial in wavelength of up to 9th order, including a wavelength shift and zero point, to account for potential continuum calibration errors. We use the steepest descent non-linear least squares fitting method developed by Levenberg-Marquardt (see [89]). The spectrum is normalized using this function by picking points at a fixed distance from each line centre to normalize the flux from each line. Finally, using our grid of model spectra, we determine log g and $T_{\rm eff}$ for the WD from the simultaneous fitting of these normalized line profiles, again using the Levenberg-Marquardt method.

For most WDs, we utilize the pure H atmospheric models of Tremblay et al. [132]. These models assume non-local thermodynamic equilibrium (NLTE), where the atmosphere is in equilibrium overall but is not assumed to be at any given altitude. For hotter WDs, pure H atmosphere models sometimes struggle due to the so-called Balmer line problem, where simultaneously fitting the Balmer lines proves problematic due to inconsistencies between individual line fits. In particular, the fit to Hα gives a significantly lower $T_{\rm eff}$ than Hδ, with the intermediate lines falling between the two [91]. Werner (1996) [138] found that the Balmer line problem was due to metal levitation in the radiation field of particularly hot WDs. This metal levitation polluted the atmospheres with heavier elements, leading to stark broadening of the Balmer lines, particularly Hβ through Hγ.

Werner solved this problem by introducing CNO at solar abundance in the atmosphere to account for metal levitation, allowing for simultaneous fitting of the Balmer lines. If the temperature of the WD was $> 40,000$ K, we consider metal-polluted models from Gianninas et al. [50] to account for this problem. As with the pure H models, these models also assume non-local thermodynamic equilibrium. The Balmer line problem is not present in all hot WDs, so we consider both models, only favoring the metal-polluted models in cases where the Balmer line problem impacts the quality of the simultaneous fit.

2.3 Cooling Models

Once log g and $T_{\rm eff}$ are determined the next step is to compare to theoretical WD cooling models to estimate the mass and cooling age of the WD. One challenge with this is the uncertainty in the composition of the core, particularly for ultramassive WDs. Uncertainties, particularly in mass loss rates in the super-AGB phase, lead to uncertainty in the minimum core mass for off-centre carbon ignition, determining whether the star forms a CO or ONe WD.

To account for these two different core compositions we employ both Camisassa et al. [18] ONe core models and Bédard et al. [7] CO core ones. Camisassa et al. [18] models use the LPCODE stellar evolution code (see [2]). Models were computed for final WD masses of 1.10 $M_{\odot}$, 1.16 $M_{\odot}$, 1.23 $M_{\odot}$, and 1.29 $M_{\odot}$. Bédard et al. [7], on the other hand, developed models using MESA (see [101], [102], [103], [104], and [105]) for 14 final WD masses between 0.306 and 1.233 $M_{\odot}$. The differing implementation of the numerical equations of stellar evolution in LPCODE and MESA give WD cooling ages that differ by less than 2% [118]; as such, development with differing stellar evolution codes is not a cause for concern.

In both cases, models were calculated using solar metallicity. The clusters we consider are all within 1.5 kpc and thus either in or near the solar neighborhood. The solar neighbourhood displays an apparent spread of metallicity [57], though the young age of these clusters reduces the range of potential metallicities. Metallicity does impact the IFMR, but in a relatively minor way (see [114]). We expect that the assumption of solar metallicity is not likely to seriously impact results.

While we expect that ultramassive WDs most likely possess ONe cores, recent work by Althaus et al. [3] and Camisassa et al. [20] present scenarios for ultramassive CO core WDs. Camisassa et al. [20] examined potential evolutionary channels that include reduced AGB wind rates and rotational impact on degenerate CO cores near the start of the AGB. In their examination, Camisassa et al. [20] found the potential for these channels to develop ultramassive CO WDs. The expectation for their claims is that the uncertainty of WD core type is most important for WDs near 1.05 $M_{\odot}$ [123], with those well below or well above this number being very likely to possess CO and ONe cores, respectively.

Ultramassive DA WDs can exhibit gravitational pulsation instabilities (see e.g.

[128], [115]). These instabilities allow for the examination of the WD's core via asteroseismology. By modeling the pulsation patterns of both ultramassive ONe and CO core WDs, it may be possible in the future to distinguish the makeup of the core. Given our current understanding, we cannot be certain about the core makeup of an ultramassive WD. We will consider both possible models for any WD where the mass appears to be between 1.05 and 1.25 $M_{\odot}$, but expect that those above 1.10 $M_{\odot}$ very likely have ONe cores while those below 1.05 $M_{\odot}$ very likely have CO cores. The range of final masses in these models dictates extrapolating for ONe models with M$<$ 1.10 $M_{\odot}$ or CO models with M$>$ 1.233 $M_{\odot}$, increasing the uncertainty of those results compared with interpolated numbers.

2.4 Progenitor Mass

With the WD final mass and cooling age in hand, the last piece of the puzzle to develop the IFMR is determining the mass of the progenitor star. To do this, we first estimate the age of the associated cluster. We primarily determine the cluster's age via PARSEC isochrones [13] using the Kroupa [77] IMF and literature cluster metallicities. The difference between the determined cluster and WD ages gives the progenitor age. The mass is determined for a progenitor of that age using the PARSEC isochrone tables created with the same methodology.

Given a high degree of uncertainty in isochrone age estimates for many clusters, we additionally source age estimates from the literature. We outline specific age estimates, both from isochrones and otherwise, for clusters with candidate ultramassive WDs in Ch. 5. Though the primary goal of this work is to develop the IFMR, we note that if the uncertainty in the cluster age is too great for a reasonably accurate estimate of the progenitor mass it is still a useful result. These WDs help develop our understanding of the overall prevalence of ultramassive white dwarfs and the ability to identify them both in clusters and as escaped former members.

Chapter 3

Escapee Candidate Selection

This chapter outlines the search criteria used to identify candidate ultramassive WDs in the Gaia catalogues. Promising candidates from these searches are selected for follow-up observation, as detailed in Ch. 4.

3.1 Wide Search

We began by searching for WD escapees from a subset of the clusters examined in R21. This subset was all of the known open clusters with WEBDA ages between 10 and 150 Myrs, and distances between 100 and 800 pc, yielding a total of 40 clusters. The age restriction removes young clusters whose MSTO mass is too high to have formed any WDs and older clusters whose ultramassive WDs would have already cooled below the Gaia magnitude limit. We exclude close clusters because their extent on the sky would make the search radius too large, while WDs in distant clusters become increasingly faint and difficult to identify.

For each of these clusters, we searched the entire Gentile Fusillo et al. [48] WD catalogue for high-confidence WDs (those they estimate have a $> 75\%$ chance of being WDs) within 10x the WEBDA cluster diameter. We will hereafter refer to this as the wide search. Within the 150 Myr timeframe of the oldest surveyed cluster, a WD with a kick of just 2 km s^{-1} could travel upwards of 300 pc away from the cluster centre, necessitating the wide search radius. The proper motion had to be within 2σ of the cluster centre to be considered a candidate escapee, with

WD and cluster centre error considered. After removing WDs already identified as cluster members by R21, we were left with 992 candidate escapee WDs. Of the 40 surveyed clusters, we identified candidate escapee WDs potentially associated with 19 of them. Tab. 3.1 lists the cluster parameters for each of the clusters used in the wide search; the WEBDA age and distance were used to determine the original cluster list, while the quantities from R21 define the cluster centre. We did not use the age from R21 to determine the list of clusters to search because the age determination was ongoing work during the wide search.

We dereddened each candidate in the wide search using the cluster reddening value determined in R21. The cooling age and mass of any cluster WD members were estimated using the python package WD_models[1]. WD_models estimates WD parameters using interpolation of selected WD cooling model grids. For $M \geq 1.0$ $M_\odot$ we use Camisassa et al. [18] ONe core models, while those with $M \leq 1.0$ use Bédard et al. [7] CO core models. The ONe core models have a maximum mass of 1.28. The evolution of extremely high mass WDs is poorly understood, so WD_models does not extrapolate beyond the grid. WDs whose mass appears to be above 1.28 $M_\odot$ are estimated as > 1.28 $M_\odot$ with no specific mass and no cooling age determined. We show the CMD of all candidates in Fig. 3.1, with previously described cooling tracks for masses from 0.2 to 1.28 $M_\odot$ and cooling ages between 10 Myr and 1 Gyr.

To narrow down the list of potential escaped WDs, we restrict ourselves to only those whose cooling age from its upper bound mass estimate is less than the cluster age plus 1σ error as given by R21; older WDs cannot have formed in the cluster. Additionally, we estimate the progenitor mass using the Cummings et al. [29] IFMR and remove candidates whose progenitor mass is more than 3σ less than the cluster main sequence turnoff. This cutoff is made particularly loose because of the assumption of a specific IFMR, leading it to remove extreme outliers only. For some objects, the upper mass estimate was outside the model grid range of 1.28 $M_\odot$ and gave no age determination. The CMDs for these candidates were visually examined to determine if the candidate warranted inclusion. The above cuts reduced the original sample from 992 to 151 candidate WD escapees.

[1] https://github.com/SihaoCheng/WD_models

Table 3.1. Wide Search Clusters

Cluster	WEBDA			R21					
	Age [Myr]	Dist. [pc]	Diam. [am]	Age [Myr]	Parallax [mas]	Ra [deg]	Dec [deg]	Pmra [mas yr^{-1}]	Pmdec [mas yr^{-1}]
(1)	(2)	(3)	(4)	(5)	(6)	(7)	(8)	(9)	(10)
Alessi 5	51	398	36.0	$80 \pm 20^{\dagger}$	2.2 ± 1.7	160.8 ± 0.9	-61.1 ± 0.6	-15.3 ± 0.5	2.6 ± 0.4
Alessi 8	83	575	37.2	$100 \pm 30^{\dagger}$	1.5 ± 0.2	232.6 ± 1.4	-51.3 ± 1.0	-5.9 ± 0.2	-5.7 ± 0.2
Alessi 12	79	537	60.0	$100 \pm 40^{\dagger}$	1.8 ± 0.4	310.9 ± 0.8	23.8 ± 0.7	4.4 ± 0.2	-4.6 ± 0.2
Alessi 19	112	550	90.0	$110 \pm 90^{\dagger}$	1.5 ± 0.3	275.2 ± 2.1	11.9 ± 1.9	-1.0 ± 0.2	-7.0 ± 0.2
Alessi 21	30	500	60.0	$60 \pm 20^{\dagger}$	1.7 ± 0.2	107.7 ± 0.7	-9.4 ± 0.7	-5.5 ± 0.2	2.6 ± 0.2
Alpha Per	71	185	300.0	$51 \pm 25^{\ddagger}$	5.7 ± 0.2	52.3 ± 1.4	48.6 ± 1.2	22.7 ± 1.2	-26.0 ± 1.2
ASCC 113	138	450	56.4	$240 \pm 40^{\dagger}$	1.8 ± 0.1	318.0 ± 0.7	38.6 ± 0.7	0.8 ± 0.2	-3.7 ± 0.2
Blanco 1	63	269	70.0	$105 \pm 50^{\ddagger}$	4.2 ± 0.4	1.0 ± 0.8	-29.9 ± 0.8	18.7 ± 0.5	2.6 ± 0.5
Collinder 121	11	471	89.0	$20 \pm 10^{\dagger}$	1.1 ± 0.2	104.1 ± 1.4	-24.3 ± 1.4	-2.8 ± 0.2	3.4 ± 0.2
Collinder 132	12	472	80.0	$25 \pm 12^{\ddagger}$	1.3 ± 0.3	110.7 ± 2.5	-31.3 ± 2.6	-3.9 ± 0.2	3.7 ± 0.2
Collinder 135	26	316	50.0	$26 \pm 13^{\ddagger}$	3.3 ± 0.3	109.3 ± 1.1	-36.9 ± 1.1	-10.1 ± 0.4	6.2 ± 0.4
Collinder 140	35	405	29.0	$35 \pm 15^{\dagger}$	2.5 ± 0.5	111.2 ± 1.1	-32.3 ± 1.0	-8.0 ± 0.6	4.8 ± 0.5
IC 348	44	385	7.0	$12 \pm 6^{\ddagger}$	3.1 ± 0.3	56.1 ± 0.1	32.2 ± 0.1	4.3 ± 0.9	-6.7 ± 0.8
IC 2391	46	175	60.0	$29 \pm 14^{\ddagger}$	6.6 ± 0.2	129.2 ± 1.3	-52.6 ± 1.2	-24.0 ± 1.1	23.5 ± 1.3
NGC 1647	144	540	40.0	$200 \pm 50^{\dagger}$	1.7 ± 0.2	71.5 ± 0.4	19.1 ± 0.4	-1.0 ± 0.4	-1.5 ± 0.3
NGC 2232	53	359	45.0	$18 \pm 8^{\ddagger}$	3.1 ± 0.3	96.9 ± 0.7	-4.8 ± 0.7	-4.7 ± 0.3	-1.8 ± 0.3
NGC 2422	73	490	25.0	$150 \pm 20^{\dagger}$	2.1 ± 0.2	114.2 ± 0.4	-14.5 ± 0.4	-7.1 ± 0.3	1.0 ± 0.3
NGC 2451A	60	189	120.0	$35 \pm 17^{\ddagger}$	5.2 ± 0.2	115.8 ± 0.9	-38.4 ± 0.8	-21.1 ± 0.7	15.3 ± 0.7
NGC 2451B	44	302	108.0	$41 \pm 20^{\ddagger}$	2.7 ± 0.3	116.2 ± 0.7	-37.9 ± 0.7	-9.5 ± 0.6	4.8 ± 0.5
NGC 2516	113	409	30.0	$200 \pm 60^{\ddagger}$	2.4 ± 0.1	119.5 ± 0.9	-60.8 ± 0.6	-4.7 ± 0.6	11.1 ± 0.6
NGC 2547	36	455	25.0	$32 \pm 16^{\ddagger}$	2.5 ± 0.2	122.5 ± 0.5	-49.2 ± 0.5	-8.5 ± 0.3	4.3 ± 0.3
NGC 2925	71	774	10.0	$129 \pm 62^{\ddagger}$	1.3 ± 0.2	143.3 ± 0.3	-53.4 ± 0.2	-8.5 ± 0.3	5.4 ± 0.2
NGC 3228	855	544	5.0	$30 \pm 15^{\ddagger}$	2.0 ± 0.3	155.3 ± 0.2	-51.8 ± 0.1	-14.8 ± 0.5	-0.7 ± 0.4
NGC 5662	93	666	29.0	$100 \pm 10^{\dagger}$	1.3 ± 0.1	218.8 ± 0.6	-56.6 ± 0.5	-6.4 ± 0.3	-7.2 ± 0.3
NGC 6025	77	756	14.0	$105 \pm 50^{\ddagger}$	1.2 ± 0.2	240.8 ± 0.5	-60.4 ± 0.4	-2.9 ± 0.2	-3.0 ± 0.2
NGC 6124	140	512	39.0	$191 \pm 91^{\ddagger}$	1.7 ± 0.4	246.5 ± 1.0	-40.5 ± 0.6	-0.2 ± 0.2	-2.0 ± 0.3
NGC 6405	94	487	20.0	$35 \pm 17^{\ddagger}$	2.2 ± 0.3	265.1 ± 0.4	-32.2 ± 0.3	-1.3 ± 0.3	-5.8 ± 0.3
NGC 6416	122	741	14.0	$229 \pm 109^{\ddagger}$	0.9 ± 0.1	266.0 ± 0.3	-32.4 ± 0.3	-1.9 ± 0.2	-2.3 ± 0.2
NGC 6425	22	778	10.0	*	1.0 ± 0.3	266.7 ± 0.2	-31.5 ± 0.2	3.8 ± 0.2	-1.7 ± 0.2
NGC 7063	95	689	9.0	$98 \pm 47^{\ddagger}$	1.5 ± 0.3	321.1 ± 0.2	36.5 ± 0.2	1.5 ± 0.2	-2.5 ± 0.2
NGC 7160	19	789	5.0	$15 \pm 7^{\ddagger}$	1.1 ± 0.1	328.4 ± 0.2	62.6 ± 0.1	-3.4 ± 0.2	-1.3 ± 0.2
Pismis 4	34	593	25.0	$120 \pm 58^{\ddagger}$	1.4 ± 0.3	128.7 ± 0.6	-44.4 ± 0.5	-8.2 ± 0.2	5.3 ± 0.2
Pleiades	135	150	120.0	$135 \pm 25^{\dagger}$	7.3 ± 0.2	56.6 ± 1.5	24.1 ± 1.5	19.9 ± 1.4	-45.4 ± 1.5
Stephenson 1	54	390	20.0	$28 \pm 14^{\ddagger}$	2.8 ± 0.2	283.6 ± 0.3	36.9 ± 0.3	1.1 ± 0.2	-3.0 ± 0.2
Stock 23	32	380	21.6	$90 \pm 30^{\dagger}$	1.6 ± 0.2	49.3 ± 1.0	60.2 ± 0.7	-4.3 ± 0.2	-0.9 ± 0.2
Trumpler 10	35	424	29.0	$32 \pm 16^{\ddagger}$	2.3 ± 0.2	131.9 ± 0.8	-42.5 ± 0.7	-12.4 ± 0.4	6.5 ± 0.3
vdB-Hagen 23	14	437	38.4	$55 \pm 20^{\dagger}$	2.2 ± 0.2	123.4 ± 0.4	-36.3 ± 0.4	-7.1 ± 0.4	7.3 ± 0.3
vdB-Hagen 56	17	680	36.0	$35 \pm 15^{\dagger}$	2.3 ± 0.2	133.5 ± 1.2	-43.4 ± 0.8	-12.7 ± 0.7	6.5 ± 0.5
vdB-Hagen 99	40	507	20.0	$40 \pm 20^{\dagger}$	2.2 ± 0.1	159.5 ± 0.6	-59.2 ± 0.4	-14.4 ± 0.4	1.0 ± 0.4
vdB-Hagen 164	14	550	48.0	$20 \pm 10^{\dagger}$	2.2 ± 0.8	222.2 ± 1.1	-66.4 ± 0.6	-7.4 ± 0.5	-10.5 ± 0.6

Notes. Select parameters for clusters examined in wide search. Columns: (1) cluster name; (2-4) age, distance, and cluster diameter (from WEBDA); (5) best fit cluster age from R21. ‡ indicates determination from isochrones, † denotes age determined by Cantat-Gaudin et al. [21], and * indicates no age was determined in R21; (6-10) cluster centre parameters as derived from Gaia DR2 data in R21.

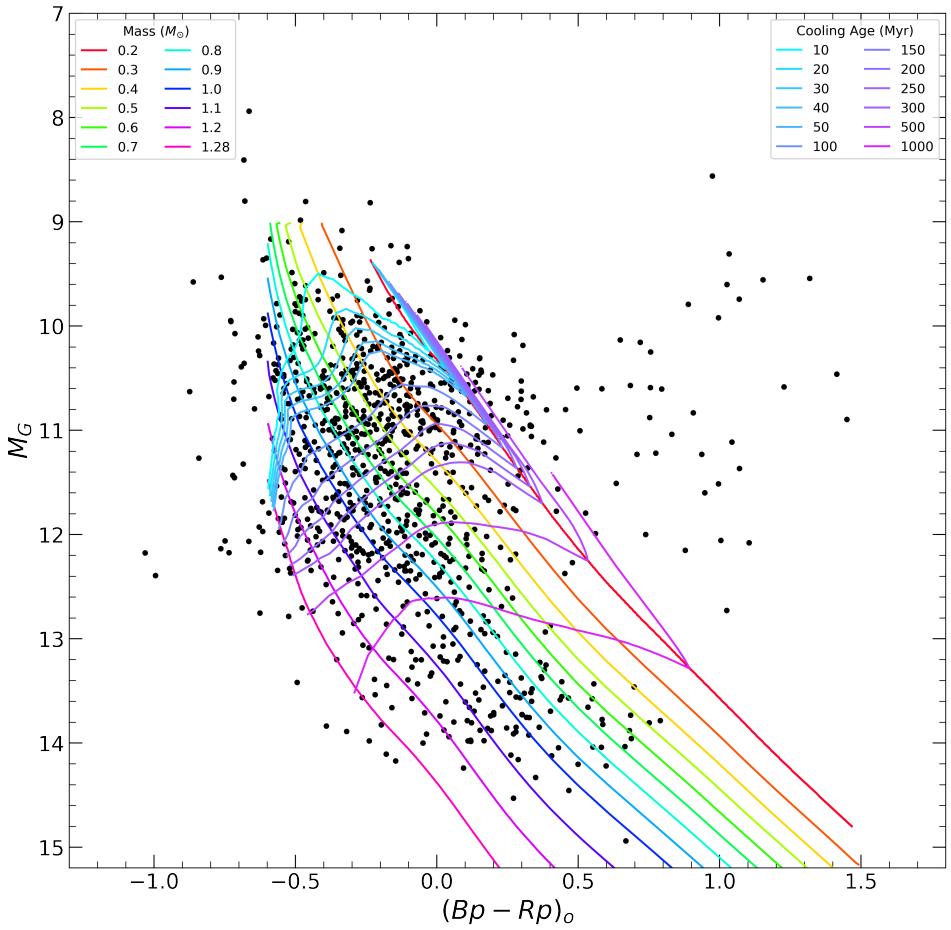

Figure 3.1: Full uncut CMD of candidate cluster member WDs identified in the wide search. Objects dereddened using the cluster reddening values determined by R21. Horizontal tracks are for cooling ages from 10 Myr to 1 Gyr (top to bottom), while vertical tracks display mass models from 0.2 to 1.28 $M_\odot$ (right to left).

Fig. 3.2 shows the cumulative distribution of the square of the WD's distance from the cluster centre for both the discarded and retained candidates. A purely random sample should scale linearly with distance squared, which we see as the general trend for the discarded candidates, while the retained ones prefer being closer to the cluster. This result suggests that a significant fraction of the retained

candidates are not taken from a random sample and may be associated with the cluster. We performed a two-sample Kolmogorov-Smirnov (KS) test to assess the difference between these populations better. A two-sample KS test compares two samples to determine how likely they were drawn from the same distribution. This returned a p-value of 0.094, p values above 0.10 support the samples potentially coming from the same distribution. We cannot strictly rule out these samples being drawn from the same distribution, but this result further suggests that they were not.

To better assess these candidates, it is necessary to examine them spectroscopically. Given the faintness of the WDs, it would take an extreme amount of observing time to obtain spectra of all 151 candidates. With that in mind, we selected a handful of the most promising candidates for follow-up observation. The cumulative distribution shows particular favouritism for distances from the cluster centre between 4 and 8 times the cluster radius, as illustrated by the slope increase in the blue curve of Fig. 3.2. The more distant the slope is from linear on this distance squared plot, the less likely it becomes that those sources were taken from a random sample. We selected six promising candidates within this range for further assessment. The chosen candidates have high estimated WD masses and cooling ages, resulting in sensibly massive progenitors given cluster age estimates from R21 and our current understanding of the IFMR. While we would have liked to follow up on all 151 candidates, it was not realistic, given the significant observation time required to obtain an appropriate SNR for each source. We detail observations of the six selected candidates in Ch. 4.

Tab. 3.2 gives select astrometric and derived quantities for selected candidates. These same parameters for the full list of 151 candidates are included in the the appendix Tab. A.1. We show CMDs illustrating the selection process for the chosen candidates in Figs. 3.3 through 3.6, with the chosen candidates displayed in blue on the right graph. The 1σ error bars illustrate how significantly changes in the object's colour can impact estimates for the mass and cooling age, demonstrating the need for follow-up spectroscopy to properly assess candidacy. These same plots for the 15 clusters with no chosen candidates are included in the appendix, Figs. A.1 through A.15.

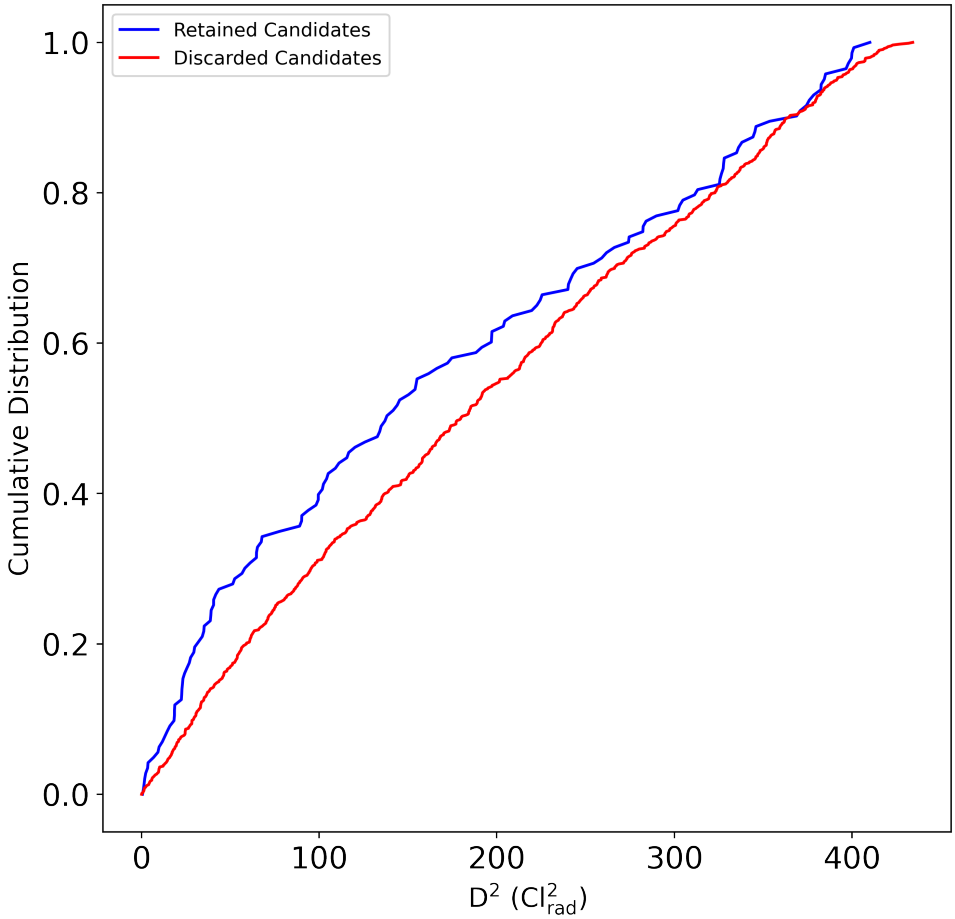

Figure 3.2: Cumulative distribution of the square of the distance from the associated cluster center for the wide search WDs, scaled by the cluster's radius. The blue curve displays the 151 candidates retained after initial cuts, while the red curve shows the 841 discarded candidates.

3.2 Reconstructed Young Clusters

In addition to the wide search, we also employ a technique developed by Heyl et al. [56] (hereafter H21a) which identifies escapee candidates from nearby young clusters by reconstructing the cluster from calculated 3D velocities. Here we provide a guide through of this technique, which H21a originally applied to the Pleiades cluster.

Table 3.2. Wide Search Escapee Candidates Select Parameters

Identifier	Gaia DR2 Source ID	M_G [mag]	$(Bp\text{-}Rp)_o$	Dist. [Cl_{rad}]	Mass [$M_\odot$]			Cooling Age [Myr]		
					Est.	Upper	Lower	Est.	Upper	Lower
(1)	(2)	(3)	(4)	(5)	(6)	(7)	(8)	(9)	(10)	(11)
Alessi 21 WD1	3045185929454409856	11.38	-0.54	6.26	1.17	>1.28	1.00	66.59	...	127.50
Alessi 21 WD2	3050876554961550848	11.19	-0.57	6.37	1.20	>1.28	0.96	14.96	...	99.89
NGC 2422	3028302962770764416	11.51	-0.54	7.17	1.19	>1.28	1.05	80.04	...	141.78
NGC 2451B WD1	5534595188067100032	11.36	-0.55	4.92	1.19	>1.28	1.05	52.67	...	113.83
NGC 2451B WD2	5591693965064811776	11.53	-0.57	5.66	1.24	>1.28	1.09	49.38	...	131.09
NGC 2516	5294015515555860608	11.18	-0.42	5.92	0.96	1.11	0.78	96.54	55.12	123.77

Notes. Select parameters for candidate ultramassive WDs identified in wide search and selected for follow-up observations. Columns: (1) associated cluster name; (2) Gaia DR2 source ID [46]; (3) absolute G magnitude dereddened using cluster reddening from R21; (4) reddening corrected (Bp-Rp) colour; (5) distance from cluster centre in units of cluster radius; (6-8) mass estimate with 1σ bounds for WD from cooling model fits; (9-11) WD cooling age estimate from same model fits.

Starting from an initial guess for the cluster centre position and proper motion, we search the Gaia EDR3 archive for every source within one degree of the cluster centre on the sky. This sample is then reduced to only objects within five mas yr^{-1} of the estimated proper motion. The cluster centre position, parallax, and proper motion are then redetermined from this sample. The cluster radial velocity is calculated as the mean of the sample stars with Gaia DR2 radial velocity measurements since Gaia EDR3 does not include radial velocities. This mean, combined with the derived proper motion, gives an estimate for the mean velocity of the cluster relative to the Sun ($\mathbf{v}_{\rm cluster}$). Using these cluster centre parameters, H21a adjust the sample to include all objects within a pre-selected distance of the cluster centre, chosen as 10 pc in the case of the Pleiades, retaining the requirement of being within five mas yr^{-1} of the cluster centre median proper motion.

The next step was to look for potential escapees in an extended volume around the cluster. The specific volume searched for escapees depends on the position of the cluster, in particular its distance. For the Pleiades, they retrieved every EDR3 source less than 100 pc from the Sun and all within 200 pc that are < 45 degrees from the Pleiades. For each source in this extended sample, they calculate the two-dimensional velocity relative to the cluster via

$$\Delta\mathbf{v}_{\rm 2D} = \mathbf{v}_{\rm 2D} - \mathbf{v}_{\rm cluster} + \left(\frac{\mathbf{v}_{\rm cluster}\cdot\mathbf{r}}{\mathbf{r}\cdot\mathbf{r}}\right)\mathbf{r}, \tag{3.1}$$

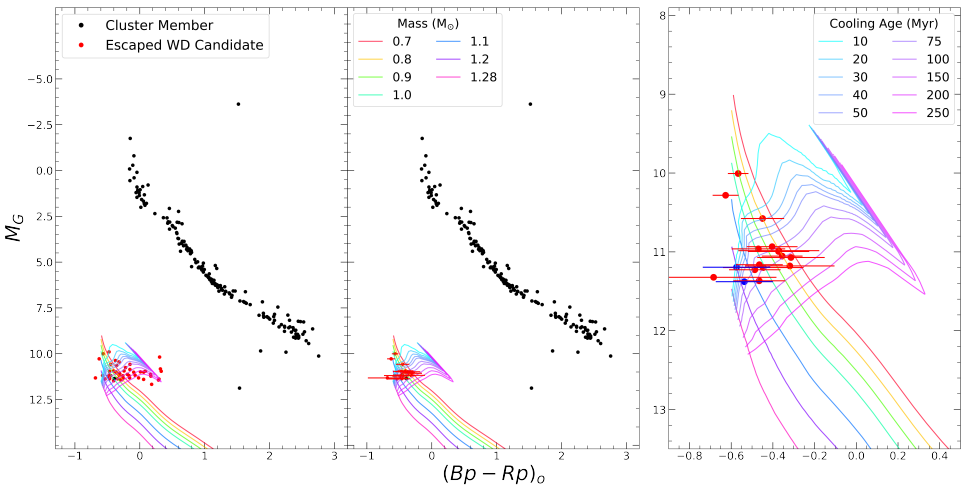

Figure 3.3: CMDs of the Alessi 21 cluster. *Left*: Cluster member candidates from R21 (black), with wide search candidate escapees before data cuts (red). Horizontal tracks are for cooling ages from 10 to 250 Myr (top to bottom), while vertical tracks display mass models from 0.7 to 1.28 $M_\odot$ (right to left). *Middle*: As in left graph, but with post-cut escapee candidates including 1σ error bars. *Right*: Zoom in of the WD cooling sequence from the middle graph, with select candidates for follow-up observation in blue.

where $\mathbf{r}$ is the star's displacement from the Sun, and $\mathbf{v}_{2D}$ is the velocity of the star in the plane of the sky where they have assumed zero radial velocity.

To be deemed a potential escapee, the relative proper motion must be large enough to explain the current position of the star from the cluster centre. A source at a given distance from the cluster must be moving away in that same direction at a sensible rate for past cluster membership to be possible. They determine this by finding the distance of each source relative to the cluster center as a function of time, assuming no relative acceleration, via

$$d(t)^2 = (\Delta\mathbf{r} + t\Delta\mathbf{v} + \hat{r}\delta r)^2, \tag{3.2}$$

where $\Delta\mathbf{r} = \mathbf{r} - \mathbf{r}_{\text{cluster}}$ and $\Delta\mathbf{v} = \mathbf{v}_{2D} - \mathbf{v}_{\text{cluster}}$ with an arbitrary displacement δr.

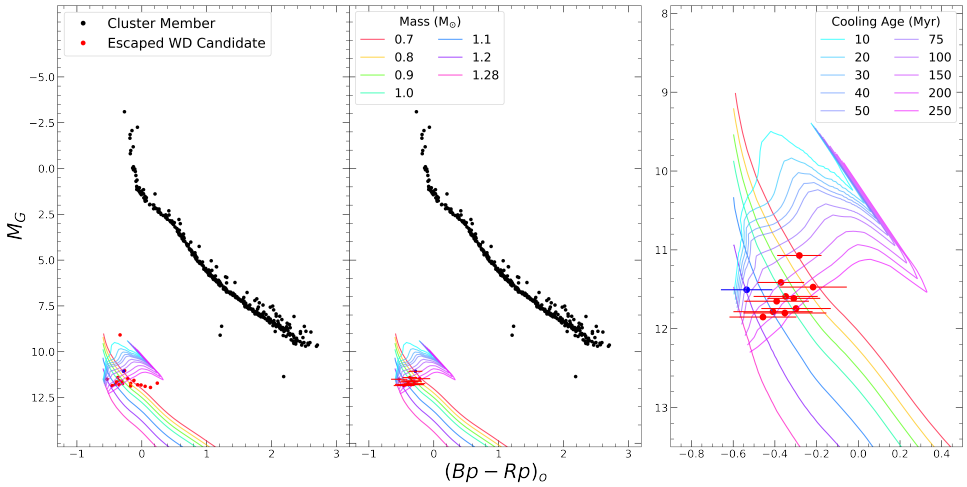

Figure 3.4: Wide search cluster CMDs as in Fig. 3.3, but for NGC 2422.

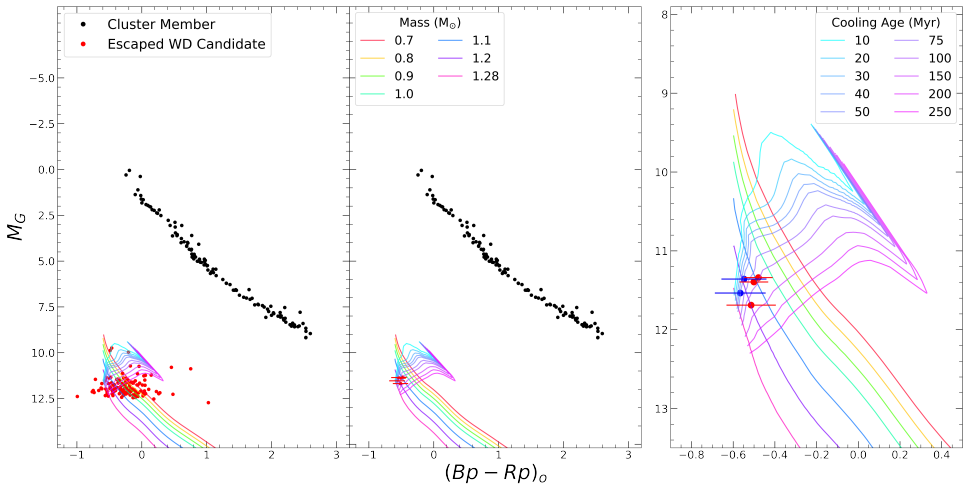

Figure 3.5: Wide search cluster CMDs as in Fig. 3.3, but for NGC 2451B.

From this, they find the time when the source was closest to the cluster centre from

$$t_{\min} = \left(\frac{\Delta \mathbf{r} \cdot \Delta \mathbf{v} - (\Delta \mathbf{r} \cdot \hat{r})(\Delta \mathbf{v} \cdot \hat{r})}{(\Delta \mathbf{v} \cdot \hat{r})^2 - (\Delta \mathbf{v})^2} \right). \tag{3.3}$$

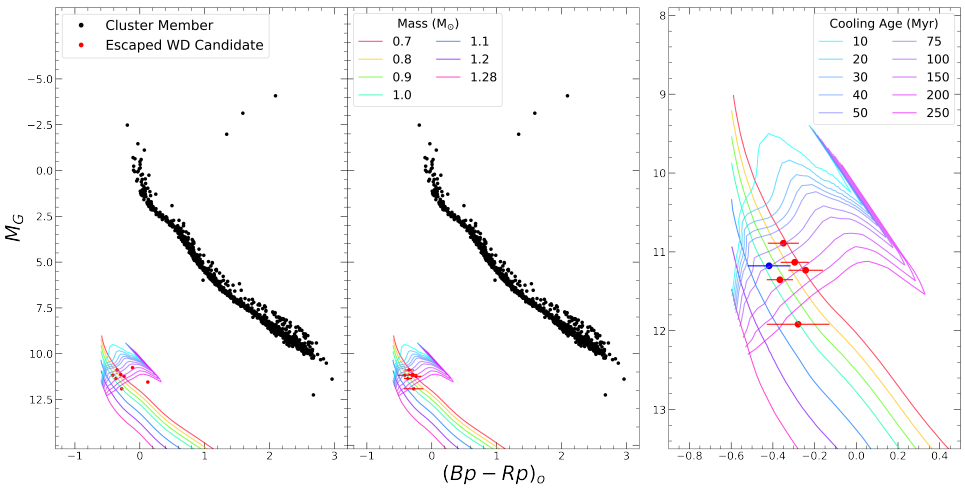

Figure 3.6: Wide search cluster CMDs as in Fig. 3.3, but for NGC 2516.

The minimum time determines the radial displacement from

$$\delta r = -\hat{r} \cdot (\Delta \mathbf{r} + t_{\min} \Delta \mathbf{v}), \tag{3.4}$$

which additionally provides an estimate for the radial velocity of the star $v_r = \Delta r / t_{\min}$. With the radial velocity, they reconstruct the star's 3D velocity vector relative to the cluster centre via

$$\Delta \check{\mathbf{v}}_{3D} = \mathbf{v}_{2D} + v_r \hat{r} - \mathbf{v}_{\text{cluster}}, \tag{3.5}$$

where $\check{\mathbf{v}}_{3D} = \mathbf{v}_{2D} + v_r \hat{r}$ gives the reconstructed 3D velocity of the star.

With the reconstructed 3D velocity, they trace the object's motion relative to the cluster and search for objects close to the cluster in the past. To be considered an escapee, they required that the nearest approach came within 15 pc of the cluster centre. They restrict escapees to those whose relative motion is within 10 km s^{-1} of the cluster centre. Given the cluster's age, they find that a star's maximum relative velocity to be potentially identified as a cluster escapee is 2.36 km s^{-1}.

Notably, they do not consider uncertainties in proper motion, position, or parallax in these calculations. For the Pleiades cluster, they estimate that the proper motion error is approximately 32 to 51 m s^{-1}, which would result in a relative posi-

tion error of 4 to 7 pc over the lifetime of the Pleiades. This uncertainty level is well within the closest approach cut-off, so the error is not troublesome for the Pleiades and other young and close clusters. Using this technique, we can not accurately examine clusters further than about 200 pc or with ages over 200 Myr. None of the selected candidate's clusters from the wide search can be reconstructed using this technique.

From this method, H21a identified three potentially interesting WD escapees from the Pleiades. The H21a technique was additionally applied to the remaining four clusters within 200 pc of the Sun with ages under 200 Myrs in a follow-up paper Heyl et al. [55] (hereafter H21b), of which I am a co-author. In three of the four clusters (NGC 2451A, IC 2391, and IC 2602), no candidate ultramassive WDs were identified, but the last of the four, Alpha Persei, was more promising.

3.2.1 Alpha Persei

The procedure to identify escapees from the Alpha Persei cluster follows the same prescription presented in Heyl et al. [55]; here we mention key results and differences from the initial application to the Pleiades. The Alpha Per EDR3 sample volume includes all sources within 250 pc of the Sun within 28 degrees on the sky of the cluster centre, as well as the nearside hemisphere of objects within 200 pc and 45 degrees, for a total volume of approximately seven million cubic parsecs. From a reduced sample of stars within 1 degree on the sky and within 5 mas yr^{-1} in proper motion, they calculate the cluster centre as

$$\mathbf{v}_{\mathrm{cluster}} = (-13.9 \pm 0.8, -24.2 \pm 0.4, -6.83 \pm 0.2)\mathrm{kms}^{-1}, \tag{3.6}$$

and

$$\mathbf{r}_{\mathrm{cluster}} = (-146.5 \pm 0.7, 93.5 \pm 0.4, -19.9 \pm 0.1)\mathrm{pc}. \tag{3.7}$$

They use the original extended sample to determine each source's reconstructed 3D velocity, distance, and time of closest approach as in H21a. They derived a relative threshold velocity for escapee candidacy of 3.06 km s^{-1} from the cumulative distribution where the true-positive rate equals the completeness rate. Fig. 3.7 displays the results of the H21b search of Alpha Persei. Given the potential uncer-

tainty of estimated WD parameters, we allow for any WD whose mass is estimated to be > 0.84 $M_\odot$ with a cooling age < 250 Myrs. H21b selected two candidates that meet these criteria for additional follow-up, the most massive of which has an estimated mass of ~ 1.2 $M_\odot$.

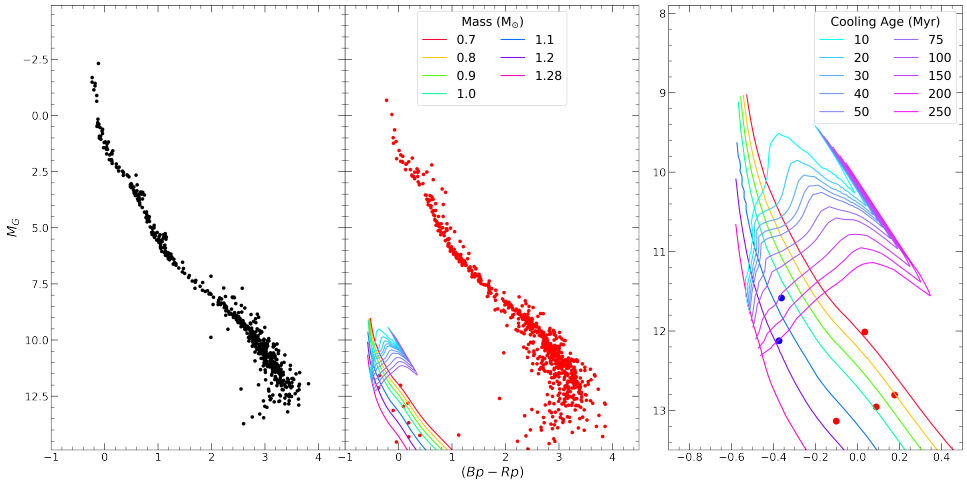

Figure 3.7: Gaia EDR3 CMDs for Alpha Persei cluster from H21b search. *Left*: Cluster members. *Middle*: Escapee candidates. Horizontal tracks are for cooling ages from 10 to 250 Myr (top to bottom), while vertical tracks display mass models from 0.7 to 1.28 $M_\odot$ (right to left). *Right*: Zoom in of the WD cooling sequence from the middle gtaph, with selected candidates for follow-up observation in blue.

In follow-up work, I first-authored a further analysis of Alpha Persei escapees [88]. We expanded on the H21b search to determine the minimum cluster distance, reconstructed 3D velocity, and time of closest approach for the entire Gentile Fusillo et al. [49] WD catalogue. We relax the relative reconstructed 3D velocity requirement to 5 km s^{-1}, and require that the time of closest approach was within the cluster's lifetime, which H21b estimated to be 81 Myrs from kinematics (we will discuss this and other age estimates in Ch. 5). We identified five candidate escapee WDs using these requirements alongside the methodology of H21b. The two candidates identified by H21b were also identified in this search. These two are each currently within 25 pc of the cluster centre, while the three not identified by H21b are each more than 100 pc away.

Fig. 3.8 displays the results of this search, with the five WDs which meet the aforementioned cut criteria indicated in blue. WDs were dereddened using the mean A_V value from Gentile Fusillo et al. [49]. To convert to Gaia band reddening and extinction we use conversion factors $A_V = 3.1$ E(B-V), E(B-V) $= 0.771$ E(Bp-Rp), and E(Bp-Rp) $= 0.486 A_G$ (see [13] and [22]). We present follow-up observations of each of these five ultramassive white dwarf candidates in Ch. 4.

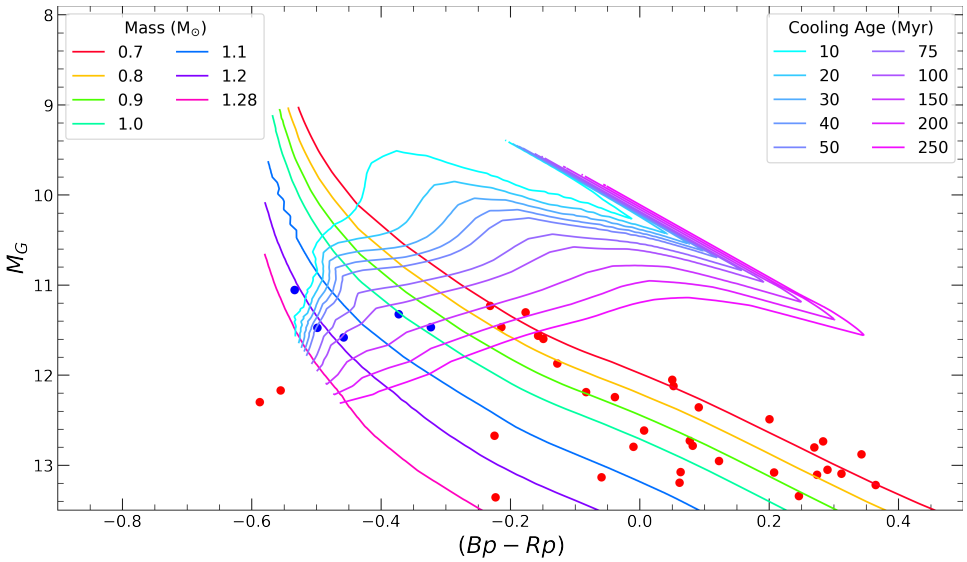

Figure 3.8: White dwarf cooling sequence with potential escapees from the Alpha Persei cluster identified in the Gentile Fusillo et al. [49] WD catalogue. Candidates selected for follow-up observations indicated in blue. Cooling tracks are as in Fig. 3.7.

3.2.2 Hyades

The last escapee search we will discuss is applying the H21a method to the heavily studied Hyades cluster. The Hyades cluster is approximately 680 Myrs old [52] and has a particularly low velocity dispersion of ~ 0.3 km s^{-1} [30]; the combination of these could lead to a substantial population of escapees. The Hyades cluster is particularly extended on the sky due to its close proximity to the Sun. As such, the cluster is difficult to identify in proper motion space and we cannot use the R21 method to determine cluster centre parameters.

Instead, for our catalogue, we take the Lodieu et al. [84] DR2 catalogue of high-confidence cluster members, which contains 710 candidate stars, and crossmatch it with Gaia EDR3. This returns a sample of 665 candidate members; we further reduce this via a 3σ cut in C^* for stars dimmer than $G = 4$, reducing the sample to 564 sources. Cluster centre parameters are determined from the mean values of this sample of high-confidence cluster members.

As with Alpha Persei, we search for escapees using two methods: one uses an extended volume of escapee candidates while the other uses the entire Gentile Fusillo et al. [49] WD catalogue. Because the cluster's displacement from the Sun is small, we consider every Gaia EDR3 source within 200 pc as a potential escapee for our extended volume. We relax the minimum cluster distance for candidacy to 30 pc, the relative reconstructed 3D velocity to 10 km s^{-1}, and the escape time to < 650 Myrs to allow for escapees early in the cluster's history. The Fusillo EDR3 WD catalogue search uses the same escapee candidate requirements. Otherwise, the methodology follows the same prescription as Alpha Persei.

To be considered a candidate escapee WD we require that the estimated cooling age is between 450 and 650 Myrs for $M > 1.1$ $M_\odot$. Younger WDs are not likely to be ultramassive due to the expected main sequence lifetimes for their progenitors (see Fig. 1.2), while older WDs are not likely to have originated in the cluster. Both search methods returned a single candidate ultramassive WD, with an estimated mass of > 1.3 $M_\odot$. Fig. 3.9 shows the results of the Lodieu et al. [84] crossmatch along with the extended volume escapers, with the ultramassive WD candidate shown in blue on the right graph. Fig. 3.10 displays the Fusillo catalogue search results, with the same ultramassive WD candidate again shown in blue. Tab. 3.3 presents parameters for candidate escapee WDs identified in the reconstructed velocity searches of Alpha Persei and the Hyades using the Fusillo catalogue.

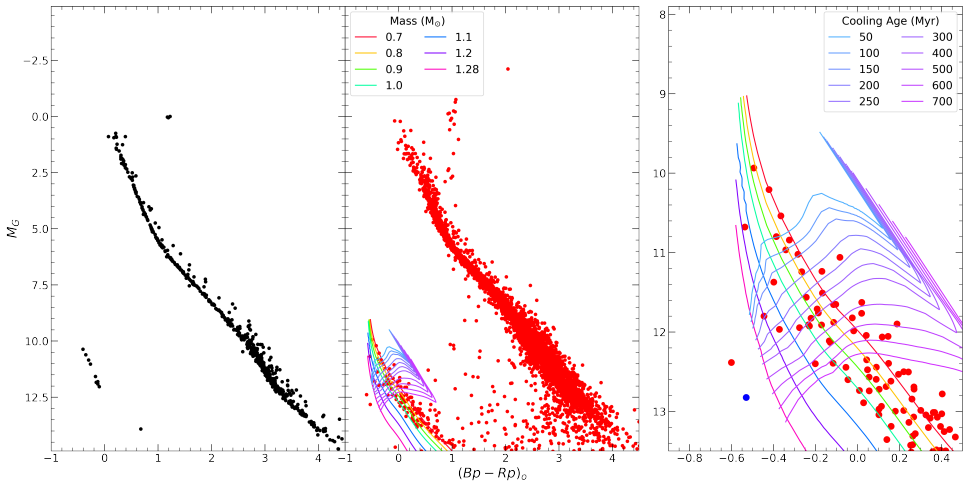

Figure 3.9: Gaia EDR3 CMDs for Hyades cluster. *Left*: Cluster members from Lodieu et al. [84] crossmatch. *Middle*: Escapee candidates from H21a method. Horizontal tracks are for cooling ages from 50 to 700 Myr (top to bottom), while vertical tracks display mass models from 0.7 to 1.28 $M_\odot$ (right to left). *Right*: Zoom in of the WD cooling sequence from the central graph, with selected candidate for follow-up observation in blue.

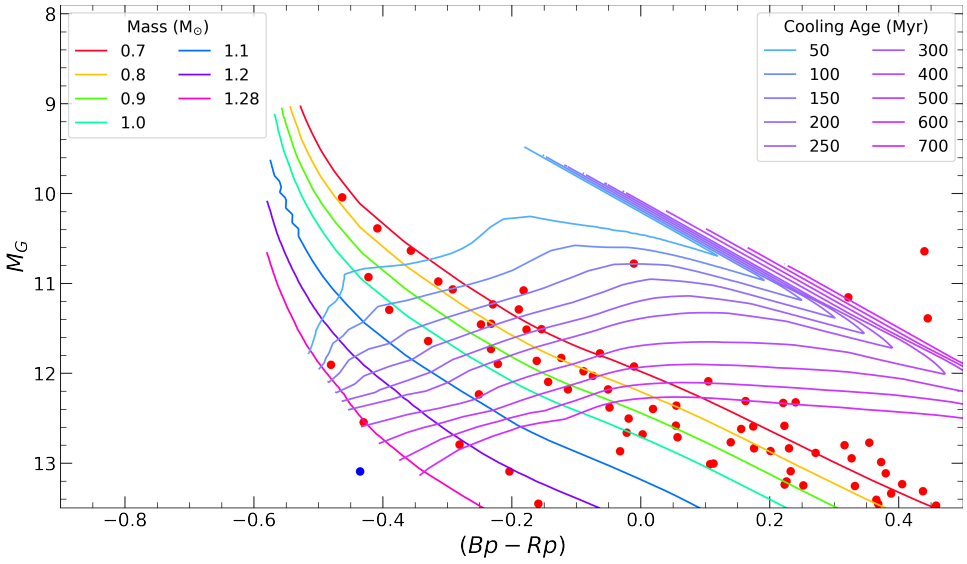

Figure 3.10: As in Fig. 3.8, but for the Hyades cluster. Cooling tracks are as in Fig. 3.9.

Table 3.3. Reconstructed Cluster Escapee Candidates

Identifier	Gaia DR2 Source ID	M_G [mag]	(Bp-Rp)$_o$	Mass [$M_\odot$]	Cooling Age [Myr]	$D_{current}$ [pc]	D_{min} [pc]	$\Delta\vec{v}_{3D}$ [km s^{-1}]	t_{escape} [Myr]
(1)	(2)	(3)	(4)	(5)	(6)	(7)	(8)	(9)	(10)
Alpha Persei WD1	439597809786357248	11.052	-0.534	1.22	0.86	24	8.98	4.08	5
Alpha Persei WD2	244003693457188608	11.578	-0.458	1.18	103.45	20	5.40	1.61	12
Alpha Persei WD3	1924074262608187648	11.321	-0.373	1.01	116.57	113	4.68	4.73	25
Alpha Persei WD4	1990559596140812544	11.467	-0.323	0.97	156.50	117	9.82	4.60	25
Alpha Persei WD5	1983126553936914816	11.472	-0.499	1.22	52.59	136	6.61	4.43	30
Hyades	560883558756079616	13.091	-0.435	>1.28	...	84	16.90	9.80	15

Notes. Select parameters for candidate ultramassive WDs identified in Fusillo catalogue using reconstructed velocity methods. Columns: (1) Identifier; (2) Gaia EDR3 source ID [47]; (3) absolute G magnitude dereddened using source reddening from Gentile Fusillo et al. [49]; (4) reddening corrected (Bp-Rp) colour; (5) mass estimate from cooling model fits; (6) cooling age estimate from same model fits; (7) Current distance from cluster centre; (8) Distance of closest cluster centre approach; (9) Reconstructed 3D velocity; (10) Time of closest approach.

Chapter 4

Observations

We obtained follow-up spectroscopic observations with the Gemini Observatory, which consists of twin observatories, Gemini North on Mauna Kea, Hawaii, and Gemini South on Cerro Pachon, Chile. Each telescope uses a Ritchey-Chretien Cassegrain telescope with an 8.1 m concave primary mirror and a 1 m convex secondary [51]. The 8.1 m primary mirrors make these telescopes the largest ground-based optical telescopes available to Canadian astronomers. The size of the mirrors and the near complete sky coverage provided by the pair make these prime for observing the faint WDs we identified in our various searches.

Using Gemini, we obtained candidate spectra using the Gemini Multi-object Spectrographs (GMOS), which operate between approximately 360 and 1030 nm. An array of three Hamamatsu CCDs provides a 5.5 arcmin field of view (FOV). The total size of the combined arrays is 2048 by 4176 (Gemini North) and 2048 by 4608 (Gemini South), giving effective pixel scales of 0.08 and 0.07 arcseconds per pixel, respectively. As a gap of 67 pixels separates the CCDs on the array, appropriate wavelength dithering is necessary for full coverage. Each observation used longslit mode with a 1.0 arcsec focal plane mask, with the B600 grating and no filter. Binning of 2x2 in both the spectral and spatial directions provides an effective pixel scale of ~ 0.15 arcsec per pixel for a resolution of ~ 1 $\AA$.

4.1 Data Reduction

The Gemini data were reduced with the Image Reduction and Analysis Facility (IRAF, [130]) system, particularly the python implementation of it PyRAF. We provide a low-level look at the data reduction process; for a detailed explanation of the steps and python implementation, see the GMOS Data Reduction Cookbook[1].

For the appropriate observing program, data is obtained from the Gemini Archive. Each program includes four primary types of exposures. Exposures taken of the target object are referred to as science exposures. Arc lamp exposures produce a predictable emission spectrum, and are used to calibrate wavelengths. Observations of a photometric standard of known flux are used to calibrate the science exposure flux. Finally, uniformly lit images that reveal variations on the CCD are called flats. In addition to program exposures, we also need baseline calibrations for the instrument. These are known as bias frames, short exposures taken with no light on the CCD that returns noise from the CCD added during readout.

The next step is to create an observing log database of all the different exposures. The subsequent steps refer to this database to determine which exposures to use. After completing the observation log, the first reduction step is to perform an overscan correction, which subtracts out variations caused by pixels in the overscan region of the CCD. The overscan correction is applied to all exposures. After this, all of the bias exposures in a predefined time range are combined into a bias residual MasterCal file. The bias residual is applied to the science, arc, standard, and flat field exposures. Each file is converted to brightness units by dividing out the sensor gain.

The three CCD chips are designed to favour different wavelengths, so the normalization differs between them. We correct for this quantum efficiency difference in the flat field, standard, and science exposures. The images from different CCDs are then mosaiced into single images. For these same exposures, we identify and reject cosmic rays. The flat exposures are combined into a flat-field MasterCal, which is applied to each science and standard file to correct for flat field distortions.

The arc exposures are mosaiced and used to determine the wavelength calibra-

[1] https://noirlab.edu/science/programs/csdc/usngo/gmos-cookbook/index.html

tion. In this step, an automated process selects spectral lines of the arc file and compares them to input wavelengths for calibration. If the automated process fails, this step can be performed interactively, with the spectral lines manually selected. The wavelength calibration is used to derive a dispersion solution, which is applied to calibrate the standard. A region along the slit with no discernible emission is selected to subtract the sky for the standard. The standard spectrum is then ready for extraction. The extraction process is automatic as long as the target is the brightest source in the slit, which is generally the case for the standard. Once the standard spectrum is extracted, the flux is used to derive its flux calibration.

Separate arc exposures for the science exposures determine an additional wavelength calibration and dispersion solution. The sky is subtracted in the same fashion as for the standard. The spectra are extracted, though, unlike with the standard, the science target is often not the brightest object in the slit. In this case, the target spectrum has to be selected manually. Finally, the flux calibration from the standard is applied to the science exposures. Once the science flux is calibrated, the final step combines every science file into a single spectrum. The exposures are taken at two separate wavelengths due to the CCD chip gaps, typically separated by 5 to 10 nm. Before combining the exposures, the wavelengths have to be aligned. Once the science exposures are aligned and combined, the data reduction process is complete.

4.2 Observation Details

We observed ten candidate ultramassive WDs with Gemini, including nine of the escapees selected in Ch. 3. The tenth object we observed with Gemini is the candidate identified in the EDR3 search of the vdB Hagen 99 cluster. We previously showed the CMD of this cluster in Fig. 2.2b. Unlike the other selected candidates, this source is within 2σ of the cluster centre in both proper motion and parallax space and is, as such, considered a potential current cluster member. Fig. 4.1 shows the WD cooling sequence for vdB Hagen 99, giving a mass of > 1.28 $M_{\odot}$, and thus no cooling age estimate. While this object appears to be far to the left of the WD cooling sequence, the colour error bars are significant, and we do not rule out potential membership based on that alone.

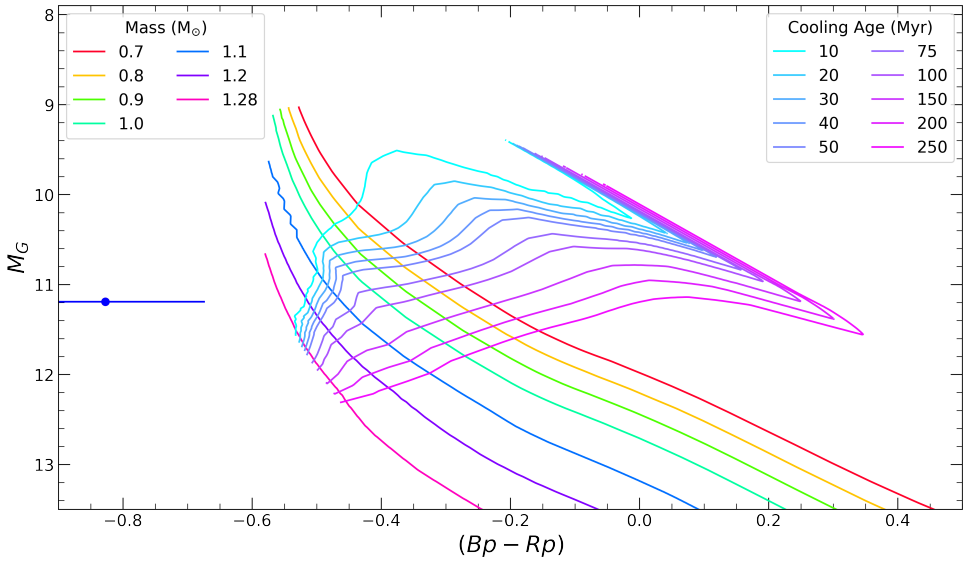

Figure 4.1: WD cooling sequence of the vdB Hagen cluster, whose Gaia EDR3 CMD shown in Fig. 2.2b. Candidate WD is to the left of the cooling sequence, along with 1σ error bars. Cooling sequences are as in Fig. 3.8.

My colleague Ilaria Caiazzo observed the three remaining escapee candidates selected in Ch. 3. Alpha Persei WD3 and 4 were observed with the Hale telescope at Palomar Observatory. Spectra were taken with the Double-Beam Spectrograph (DBSP, [97]) using the R600 and R316 gratings on the blue and red arms, respectively, with total exposure times of 20 minutes each. WD5 was observed with the Keck Telescope using the Low Resolution Imaging Spectrometer (LRIS, [98]) using the R600 grim for both arms for a total exposure time of 10 minutes.

The ten candidates were observed over 11 months as part of four separate Gemini observation programs; these programs are detailed in Tab. 4.1. We show the reduced spectra for these ten candidates in Figs. 4.2 through 4.5, with the reduction following the steps presented in Sec. 4.1. In Ch. 5 we analyze each of these reduced spectra and discuss the results and implications for the WD IFMR.

Each spectrum shows a particularly blue continuum with broad Balmer lines. From this, we confirm each of the ten are H-atmosphere DA WDs. None display clear Zeeman splitting of the Balmer lines, so we rule out the possibility of strong

Table 4.1. Observation Details

Name	Gaia	Ra	Dec	Parallax	Telescope	Gemini Program Details			
						Program ID	Exposures	Total Time	Observation Dates
		[deg]	[deg]	[mas yr^{-1}]			[s]	[m]	
(1)	(2)	(3)	(4)	(5)	(6)	(7)	(8)	(9)	(10)
Alessi 21 WD1	DR2	109.4177	-12.0308	1.17	Gemini South	GS-2021A-Q-236	10x1040	173	19/01/2021
Alessi 21 WD2	DR2	104.6703	-8.2879	1.49	Gemini South	GS-2021A-Q-236	8x1025	137	07/02/2021
NGC 2422	DR2	113.3759	-15.7805	3.93	Gemini South	GS-2021A-Q-236	8x1025	137	07/02/2021-08/02/2021
NGC 2451B WD1	DR2	120.9797	-40.2599	1.32	Gemini South	GS-2021A-Q-236	8x400	53	21/01/2021
NGC 2451B WD2	DR2	112.6808	-33.6684	2.20	Gemini South	GS-2021A-Q-236	8x625	83	06/02/2021
NGC 2516	DR2	117.2778	-59.7985	2.40	Gemini South	GS-2021A-Q-236	8x400	53	08/02/2021
Alpha Per WD1	EDR3	4.6805	50.3478	6.44	Gemini North	GN-2021B-FT-103	4x685	46	10/08/2021-12/08/2021
Alpha Per WD2	EDR3	59.2417	45.0198	5.93	Gemini North	GN-2021B-FT-103	4x900	60	06/10/2021
Alpha Per WD3	EDR3	354.1364	42.7338	6.60	Hale	-	-	-	-
Alpha Per WD4	EDR3	344.6288	53.7945	6.31	Hale	-	-	-	-
Alpha Per WD5	EDR3	337.0616	45.5762	6.64	Keck	-	-	-	-
Hyades	EDR3	39.6517	76.7052	5.98	Gemini North	GN-2021B-FT-216	8x1000	133	01/03/2021-02/03/2021
vdB Hagen 99	EDR3	159.6909	-58.8402	2.20	Gemini South	GS-2022A-FT-104	16x895	239	08/04/2022-29/04/2022

Notes. Select details for follow-up observations of candidates selected in Ch. 3. (1) WD identifier from this work; (2) Gaia release; (3-5) Ra, dec, and parallax for WD in said Gaia catalogue; (6) Telescope used for follow-up observations; (7-11) Program details if observed with Gemini.

magnitude fields. Note that though our observations covered the wavelength range of Hα, the signal-to-noise ratio (SNR) was rarely high enough to give a useful spectral line. The surface gravity and temperature fits are largely driven by the next few Balmer lines and are not heavily impacted by Hα. Hα is particularly important for characterizing the strength of a detected magnetic field, but since none of the observed WDs displayed Zeeman splitting, the absence of Hα is not expected to influence results negatively.

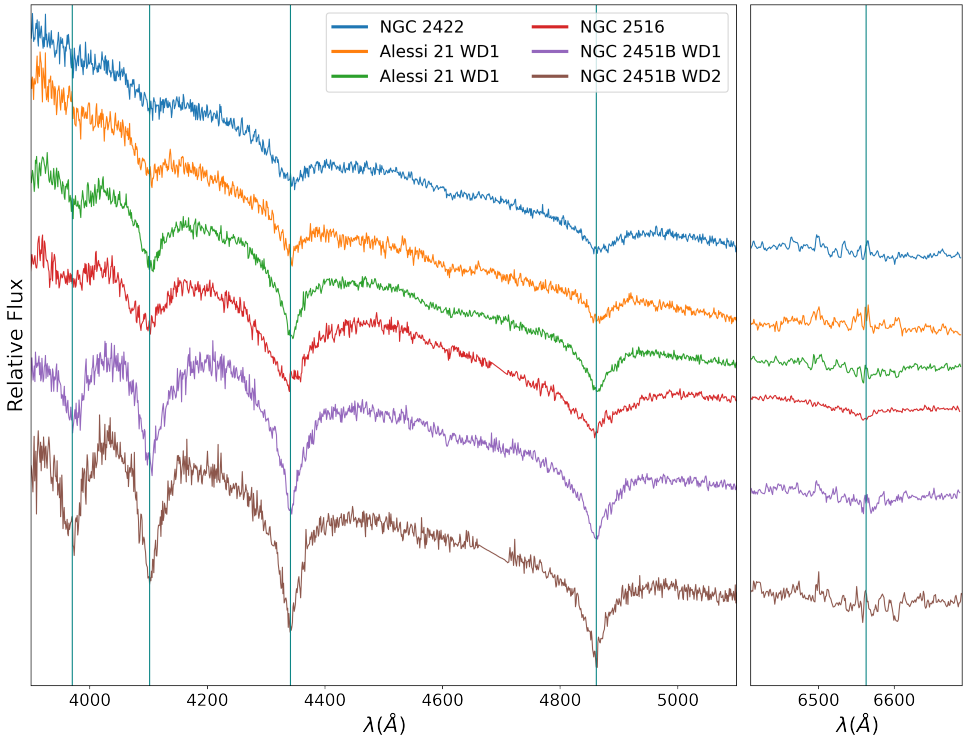

Figure 4.2: Reduced spectra for WDs identified in the wide search. We normalize the flux at 4400 $\AA$. The different spectra are shifted vertically arbitrarily for comparison. The central wavelength of the Balmer lines Hβ through Hε are indicated with blue vertical lines on the left panel, while the right panel shows the same for Hα.

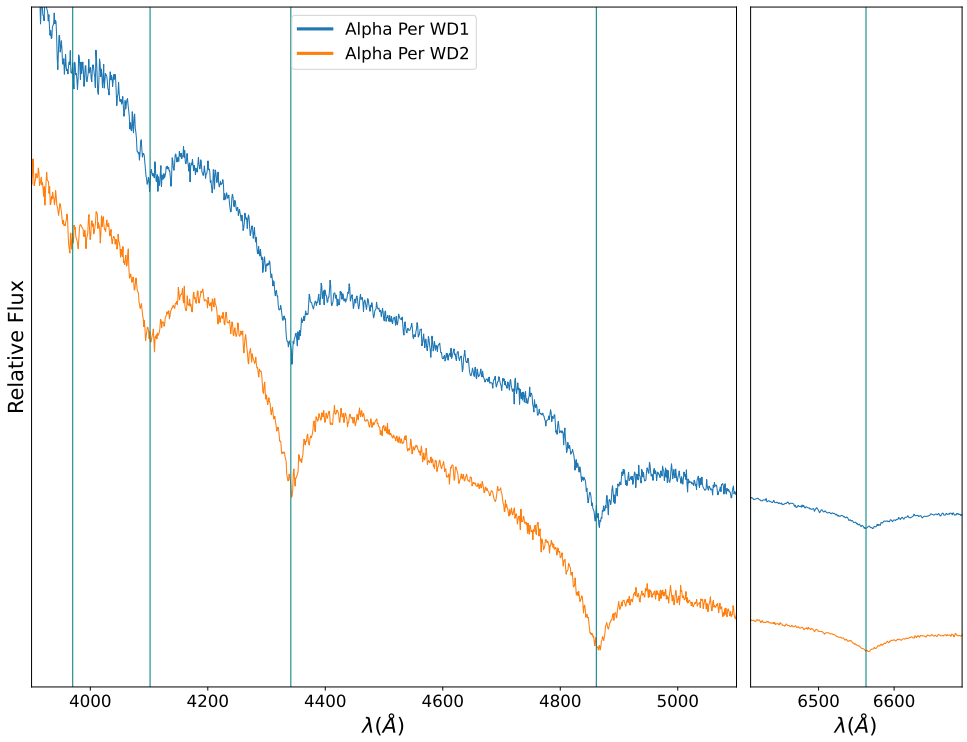

Figure 4.3: As in Fig. 4.2, but for Alpha Persei escapee candidates.

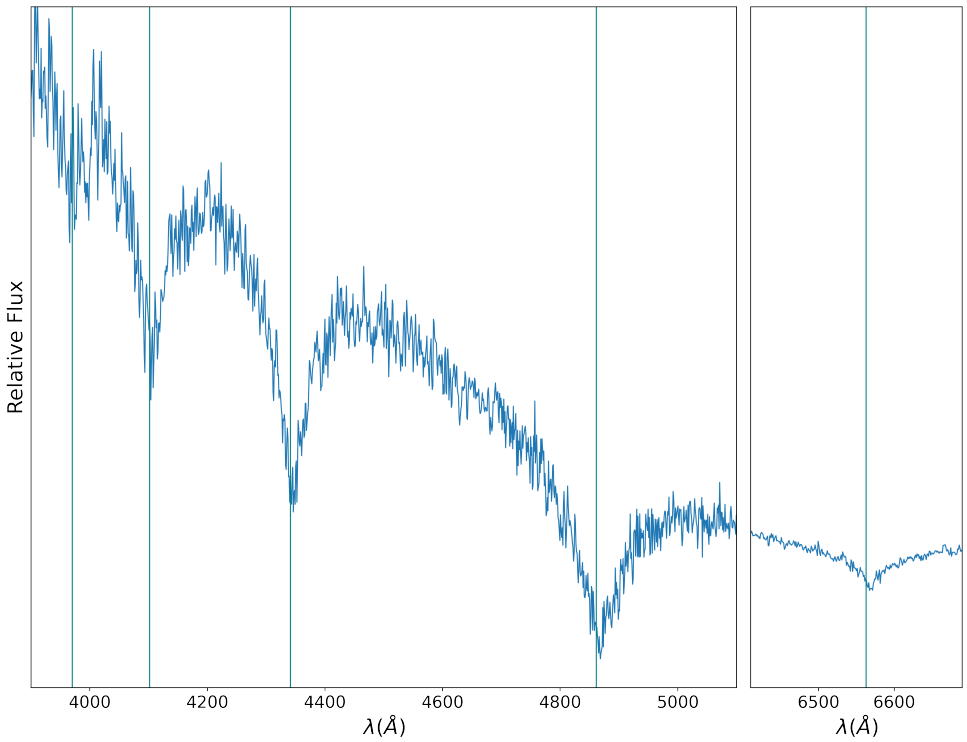

Figure 4.4: As in Fig. 4.2, but for Hyades escapee candidate.

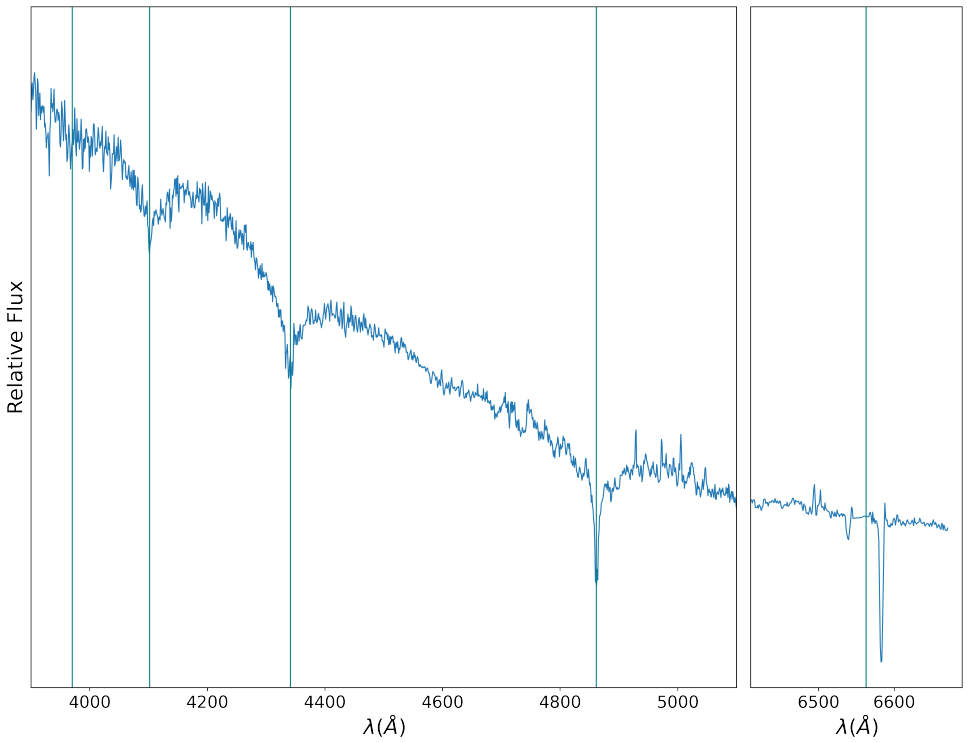

Figure 4.5: As in Fig. 4.2, but for vdB Hagen 99 cluster member candidate.

Chapter 5

Results and Discussion

We now analyze the spectra reduced in Ch. 4. We simultaneously fit the Balmer lines for each spectrum using the technique outlined in Sec. 2.2. From the best fit values of log g and $T_{\rm eff}$, we estimate the cooling age and mass of the WD, as in Sec. 2.3. In each case, we determine the error in the fit parameters from the covariance matrix. We estimate parameters for a CO core for all candidates, and ONe core masses for WDs with a CO core mass of > 1.1 $M_{\odot}$. Progenitor masses are estimated as in Sec. 2.4.

We do not present results in cases where the progenitor lifetime gave a progenitor mass that strongly diverges from the current understanding of the IFMR. In most cases, these candidates are concluded to be non-members. The full spectroscopic and derived quantities for each candidate are presented in Tab. 5.1. In this table, we also included parameters for Alpha Persei WDs 3 through 5, as determined by Ilaria Caiazzo and presented in Miller et al. [88]. We examine the observed WDs in detail in this chapter.

Age determinations for each relevant cluster found from PARSEC isochrones. We use the Gaia EDR3 photometric system with the Kroupa [77] IMF, no extinction, and cluster metallicity. When available we use metallicity estimates from [93], determined from both photometric and spectroscopic data. In some cases, they give multiple metallicity estimates from different methods, in which case we take the variance weighted mean. Although the wide search used Gaia DR2 data, with cluster CMDs determined by R21, age estimates use updated EDR3 cluster

Table 5.1. Spectroscopic and Derived Quantities For All Candidates

Name	$T_{\rm eff}$	log g	ONe Core			CO Core			Membership
			$M_{\rm f}$	$t_{\rm cool}$	$M_{\rm i}$	$M_{\rm f}$	$t_{\rm cool}$	$M_{\rm i}$	
	[10^3 K]	[cm s^{-2}]	[$M_\odot$]	[Myr]	[$M_\odot$]	[$M_\odot$]	[Myr]	[$M_\odot$]	
(1)	(2)	(3)	(4)	(5)	(6)	(7)	(8)	(9)	(10)
Alessi 21 WD1	60.4 ± 1.1	8.14 ± 0.05	—	—	—	0.78 ± 0.03	1 ± 1	—	Non-member
Alessi 21 WD2	35.1 ± 0.2	8.60 ± 0.02	—	—	—	1.01 ± 0.01	28 ± 2	8^{+3}_{-1}	Unlikely member
NGC 2422	51.3 ± 0.7	9.13 ± 0.10	1.23 ± 0.03	15 ± 11	$5.8^{+0.9}_{-0.6}$	1.26 ± 0.03	33 ± 11	$7.8^{+0.9}_{-2}$	Questionable member
NGC 2451B WD1	27.0 ± 0.2	8.38 ± 0.02	—	—	—	0.87 ± 0.01	49 ± 2	—	Non-member
NGC 2451B WD2	25.2 ± 0.2	8.06 ± 0.03	—	—	—	0.67 ± 0.02	23 ± 1	—	Non-member
NGC 2516	31.0 ± 0.2	9.08 ± 0.06	1.21 ± 0.02	170 ± 20	10^{x}_{-4}	1.24 ± 0.02	176 ± 10	12^{y}_{-6}	Questionable member
Alpha Per WD1	41.6 ± 0.2	9.05 ± 0.03	1.20 ± 0.01	45 ± 4	8.5 ± 0.9	1.23 ± 0.01	62 ± 4	12^{+4}_{-2}	High-confidence Member
Alpha Per WD2	46.2 ± 0.3	8.98 ± 0.04	1.17 ± 0.01	14 ± 4	6.3 ± 0.3	1.20 ± 0.02	31 ± 4	7.2 ± 0.6	High-confidence Member
Alpha Per WD3	23.9 ± 1.0	8.56 ± 0.10	—	—	—	0.97 ± 0.06	133 ± 11	—	Non-member
Alpha Per WD4	21.2 ± 1.0	8.56 ± 0.10	—	—	—	0.98 ± 0.06	201 ± 11	—	Non-member
Alpha Per WD5	47.5 ± 0.5	8.84 ± 0.05	1.12 ± 0.02	3 ± 1	5.9 ± 0.2	1.14 ± 0.02	12 ± 4	6.2 ± 0.3	High-confidence Member
Hyades	$< 30{,}000$	> 9.25	—	—	—	—	—	—	Questionable member
VdB Hagen 99	58.4 ± 1.0	8.64 ± 0.04	—	—	—	1.05 ± 0.02	1 ± 1	$6.2^{+0.2}_{-0.8}$	Questionable member

Notes. Spectroscopic and derived quantities for WDs examined in this work. Columns: (1) WD identifier from this work; (2-3) Estimated temperature and surface gravity from Balmer line fits; (4-5) Mass and cooling age estimates for ONe core, only included for WDs whose mass estimate is > 1.1 $M_\odot$; (6) Progenitor mass estimates from these ONe model results, only included for cases where the cluster age combined with the WD age gives a reasonable result; (7-9) As in (4-6) but now for CO core, model results given for all WDs; (10) cluster membership expectation, see this chapters individual discussion sections for details.

CMDs developed for this work using the methodology detailed in Sec. 2.1. Gaia EDR3 is based on 34 months of data [47] vs 22 months for Gaia DR2 [46], so the EDR3 CMDs are expected to have more accurate colours and, thus, better age determinations. Though we will consider the full CMD when trying to find the best fit isochrones, we emphasize that we favour the MSTO, where the stars are particularly sensitive to cluster age [52]. To estimate the uncertainty in the best fit isochrone we visually examine the range of isochrones that provide a quality fit to the data. The error is taken as half the difference between the oldest and youngest isochrone that reasonably describes the data. We note that while this method allows us to reasonably estimate cluster age's, the visual comparison method at times leads to significant uncertainty in the cluster age. To combat this we also source cluster age estimates from the literature, depending on the confidence level of the isochrone fit.

5.1 Alessi 21

We estimate the age of the cluster using solar metallicity [11] PARSEC isochrones for ages from 50 to 80 Myrs, shown in Fig. 5.2. The MSTO is sparsely populated, and with no giant stars present, the cluster age determination is based on a minimal sample of stars. From the brightest blue MSTO star, we estimate an age of 65 ± 10 Myrs. This estimation is consistent with the work by Bossini et al. [11], which estimated 63 ± 3 Myrs from a Bayesian automated isochrone fitting technique.

The Balmer line fits are shown in Fig. 5.1. For WD1 we find an effective temperature of $60,400 \pm 1,100$ K with log g of 8.14 ± 0.05 cm s^{-2}, which suggests a cooling age of just 1 ± 1 Myr and a mass of 0.78 ± 0.03 M$_\odot$. This WD is the youngest, hottest WD of any we sampled. Given its young age and rather low mass, its progenitor lifetime would vastly exceed the cluster's age, and as such, we eliminate the possibility of cluster membership. WD2 turns out to be quite a bit more massive, with a CO core mass estimate of 1.01 ± 0.01 and cooling age of 28 ± 2 Myrs determined from an effective temperature of $35,100 \pm 200$ K and log g of 8.60 ± 0.02 cm s^{-2}. From this, we find a progenitor mass of 8^{+3}_{-1} M$_\odot$, which would place the object as quite an outlier in the IFMR and suggest a maximum WD progenitor mass above even the most aggressive of estimates [78], as such, we conclude this is also not a cluster member.

5.2 NGC 2422

Fig. 5.1 shows the best fit to the Balmer lines, giving best fit values of $T_{\rm eff} = 51,300 \pm 700$ K and log g $= 9.13 \pm 0.10$ cm s^{-2}. Due to the high effective temperature, simultaneously fitting of the Balmer lines required using metal polluted models from Gianninas et al. [50]. Given the high surface gravity, we consider both CO and ONe core cooling models. CO core models give a WD mass of 1.26 ± 0.03 M$_\odot$ with a cooling age of 33 ± 11 Myr, while ONe models give 1.23 ± 0.03 M$_\odot$ and 15 ± 11 Myr, respectively.

To determine the cluster age we use PARSEC isochrones for ages from 90 to 150 Myrs using the cluster's metallicity estimate of [Fe/H] $= +0.09$ from Netopil et al. [93]. From Fig. 5.3, we see the isochrones describe the majority of the main sequence well. The upper main sequence is troublesome, however, as the spread

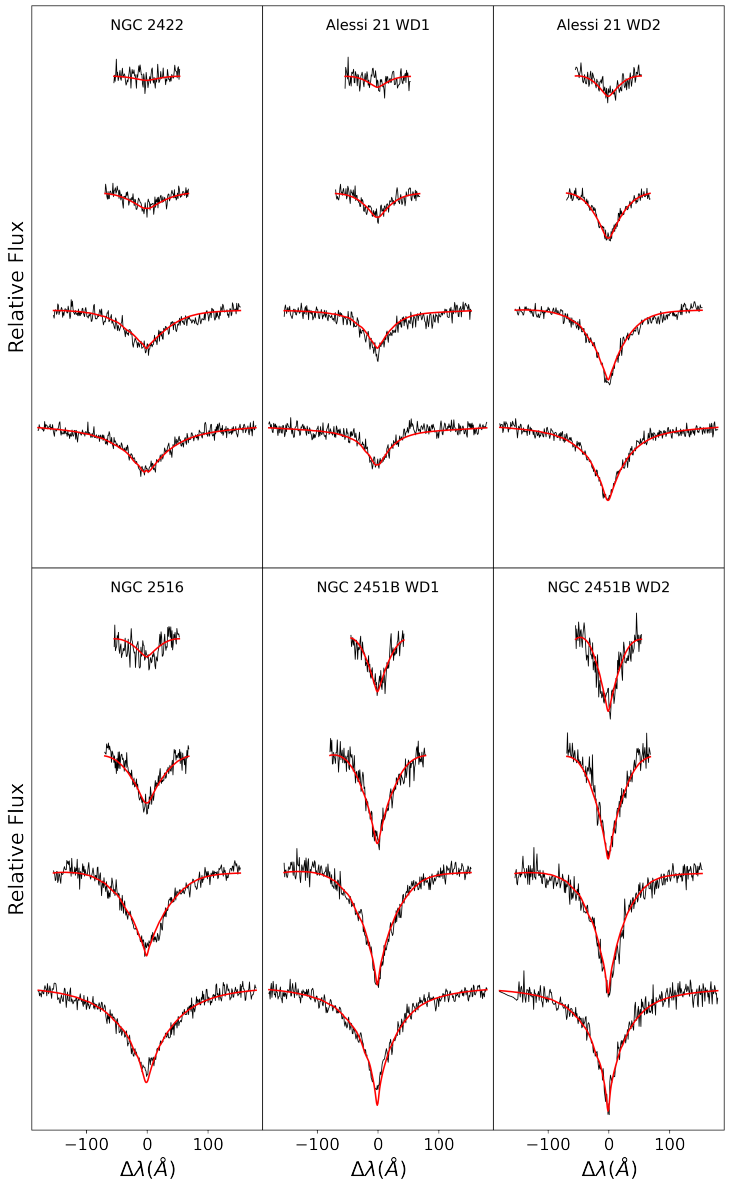

Figure 5.1: Balmer line fits of Hβ through Hε for the wide search WD spectra shown in Fig. 4.2. Hα is not included due to insufficient SNR. Alessi 21 WD1 and NGC 2422 fit with Gianninas et al. [50] metal polluted H-dominated atmosphere models, while the remainder use pure H models from Tremblay et al. [132].

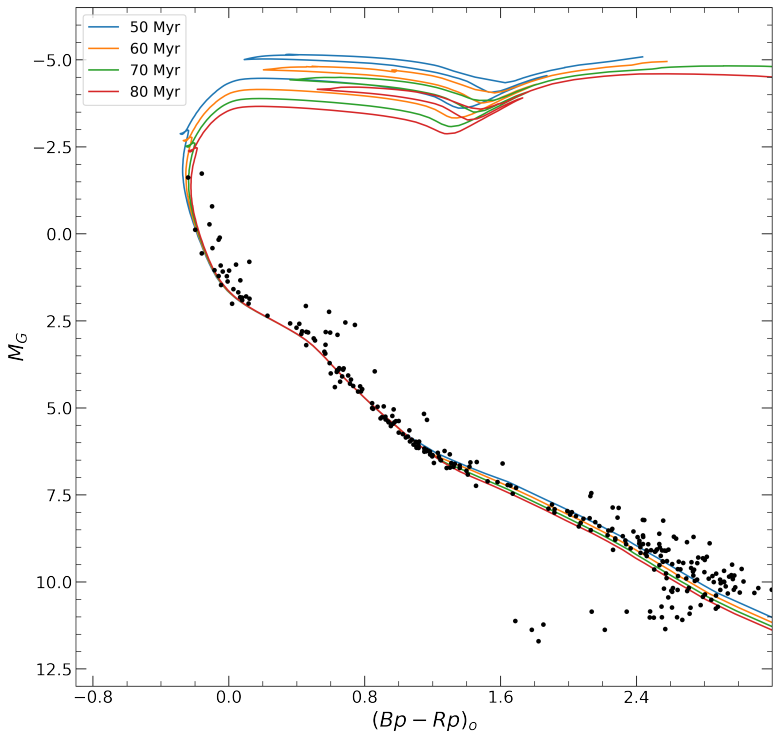

Figure 5.2: Alessi 21 EDR3 CMD, with PARSEC [13] isochrones computed with the Kroupa [77] IMF and no extinction, at solar metallicity. Ages as indicated on the diagram.

of colours prevents any single isochrone from completely describing the data. The lower main sequence prefers the younger isochrones. Overall we find the 110 and 150 Myr isochrones each match the data comparably well. From these, we estimate an age of 130 ± 20 Myrs. Age estimates from the literature vary wildly, Cummings and Kalirai [27] estimated an age of 155 ± 20 Myrs [27] from Gaia DR2 isochrones, while Loktin and Popova [85] estimate its age as just 72 ± 11 Myrs from 2MASS data.

The ages suggested by our isochrones and Cummings and Kalirai [27] give progenitor masses far too low for sensible placement on the IFMR. On the other hand, if we assume the 2MASS ages of Loktin and Popova [85] this would lead to a progenitor mass of $5.8^{+0.9}_{-0.6}$ $M_\odot$ for a ONe core, or $7.8^{+0.9}_{-2}$ $M_\odot$ for a CO core. For this WD to make sense as an escaped former cluster member, the cluster's age must

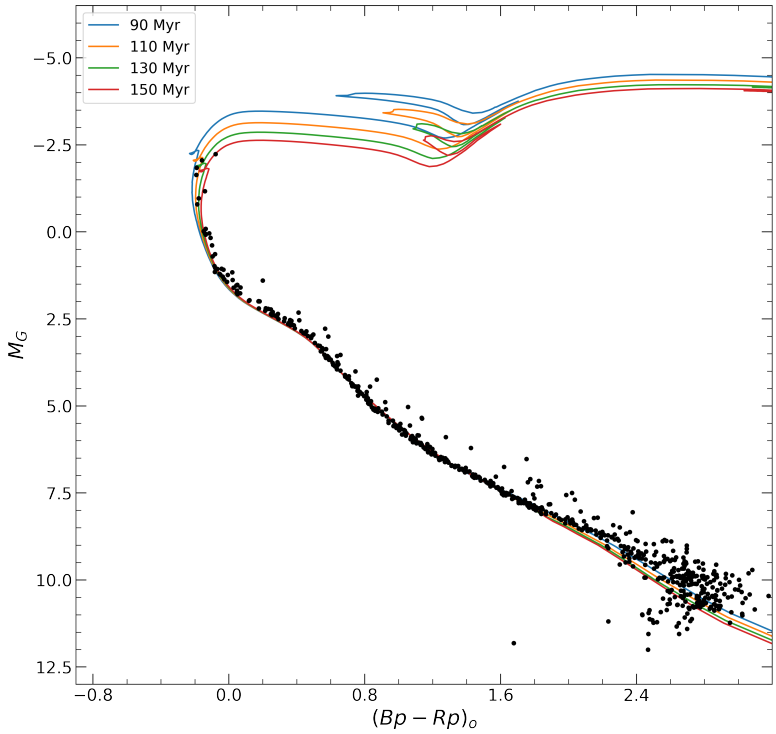

Figure 5.3: As in Fig. 5.2, but for NGC 2422 computed with metallicity of $[\mathrm{Fe/H}] = +0.09$.

be much lower than our isochrone fits suggest. We include the progenitor mass results using the Loktin and Popova [85] age estimate in Tab. 5.1, but emphasize that we are not confident in this determination. If the cluster is indeed such a young, this white dwarf would be the most massive known cluster member WD.

5.3 NGC 2451B

The best fit to the Balmer lines in Fig. 5.1 give $T_{\mathrm{eff}} = 27,00 \pm 200$ (WD1) and $25,200 \pm 200$ K (WD2), and log g of 8.38 ± 0.02 (WD1) and 8.06 ± 0.03 (WD2) cm s^{-2}. CO core WDs satisfactorily model these with masses of 0.87 ± 0.01 (WD1) and 0.67 ± 0.02 $\mathrm{M}_{\odot}$ (WD2) for ages of 49 ± 2 (WD1) and 23 ± 1 Myrs (WD2), respectively. The masses are significantly lower than the lower 1σ estimate from Gaia DR2 photometry given in Tab. 3.2, suggesting neither are likely associated

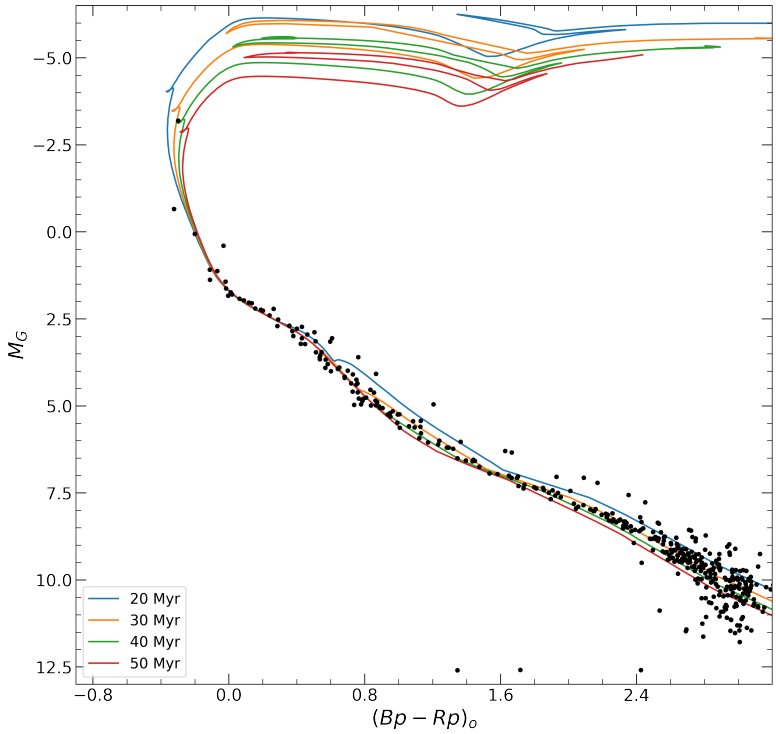

Figure 5.4: As in Fig. 5.2, but for NGC 2451B.

with the cluster at all.

PARSEC isochrones are computed using solar metallicity [93] for ages 20 to 50 Myrs. They are shown with the DR2 cluster CMD in Fig. 5.4. The 30 and 40 Myr isochrones are acceptable fits to the brightest cluster star, while the lower main sequence prefers the 50 Myr isochrone. From these, we estimate the cluster age as 40 ± 10 Myr. The cooling age of WD1 of 49 ± 2 Myr rules out cluster membership, as this age is close to the upper bound age of the cluster. For WD2, an estimated CO mass of just 0.67 ± 0.02 suggests a progenitor lifetime that vastly exceeds the cluster's age. We confirm our original expectation from the cooling models alone that neither of these WDs is associated with the NGC 2451B cluster.

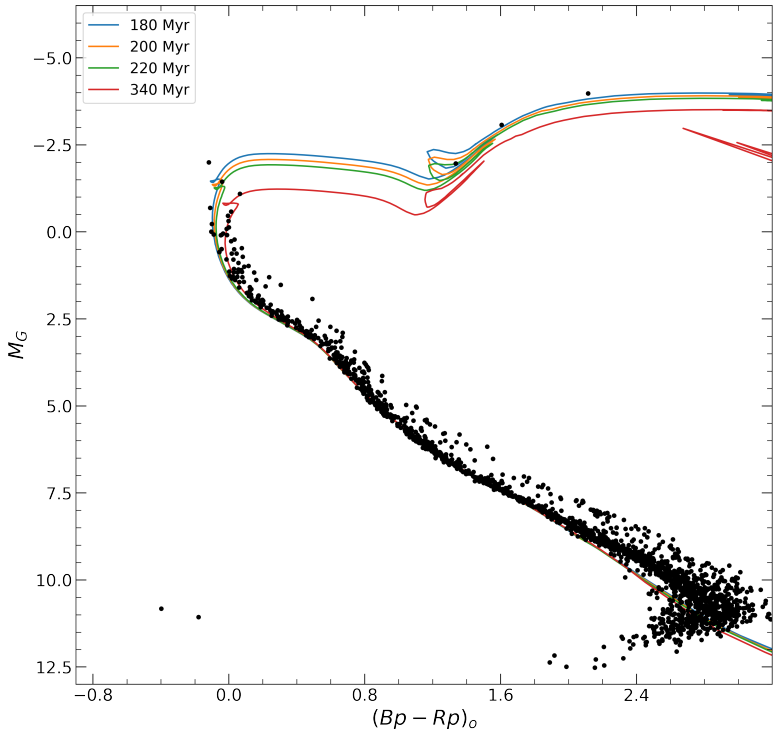

Figure 5.5: As in Fig. 5.2, but for NGC 2516 computed with metallicity of $[\mathrm{Fe/H}] = +0.05$. An additional extinction of $\mathrm{Ag} = 0.1$ has been added when computing the PARSEC isochrones.

5.4 NGC 2516

A confident age determination for NGC 2516 is troublesome. Initially, we used PARSEC isochrones for $[\mathrm{Fe/H}] = +0.05$ [93] with no extinction, but found that the isochrones missed most of the main sequence, suggesting that the reddening was underestimated in R21. In Fig. 5.5 we have added an extinction of $\mathrm{A}_G = 0.1$ to the isochrones for ages from 180 to 220 Myr, as well as a much older 340 Myr isochrone. The added extinction significantly improves the fit to the MS. The giant stars prefer ages around 180 Myrs, while the upper main sequence has two different sets of stars; the stars with bluer $(\mathrm{Bp\text{-}Rp})_\mathrm{o}$ which prefer the 220 Myr fit, and a redder group of stars that are better fit by the 340 Myr one. The giant stars are a very poor fit for the 340 Myr isochrone. Generally, none of the isochrones are

quality fits to the lower MS, which prefers a much younger age. Age estimates that better fit the lower MS are very poor fits to the upper MS and giants, so we prefer the older age characterizations.

Bouma et al. [12] examined an expansive region around NGC 2516 and found an approximately 500 pc halo of stars of the same age as the cluster core. From this, they estimate an age range for the cluster from 100 to 200 Myr from lithium depletion and separately 150 to 200 Myr from gyrochronology. They expect that the width of the MSTO is a result of binaries, which make some of the stars appear redder than they are. For this reason, they favour isochrone fits to the bluer MSTO stars that also better fit the giant stars. Doing the same with our isochrones, we estimate the best fit as 190 ± 30 Myrs, where the significant error bars demonstrate the overall lack of confidence in the estimate.

The Balmer line fit to this WD candidate gives $\log g = 9.08 \pm 0.06$ cm s^{-2} and $T_{\rm eff} = 31,000 \pm 200$ K. The particularly high surface gravity warrants examination with both CO and ONe cores. ONe core best fit is for a mass of 1.21 ± 0.02 $M_\odot$ with a cooling age of 170 ± 20 Myr, combined with the cluster age, gives a progenitor lifetime of 20 ± 36 Myr. We find a progenitor mass of 10^{+x}_{-4} $M_\odot$, where no upper bound was calculated because this required the WD to be older than the cluster, precluding membership. For a CO core, we find a cooling age of 176 ± 10 Myr and mass of 1.24 ± 0.02 $M_\odot$, giving a progenitor mass of 12^{+y}_{-6} $M_\odot$, where once again no upper bound is determined. From the Balmer line fit in Fig. 5.1 we see that the core of Hγ is stretched at higher wavelengths, in particular ≈ 4345 to 4360 $\AA$ is at a greater depth than would be expected.

We examined the Gemini science exposures individually and found that the extra wide core was present in each of the eight individual exposures. This suggests that it is not likely an observation artifact but a real feature. We considered the possibility of an interstellar line or nearby helium line, but nothing we examined matched the particular wavelength range of the widened core. We cannot at this moment determine definitively the cause of this feature.

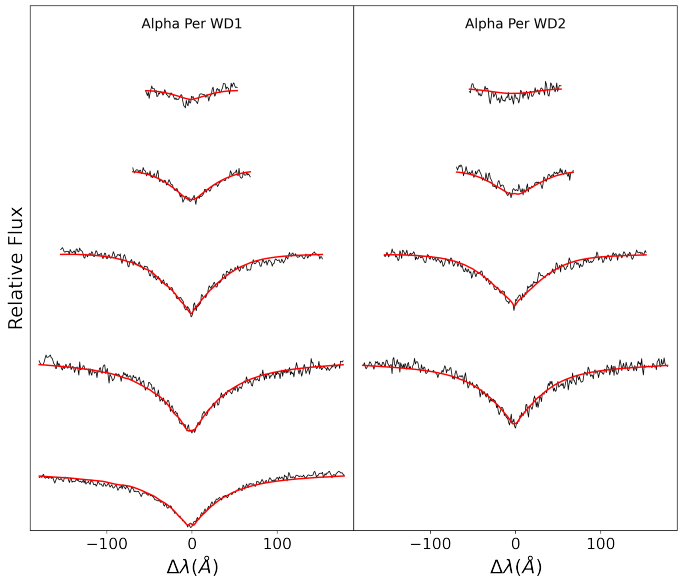

Figure 5.6: As in Fig. 5.1, but for Alpha Persei WDs 1 and 2. WD1 uses pure H models while WD2 uses metal polluted ones.

5.5 Alpha Per

WDs 1 and 2 appear to be very hot. As such, we consider both pure hydrogen and metal polluted atmosphere models. We find that the fit to WD1 is not improved using the polluted models and that it does not experience the Balmer line problem. We fit with pure hydrogen models and found a best-fit of $T_{\rm eff} = 41,600 \pm 200$ K with log g$= 9.05 \pm 0.03$ cm s^{-2}, the particularly low error in log g compared with other ultramassive WDs found in this work is a result of the improved signal-to-noise ratio (SNR) of these observations. From these atmospheric parameters, we find $M = 1.20 \pm 0.01$ M$_\odot$ with a cooling age of 45 ± 4 Myrs for a ONe core, and $M = 1.23 \pm 0.01$ M$_\odot$ with a cooling age of 62 ± 4 Myrs for CO core. WD2 does experience the Balmer line problem, and as a result, the fit quality improves using Gianninas et al. [50] metal polluted models, which give best-fit values of $T_{\rm eff} = 46,200 \pm 300$ K and log g $= 8.98 \pm 0.04$ cm s^{-2}. From these, we find ONe core $M = 1.17 \pm 0.01$ M$_\odot$ with a cooling age of 14 ± 4 Myrs, and CO fits of $M = 1.20 \pm 0.02$ M$_\odot$ with a cooling age of 31 ± 4 Myrs.

To determine the cluster age we first consider PARSEC isochrones at the ex-

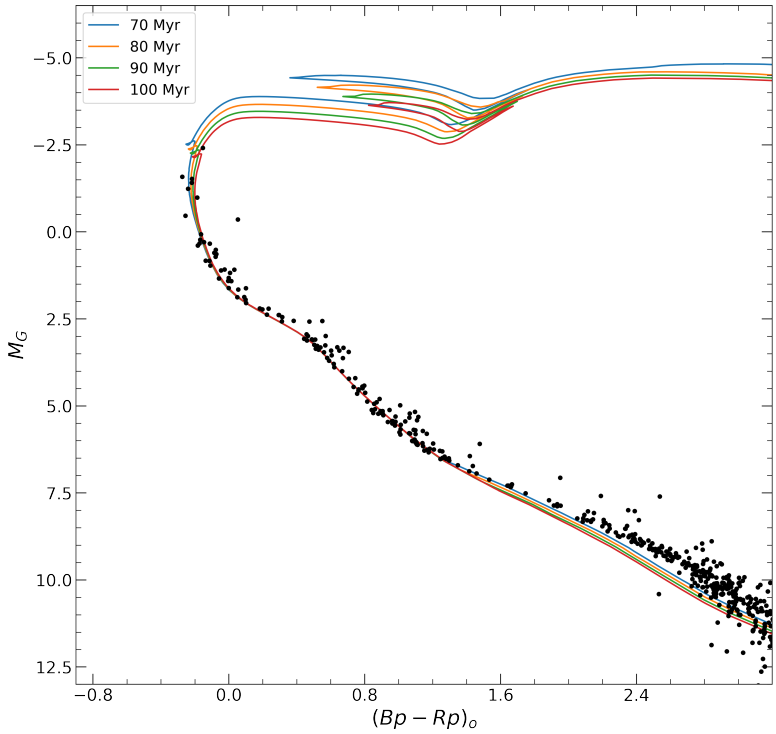

Figure 5.7: As in Fig. 5.2, but for Alpha Persei.

pected solar metallicity of Alpha Persei (see [27], [92]), which we display in Fig. 5.7 for ages between 70 and 100 Myrs. We find that the 70 Myr isochrone best fits the lower main sequence, but MSTO stars prefer the 80 and 90 Myr isochrones. From these, we estimate a cluster age of 80 ± 10 Myrs.

H21b derived the age of Alpha Persei from kinematics by examining how the CMD of escapee candidates changes with the cluster's age. Low mass stars spend significantly longer in pre-MS stages than their higher mass counterparts. During the pre-MS phase, stellar luminosity is notably lower than on the MS, even for stars with similar colours. As a result, cluster member stars that reach the main sequence will be significantly more luminous than their pre-MS counterparts. As such, the lower MS can be potentially used to constrain the cluster's age. They fit the lower MS using two different methods with a quartic polynomial. One is a χ^2 minimizer while the other is a more robust estimator R^2 (see Heyl et al. [55] Eqs. (11)

through (13) for details). They estimate the cluster's age by determining χ^2 and R^2 as a function of maximum escape time by examining how the CMD changes going farther into the past. They find that both estimators suddenly increase substantially at a given point, which they use to estimate the cluster's age. They estimate the uncertainty in this age determination by performing 100 resamplings of the escapees and then measuring the kinematic ages. From this technique, they estimate an age of 81 ± 6 Myrs.

The age estimate we obtain with isochrones agrees within the uncertainty of the kinematic estimate from H21b, though with increased error. Given the robust nature of the H21b method, we use their age determination to estimate the progenitor mass of the Alpha Persei WDs. For WD1, we find a progenitor mass of 8.5 ± 0.9 $M_\odot$ for an ONe core, and 12^{+4}_{-2} $M_\odot$ for CO, whereas WD2 is estimated as 6.3 ± 0.3 $M_\odot$ and 7.2 ± 0.6 $M_\odot$ for ONe and CO cores, respectively. Spectra and fits for WDs 3 through 5 are presented in Miller et al. [88]. WDs 3 and 4 were found to be just under 1 $M_\odot$ with cooling ages older than the cluster's age, precluding membership. For a ONe core, the best fit for WD5 gives a mass of 1.12 ± 0.02 $M_\odot$ with a cooling age of just 3 ± 1 Myrs for a progenitor mass of 5.9 ± 0.2 $M_\odot$, while CO core fits give 1.14 ± 0.02 $M_\odot$, 12 ± 4 Myrs, and 6.2 ± 0.3 $M_\odot$, respectively. WDs 1, 2, and 5 are considered high-confidence cluster members, with WD1 being the most massive high-confidence cluster WD included in our results.

5.6 Hyades

Due to its proximity and significant extent, the Hyades is not identifiable via the R21 method. Instead, it was found via a Gaia EDR3 crossmatch of the Lodieu et al. [84] Hyades Gaia DR2 catalogue. We initially fit PARSEC isochrones to the crossmatched EDR3 CMD, using a metallicity of $[\mathrm{Fe/H}] = +0.146$ from Cummings et al. [28]. We find that these isochrones do not well represent either the MSTO or the low mass MS at this metallicity. Recent work by Gossage et al. [52] examined the Hyades with Tycho B_T and V_T photometry [59] finding a higher metallicity of $[\mathrm{Fe/H}] = +0.24$. In Fig. 5.9 we show the Hyades EDR3 CMD with PARSEC isochrones from 650 to 725 Myrs using the Gossage et al. [52] metallicity estimate.

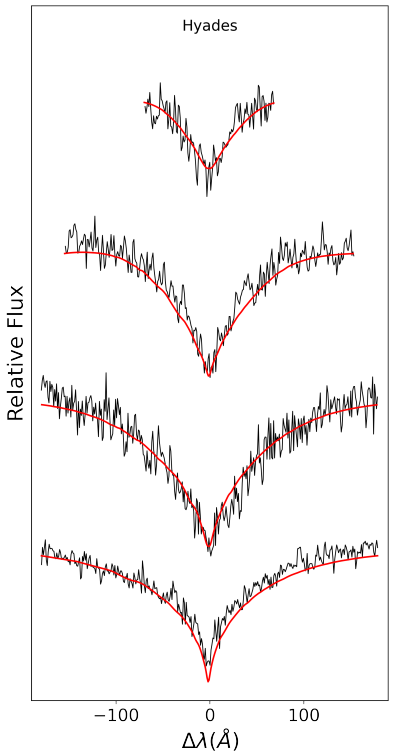

Figure 5.8: As in Fig. 5.1, but for the Hyades using pure H models.

We find that the higher metallicity significantly improves the quality of the fit, particularly for the lower MS. The 675, 700, and 725 Myr isochrones provide strong fits to the MSTO and giant stars. From these, we estimate an age of 700 ± 25 $M_{\odot}$. This estimate agrees within uncertainty with the age of 676^{+67}_{-11} Myrs found by Gossage et al. [52].

Due to an extremely bright contaminating star placed in the slit with the target WD during one set of observations with the Gemini spectrograph, only 3 of the 8 Gemini exposures were usable. This leads to a particularly low SNR and significantly increases the uncertainty in model fits. Additionally, models only go up to a maximum of $\log g = 9.5$ cm s^{-2}, and we find that this WD may be near the edge of the model grid and, therefore, not well modelled. Attempts at simultaneously fitting the Balmer lines were unsuccessful and could not typically converge to a solution. With very specific initial guesses, we sometimes managed to find a fit.

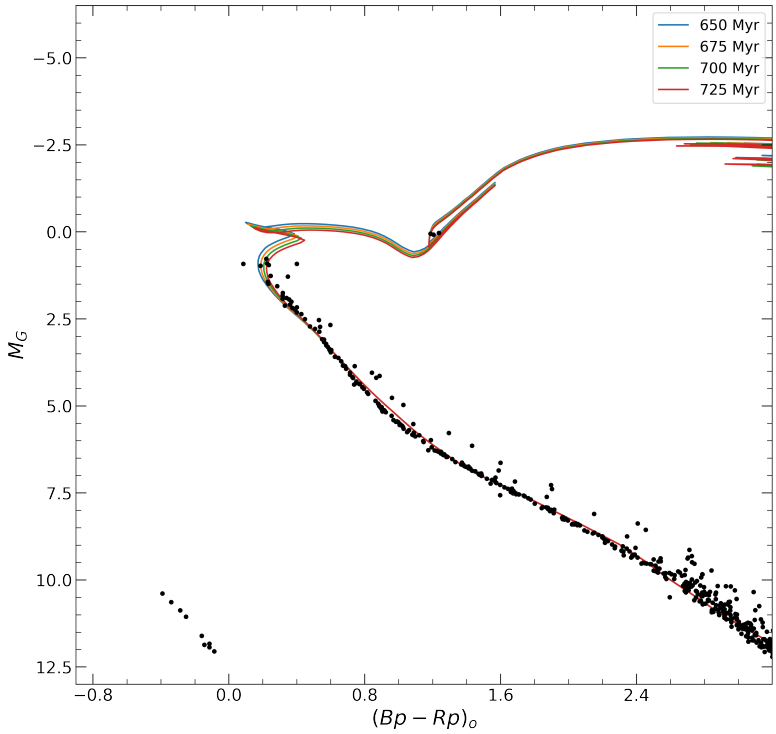

Figure 5.9: As in Fig. 5.2, but for the Hyades with a metallicity of $[\mathrm{Fe/H}] = +0.24$.

Given the bias due to the requirement of these initial guesses, we do not consider these fits trustworthy. In Fig. 5.8 we show an example fit of $\log g = 9.26 \pm 0.12$ cm s^{-2} with a temperature of $26,600 \pm 1,200$ K, intended as merely an illustration and not a precise claim of its parameters.

To better assess the atmospheric parameters, we compared the fit to the well-known ultramassive WD GD50. GD50 is a particularly massive WD that was once thought to be a part of the Pleiades cluster but is now considered part of the AB Doradus moving group [43]. Recent studies of GD50 have found masses > 1.24 $M_\odot$ with log g estimates between 9.09 and 9.20 cm s^{-2} (see e.g. [53], [79], [73]). We find a best fit for the Guo et al. [53] GD50 spectra of $\log g = 9.11 \pm 0.01$ cm s^{-2} with $T_{\mathrm{eff}} = 44,800 \pm 500$ K. We compare the fit for GD50 to the Hyades in Fig. 5.10. The significantly different temperatures of the two WDs make direct visual comparisons challenging. To combat this, we also include a fit that uses the

GD50 log g but changes the temperature to match the Hyades fit. Comparing this fit to the Hyades spectra, we see that the spectra have increased stark broadening compared to the GD50 fit, particularly for Hβ, which has the most influence on the determined surface gravity.

Between the parameters for the fit in Fig. 5.8, and the comparison with GD50, we estimate that the WD has a surface gravity of at least 9.20 cm s^{-2}, with a value above 9.50 completely plausible, and a temperature below 30,000 K. This range of fit parameters would give a particularly ultramassive WD that is at least 1.2 M$_\odot$, and could very well be above 1.3 M$_\odot$. A mass of 1.3 M$_\odot$ and a temperature of 20,000 K would place the cooling age close to the cluster age, potentially supporting membership. Alternatively, a temperature closer to 30,000 K would make the WD upwards of 250 Myr younger than the cluster, in which case the progenitor mass would be far too low for such a massive WD to have been a cluster member. Without confident atmospheric parameters, we cannot determine cooling parameters or progenitor mass to establish cluster membership better. While we do not confirm membership, we also do not rule it out, and we emphasize that the close approach of the WD to the cluster provides strong support for potential membership. Even if this object was not a cluster member, it is still a particularly massive WD and, therefore, worth additional study. Better modelling of high surface gravity WDs is paramount to analyze the spectra of this and other extremely massive WDs.

5.7 vdB Hagen 99

The candidate ultramassive WD identified in vdB Hagen 99 is the only candidate ultramassive WD we select for follow-up observation that we believe to be a current cluster member and not an escapee. The spectrum, shown in Fig. 4.5, has unnaturally sharp lines, particularly Hβ, but to a lesser extent Hγ and Hδ as well. Visually, the sharpness of the central depth of these lines does not seem to match the effective temperature of the WD. The raw unreduced spectra were examined for potential issues or troublesome skylines, to no avail. It is not clear what is causing the issue. The best way to assess would be to take an additional spectrum, with Gemini or another large telescope, and to see if the same sharp feature exists. As

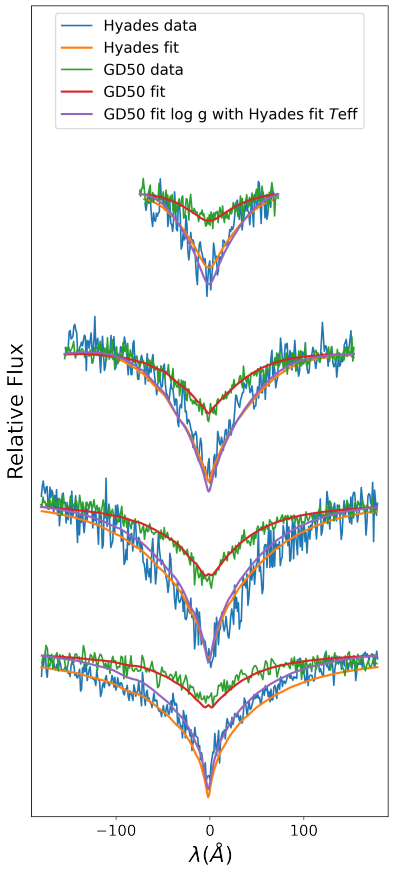

Figure 5.10: Comparison of Hyades WD spectra to GD50 spectra from Guo et al. [53]. Hyades data and fit are as in Fig. 5.8. GD50 Balmer lines were extracted and fit using the same methodology as the Hyades. The purple line illustrates a fit using the GD50 log g along with the Hyades $T_{\rm eff}$.

it stands, we are uncertain as to whether this is an artifact of the observations or a real feature.

For the age of the cluster we considered PARSEC isochrones at solar metallicity [11] for ages from 40 to 70 Myrs, as shown in Fig. 5.12. We use a cluster reddening of E(Bp-Rp)= 0.15, as found in R21. Each isochrone matches well to the central MS, supporting the use of solar metallicity. The lower main sequence is best described by the 50 Myr isochrone, suggesting an even slightly lower age of

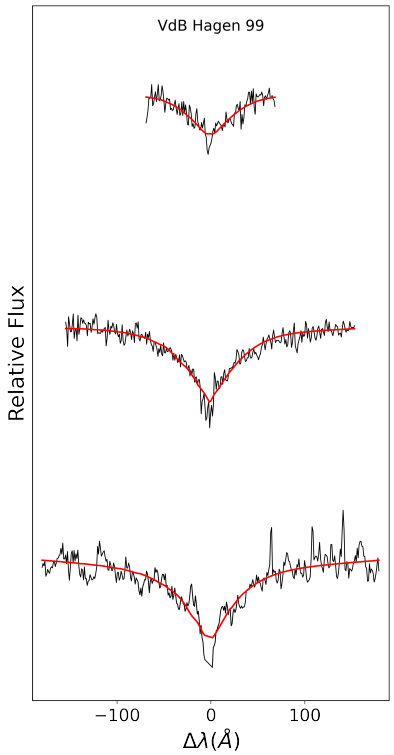

Figure 5.11: As in Fig. 5.1, but for vdB Hagen 99 using metal polluted models.

45 Myr. The brightest MSTO star is best described by the 60 Myr isochrone, the 70 Myr isochrone fits this one as well but is a very poor fit to the lower MS. The bluest MSTO star best matches the 50 Myr isochrone. Overall, we estimate an a best estimate of the cluster age of 55 ± 10 Myrs.

We extract the Balmer lines and fit the spectrum using metal polluted H atmosphere models to estimate the WD atmospheric parameters. To reduce error due to the sharp depth, we ignore the central region of Hβ in our fits. The best fit parameters give $T_{\rm eff} = 58,400 \pm 1,000$ K and log g $= 8.64 \pm 0.04$ cm s^{-2}, suggesting a very young WD with an age of just 1 ± 1 Myr and mass of 1.05 ± 0.02 M$_\odot$, for a progenitor mass of $6.2^{+0.2}_{-0.8}$ M$_\odot$. While these parameters place the object sensibly in the IFMR, we emphasize that we are not confident in the temperature estimate due to the sharp central depth of the Balmer lines. The proximity of the WD to the

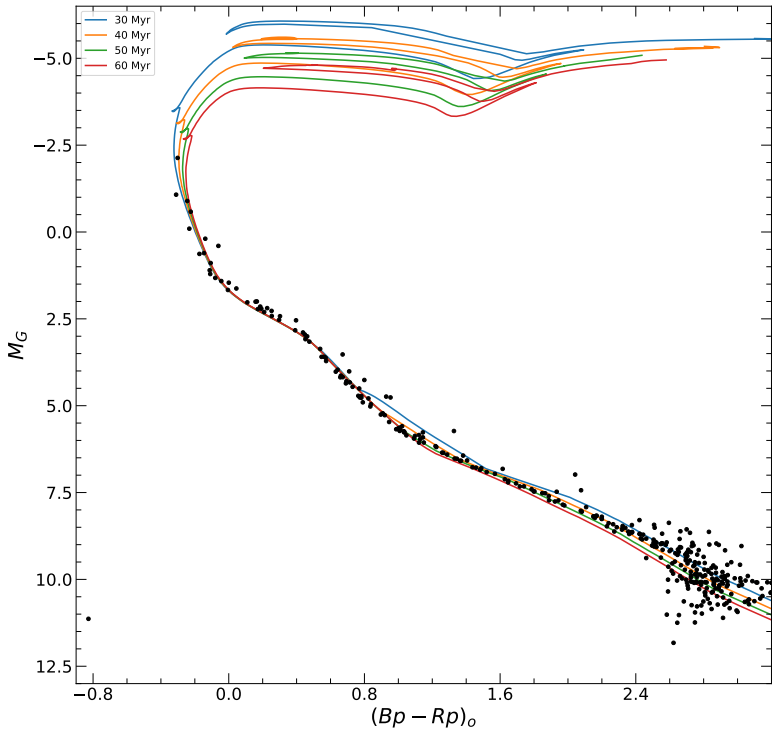

Figure 5.12: As in Fig. 5.2, but for vdB Hagen 99.

cluster certainly favours membership, but without an accurate temperature and age, we choose to be ambiguous as to whether this candidate is indeed a cluster member. Additional spectroscopy to assess whether the sharp centres of the Balmer lines are a real feature is required to better assess candidacy.

5.8 Binary Mergers and Chance Encounters

A couple of key factors are worthy of consideration before finalizing the updated IFMR; the assumption of single star evolution and the possibility of chance encounters. Temmink et al. [129] studied the prevalence of binary mergers in single WD evolution and found that approximately 10 to 30% of WDs have had past binary mergers, increasing to between 30 to 50% for massive WDs. WDs typically take 3 to 5 times as long to form via binary evolution, shifting the progenitor age by hundreds of millions of years for massive WDs [129]. Given the young age

of clusters examined in this work, we rule out cluster membership for any of our identified WDs, which are binary merger products. While we cannot strictly rule out past mergers from the WD's spectra, one way to examine this is to estimate the probability that the WDs are merely chance encounters, as would have to be the case if they are not cluster members.

Alpha Persei WDs 1 and 2 were found by H21b from a total search volume of 6.4×10^6 cubic pc. In that volume, just 0.15% of sources have proper motions consistent with past cluster membership. Of these, H21b estimate that 43% are potentially interlopers. We can estimate the probability of these WDs being chance encounters by comparing them to the prevalence of massive WDs in the solar neighbourhood. Fleury et al. [40] examined the Gentile Fusillo et al. [49] catalogue for WDs with ages less than 250 Myr that were within 200 pc of the Sun. From this sample they estimate that approximately 100 of the WDs have masses of at least 0.95 $M_\odot$. The total volume within 200 pc of the Sun is roughly 3.3×10^7 pc^3. Combining these factors Miller et al. [88] estimate we should find just 0.012 young massive WDs in this volume whose motion is consistent with past cluster membership. In the mass range above 1.15 $M_\odot$, consistent with the masses of WDs 1 and 2, the number of expected WDs is a factor of 15 smaller [40].

We cannot use the same calculation to estimate the probability that the remaining WDs are interlopers. Instead, we determine a crude estimate by looking at the fraction of massive WDs found in the 200 pc sample. Fleury et al. [40] estimated that just one of every thousand WDs in this sample have $M > 0.95$ $M_\odot$ and ages under 250 Myrs. From the Gentile Fusillo et al. [49] catalogue we identified 62 WDs which potentially escaped from Alpha Persei, while for the Hyades it was 151. For the wide search clusters, which were developed from the Gentile Fusillo et al. [48] catalogue, we identified 13 potential escapees from NGC 2516 and 34 for NGC 2422. The Gaia EDR3 WD catalogue contains approximately 38% more WDs than DR2. To account for this increased sample, we scale these numbers to roughly 18 and 47. Using the aforementioned massive WD fraction, we estimate the number of expected massive WDs in the search region for each of these clusters as 0.06, 0.15, 0.02, and 0.05, for Alpha Persei, the Hyades, NGC 2516, and NGC 2422, respectively. As this is the expected number of WDs with $M > 0.95$ $M_\odot$, and we estimate each of these identified candidates has a mass of at least 1.1 $M_\odot$,

we except that the probability that these stars are interlopers is between a factor of two and fifteen smaller [40].

5.9 Implications and State of the IFMR

In Fig. 5.13 we display an updated IFMR including select WDs from Tab. 5.1, along with Pleiades WDs discovered and characterized by H21a. Included are all WDs we label as either questionable or high-confidence in our cluster membership determination in Tab. 5.1. The three high-confidence members are all Alpha Persei escapees, each displaying results for ONe core models. The questionable points are from NGC 2422, vdB Hagen 99, and NGC 2516. NGC 2422 and vdB Hagen 99 points use CO core results, while the NGC 2516 point displays an ONe core. While the NGC 2422 WD is in a mass range that favours a ONe core, progenitor mass estimates seem to rule out membership if it possesses a CO core. Given the channels for the potential formation of ultramassive CO WDs presented in Sec. 2.3, such a massive WD could have a CO core. We emphasize that we do not express any specific degree of confidence about the membership status of the three questionable members, but do not rule out membership, either. These three points are included in the IFMR to illustrate where they lie if cluster membership is favoured. Future work that examines the IFMR should exclude these points unless membership is better established.

The three most massive high-confidence cluster member WDs on the updated IFMR are all from the Alpha Persei cluster, the most massive of which has a progenitor mass of 8.5 ± 0.9 $M_{\odot}$. This is near the expected theoretical limit of 8 $M_{\odot}$ [136], despite the WD's mass being well below the Chandrasekhar limit. These results support the idea that the upper limit for WD production might be significantly higher or that WDs do not form with masses close to the Chandrasekhar limit. The second possibility is worth a closer examination. Kilic et al. [73] examined the Gaia DR2 sample of WDs within 100 pc from the Montreal White Dwarf Database [33] and found 23 WDs with masses above 1.25 $M_{\odot}$ if the WDs are H dominated ONe core WDs, with 2 of those being over 1.3 $M_{\odot}$. If these same WDs possess CO cores, all 25 would be above 1.3 $M_{\odot}$. Even if 30 to 50% of these WDs are binary merger products, as expected by Temmink et al. [129], a fair fraction are likely

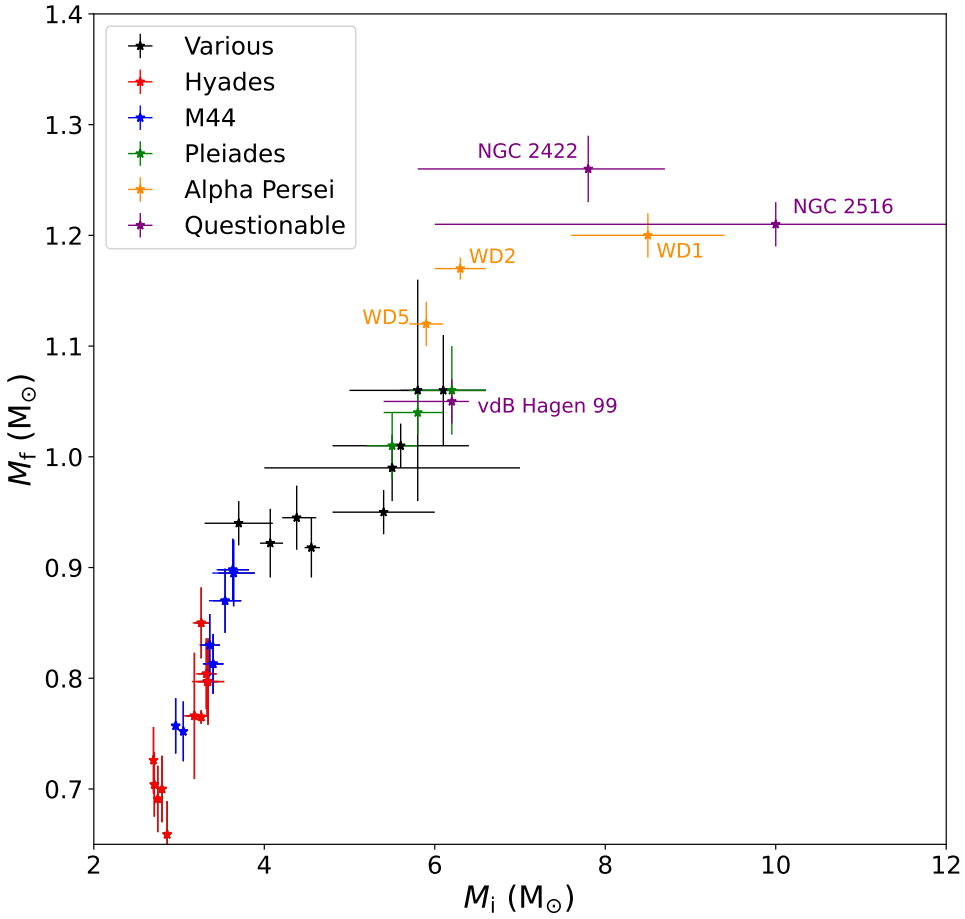

Figure 5.13: Updated IFMR. Hyades, Various, and M44 from R21 as in Fig. 1.6. Pleiades points are from H21a found via their reconstructed velocity method. The remainder are as described in this work. Alpha Persei and NGC 2516 points are for ONe cores, while the remainder are for CO.

formed from single stellar evolution. As such, the Kilic et al. [73] result combined with our knowledge of the IFMR suggests a significant increase in the upper mass limit for WD production, even when accounting for binary merger fractions.

Collectively, we see that the addition of escapee WDs examined in this work and by H21a has done much to populate the high mass region of the IFMR. Five of the seven most massive high-confidence cluster member WDs come from the escapee search method developed by H21a, with an additional two ultramassive escapees considered questionable members from the wide search. R21 searched more than 200 young open clusters for candidate WDs and found none with masses above 1.06 $M_{\odot}$ or progenitors above 6.2 $M_{\odot}$. In escapee searches in this work and H21a, we have identified between 3 and 5 cluster WDs with masses above 1.06 $M_{\odot}$ and the same number with progenitors above 6.2 $M_{\odot}$, despite only searching a relatively small number of clusters. This strongly suggests that the shortage of high-mass WDs in clusters largely results from WDs escaping from their birth clusters.

Chapter 6

Conclusions

The maximum mass of a white dwarf progenitor is not well understood, primarily due to an inability to identify ultramassive cluster member WDs and populate the high-mass region of the IFMR. While the Gaia mission has provided an unprecedented data set to search for these massive WDs, broad searches have failed to identify any cluster member WDs with masses above 1.06 $M_{\odot}$ or progenitors above 6.2 $M_{\odot}$. Evidence suggests that ultramassive WDs may be particularly likely to escape their birth clusters due to experiencing a velocity kick of a few km s^{-1} at birth. We consider this possibility and search for WDs which may have escaped from a sample of nearby young clusters as a means of populating the high-mass region of the IFMR.

We employ two techniques to identify ultramassive WD escapees. The first searches an extensive region around the clusters for WDs whose proper motion is consistent with the cluster. In contrast, the second employs a more sophisticated technique which attempts to reconstruct the 3D velocity of candidates and identify those which were close to the cluster in the past. While the second technique is preferred, it ignores astrometric uncertainties, which makes the method unreliable for clusters more than 200 pc away or older than 200 Myrs.

From the first method, we identified 151 candidate escapee WDs from a sample of 40 clusters, from which we selected six promising candidates for additional follow-up. The second method found six candidates from searches of the Hyades and Alpha Persei clusters. Additionally, we identified one candidate ultramassive

WD which appears to be a current cluster member of vdB Hagen 99 that had not previously been identified. We obtained follow-up spectroscopy for all thirteen candidates, ten of which were obtained for this work with the Gemini telescope.

For each candidate, we determine the effective temperature and surface gravity using non-local thermodynamic equilibrium hydrogen atmosphere models, considering both pure H and metal polluted models. These atmospheric parameters are then used to determine the mass and cooling age of the WD, using CO models for all WDs and ONe models for those above 1.05 $M_{\odot}$. We determine each cluster's age from isochrones, additionally considering literature ages. The WD's cooling age is then subtracted from the cluster's age, leading to an estimate of the progenitor lifetime and its mass.

Of this set of thirteen candidates, we find three high-confidence escapees, each from the Alpha Persei cluster. Three additional candidates are considered questionable escapees, where we cannot confirm nor exclude potential past membership. Six of the remaining seven candidates are non-members due to their cooling ages being inconsistent with former cluster membership. The final candidate is a questionable member from vdB Hagen 99. We update the IFMR from Richer et al. [112] to include the three high-confidence escapees and three of the four questionable ones. The final questionable one is an extremely massive WD potentially escaped from the Hyades, but a low SNR spectrum combined with surface gravity seemingly near the edge of model grids prevented a confidence estimation of its atmospheric parameters. Additionally, we include two escapees and one cluster member WD from the Pleiades found in Heyl et al. [56].

The three high-confidence escapees from Alpha Persei are each the most massive cluster WDs known, with among the most massive progenitors. The most massive of which, Alpha Persei WD1, has an estimated mass of 8.5 $M_{\odot}$, which is beyond the theoretical limit of 8 $M_{\odot}$. Given that this WD is well below the Chandrasekhar mass, it suggests that the high-mass limit for WD production may be well above the theoretical limit. While this work has advanced our understanding of the high-mass region of the WD IFMR, the maximum mass of a WD progenitor remains a mystery. Our results lead us to believe that many more of these escaped WDs are out there, waiting to be identified.

In addition to the identification challenges, precise cluster age determination is

one of the most significant problems we encounter. In many cases, age estimates are from isochrones fits and are driven by a handful of main sequence turnoff and giant stars. The limited number of stars that the fit is based on often leads to significant uncertainty in the cluster's age. For the precursors of ultramassive WDs, which have relatively short main sequence lifetimes, uncertain cluster ages lead to significant uncertainty in progenitor mass estimates, often to the point where no reliable progenitor mass estimate is possible. More precise age determinations would go a long way to help develop the high-mass region of the IFMR. In the future, we will work to develop additional methods to identify escapee ultramassive WDs, as well as to increase the precision in the estimated ages of their potential birth clusters.

Bibliography

[1] L. G. Althaus et al. The formation of DA white dwarfs with thin hydrogen envelopes. *A&A*, 440(1):L1–L4, Sept. 2005. doi:10.1051/0004-6361:200500159. → pages 17, 35

[2] L. G. Althaus et al. New phase diagrams for dense carbon-oxygen mixtures and white dwarf evolution. *A&A*, 537:A33, Jan. 2012. doi:10.1051/0004-6361/201117902. → page 36

[3] L. G. Althaus et al. The formation of ultra-massive carbon-oxygen core white dwarfs and their evolutionary and pulsational properties. *A&A*, 646: A30, Feb. 2021. doi:10.1051/0004-6361/202038930. → pages 19, 36

[4] R. Andrae et al. Gaia Data Release 2. First stellar parameters from Apsis. *A&A*, 616:A8, Aug. 2018. doi:10.1051/0004-6361/201732516. → page 32

[5] I. Baraffe and G. Chabrier. A closer look at the transition between fully convective and partly radiative low-mass stars. *A&A*, 619:A177, Nov. 2018. doi:10.1051/0004-6361/201834062. → page 18

[6] G. Beccari and G. Carraro. Introduction to the Theory of Stellar Evolution. In H. M. J. Boffin, G. Carraro, and G. Beccari, editors, *Astrophysics and Space Science Library*, volume 413 of *Astrophysics and Space Science Library*, page 1, Jan. 2015. doi:10.1007/978-3-662-44434-4_1. → pages 6, 7, 9, 10, 12, 15

[7] A. Bédard, P. Bergeron, P. Brassard, and G. Fontaine. On the Spectral Evolution of Hot White Dwarf Stars. I. A Detailed Model Atmosphere Analysis of Hot White Dwarfs from SDSS DR12. *ApJ*, 901(2):93, Oct. 2020. doi:10.3847/1538-4357/abafbe. → pages 36, 39

[8] P. Bergeron, R. A. Saffer, and J. Liebert. A Spectroscopic Determination of the Mass Distribution of DA White Dwarfs. *ApJ*, 394:228, July 1992. doi:10.1086/171575. → page 33

[9] L. C. Bermúdez-Bustamante, G. García-Segura, W. Steffen, and L. Sabin. AGB winds in interacting binary stars. *MNRAS*, 493(2):2606–2617, Apr. 2020. doi:10.1093/mnras/staa403. → page 13

[10] T. Blöcker. Structure and Evolution of AGB Stars. In T. Le Bertre, A. Lebre, and C. Waelkens, editors, *Asymptotic Giant Branch Stars*, volume 191, page 21, Jan. 1999. → page 11

[11] D. Bossini et al. Age determination for 269 Gaia DR2 open clusters. *A&A*, 623:A108, Mar. 2019. doi:10.1051/0004-6361/201834693. → pages 65, 78

[12] L. G. Bouma et al. Rotation and Lithium Confirmation of a 500 pc Halo for the Open Cluster NGC 2516. *AJ*, 162(5):197, Nov. 2021. doi:10.3847/1538-3881/ac18cd. → page 71

[13] A. Bressan et al. PARSEC: stellar tracks and isochrones with the PAdova and TRieste Stellar Evolution Code. *MNRAS*, 427(1):127–145, Nov. 2012. doi:10.1111/j.1365-2966.2012.21948.x. → pages xiv, 7, 37, 50, 67

[14] J. M. Brown, M. Kilic, W. R. Brown, and S. J. Kenyon. The Binary Fraction of Low-mass White Dwarfs. *ApJ*, 730(2):67, Apr. 2011. doi:10.1088/0004-637X/730/2/67. → page 26

[15] W. R. Brown, M. Kilic, C. Allende Prieto, and S. J. Kenyon. The ELM Survey. I. A Complete Sample of Extremely Low-mass White Dwarfs. *ApJ*, 723(2):1072–1081, Nov. 2010. doi:10.1088/0004-637X/723/2/1072. → page 26

[16] W. R. Brown, M. Kilic, A. Kosakowski, and A. Gianninas. Discovery of a Detached, Eclipsing 40 Minute Period Double White Dwarf Binary and a Friend: Implications for He+CO White Dwarf Mergers. *ApJ*, 847(1):10, Sept. 2017. doi:10.3847/1538-4357/aa8724. → page 19

[17] L. R. Buchmann and C. A. Barnes. Nuclear reactions in stellar helium burning and later hydrostatic burning stages. *Nucl. Phys. A*, 777:254–290, 2006. doi:10.1016/j.nuclphysa.2005.01.005. → page 9

[18] M. E. Camisassa et al. The evolution of ultra-massive white dwarfs. *A&A*, 625:A87, May 2019. doi:10.1051/0004-6361/201833822. → pages 17, 36, 39

[19] M. E. Camisassa et al. Forever young white dwarfs: When stellar ageing stops. *A&A*, 649:L7, May 2021. doi:10.1051/0004-6361/202140720. → page 17

[20] M. E. Camisassa et al. The evolution of ultra-massive carbon-oxygen white dwarfs. *MNRAS*, 511(4):5198–5206, Apr. 2022. doi:10.1093/mnras/stac348. → pages 19, 36

[21] T. Cantat-Gaudin et al. A Gaia DR2 view of the open cluster population in the Milky Way. *A&A*, 618:A93, Oct. 2018. doi:10.1051/0004-6361/201833476. → pages 30, 40

[22] L. Casagrande and D. A. VandenBerg. On the use of Gaia magnitudes and new tables of bolometric corrections. *MNRAS*, 479(1):L102–L107, Sept. 2018. doi:10.1093/mnrasl/sly104. → page 50

[23] S. Catalán, J. Isern, E. García-Berro, and I. Ribas. The initial-final mass relationship of white dwarfs revisited: effect on the luminosity function and mass distribution. *MNRAS*, 387(4):1693–1706, July 2008. doi:10.1111/j.1365-2966.2008.13356.x. → pages 2, 20

[24] M. C. Chen, F. Herwig, P. A. Denissenkov, and B. Paxton. The dependence of the evolution of Type Ia SN progenitors on the C-burning rate uncertainty and parameters of convective boundary mixing. *MNRAS*, 440 (2):1274–1280, May 2014. doi:10.1093/mnras/stu108. → page 19

[25] Y.-H. Chu et al. Hard X-Ray Emission Associated with White Dwarfs. IV. Signs of Accretion from Substellar Companions. *ApJ*, 910(2):119, Apr. 2021. doi:10.3847/1538-4357/abe5a5. → page 14

[26] E. Cukanovaite et al. Pure-helium 3D model atmospheres of white dwarfs. *MNRAS*, 481(2):1522–1537, Dec. 2018. doi:10.1093/mnras/sty2383. → page 17

[27] J. D. Cummings and J. S. Kalirai. Improved Main-sequence Turnoff Ages of Young Open Clusters: Multicolor UBV Techniques and the Challenges of Rotation. *AJ*, 156(4):165, Oct. 2018. doi:10.3847/1538-3881/aad5df. → pages 67, 73

[28] J. D. Cummings, C. P. Deliyannis, R. M. Maderak, and A. Steinhauer. WIYN Open Cluster Study. LXXV. Testing the Metallicity Dependence of Stellar Lithium Depletion Using Hyades-aged Clusters. I. Hyades and Praesepe. *AJ*, 153(3):128, Mar. 2017. doi:10.3847/1538-3881/aa5b86. → page 74

[29] J. D. Cummings et al. The White Dwarf Initial-Final Mass Relation for Progenitor Stars from 0.85 to 7.5 M $_\odot$. *ApJ*, 866(1):21, Oct. 2018. doi:10.3847/1538-4357/aadfd6. → pages xi, 2, 24, 39

[30] J. H. J. de Bruijne, R. Hoogerwerf, and P. T. de Zeeuw. A Hipparcos study of the Hyades open cluster. Improved colour-absolute magnitude and Hertzsprung-Russell diagrams. *A&A*, 367:111–147, Feb. 2001. doi:10.1051/0004-6361:20000410. → page 50

[31] C. L. Doherty, P. Gil-Pons, L. Siess, and J. C. Lattanzio. Super-AGB Stars and their Role as Electron Capture Supernova Progenitors. *PASA*, 34:e056, Nov. 2017. doi:10.1017/pasa.2017.52. → pages 12, 13, 19

[32] P. Dufour et al. Hot DQ White Dwarfs: Something Different. *ApJ*, 683(2): 978–989, Aug. 2008. doi:10.1086/589855. → page 18

[33] P. Dufour et al. The Montreal White Dwarf Database: A Tool for the Community. In P. E. Tremblay, B. Gaensicke, and T. Marsh, editors, *20th European White Dwarf Workshop*, volume 509 of *Astronomical Society of the Pacific Conference Series*, page 3, Mar. 2017. → pages 22, 82

[34] D. J. Eisenstein et al. A Catalog of Spectroscopically Confirmed White Dwarfs from the Sloan Digital Sky Survey Data Release 4. *ApJS*, 167(1): 40–58, Nov. 2006. doi:10.1086/507110. → page 20

[35] K. El-Badry, H.-W. Rix, and D. R. Weisz. An Empirical Measurement of the Initial-Final Mass Relation with Gaia White Dwarfs. *ApJL*, 860(2): L17, June 2018. doi:10.3847/2041-8213/aaca9c. → page 2

[36] M. F. El Eid. Comments on stellar evolution. *European Physical Journal Plus*, 133(9):372, Sept. 2018. doi:10.1140/epjp/i2018-12236-2. → pages 6, 9, 10, 11

[37] D. W. Evans et al. Gaia Data Release 2. Photometric content and validation. *A&A*, 616:A4, Aug. 2018. doi:10.1051/0004-6361/201832756. → pages 21, 30

[38] M. Fellhauer et al. The White Dwarf Deficit in Open Clusters: Dynamical Processes. *ApJL*, 595(1):L53–L56, Sept. 2003. doi:10.1086/379005. → pages 26, 27

[39] Z.-W. Feng et al. Higher-order generalized uncertainty principle corrections to the Jeans mass. *EPJB*, 81(8):754, Aug. 2021. doi:10.1140/epjc/s10052-021-09549-z. → page 5

[40] L. Fleury, I. Caiazzo, and J. Heyl. The cooling of massive white dwarfs from Gaia EDR3. *MNRAS*, 511(4):5984–5993, Apr. 2022. doi:10.1093/mnras/stac458. → pages 22, 81, 82

[41] G. Fontaine, P. Brassard, and P. Bergeron. The Potential of White Dwarf Cosmochronology. *PASP*, 113(782):409–435, Apr. 2001. doi:10.1086/319535. → pages 1, 15, 20

[42] J. M. Fregeau, H. B. Richer, F. A. Rasio, and J. R. Hurley. The Dynamical Effects of White Dwarf Birth Kicks in Globular Star Clusters. *ApJL*, 695 (1):L20–L24, Apr. 2009. doi:10.1088/0004-637X/695/1/L20. → page 26

[43] J. Gagné, G. Fontaine, A. Simon, and J. K. Faherty. A Young Ultramassive White Dwarf in the AB Doradus Moving Group. *ApJL*, 861(2):L13, July 2018. doi:10.3847/2041-8213/aacdff. → page 76

[44] Gaia Collaboration et al. The Gaia mission. *A&A*, 595:A1, Nov. 2016. doi:10.1051/0004-6361/201629272. → pages 2, 20, 25

[45] Gaia Collaboration et al. Gaia Data Release 2. Observational Hertzsprung-Russell diagrams. *A&A*, 616:A10, Aug. 2018. doi:10.1051/0004-6361/201832843. → page 20

[46] Gaia Collaboration et al. Gaia Data Release 2. Summary of the contents and survey properties. *A&A*, 616:A1, Aug. 2018. doi:10.1051/0004-6361/201833051. → pages 22, 23, 29, 44, 64

[47] Gaia Collaboration et al. Gaia Early Data Release 3. Summary of the contents and survey properties. *A&A*, 649:A1, May 2021. doi:10.1051/0004-6361/202039657. → pages 22, 29, 30, 31, 53, 64

[48] N. P. Gentile Fusillo et al. A gaia data release 2 catalogue of white dwarfs and a comparison with sdss. *MNRAS*, 482(4):4570, Nov 2018. ISSN 1365-2966. doi:10.1093/mnras/sty3016. → pages 22, 38, 81

[49] N. P. Gentile Fusillo et al. A catalogue of white dwarfs in Gaia EDR3. *MNRAS*, 508(3):3877–3896, Dec. 2021. doi:10.1093/mnras/stab2672. → pages xi, xiii, 16, 22, 49, 50, 51, 53, 81

[50] A. Gianninas, P. Bergeron, J. Dupuis, and M. T. Ruiz. Spectroscopic Analysis of Hot, Hydrogen-rich White Dwarfs: The Presence of Metals and the Balmer-line Problem. *ApJ*, 720(1):581–602, Sept. 2010. doi:10.1088/0004-637X/720/1/581. → pages xiv, 35, 65, 66, 72

[51] F. C. Gillett et al. The Gemini Telescopes Project (Invited Paper). In E. Falco, J. A. Fernandez, and R. F. Ferrero, editors, *Revista Mexicana de Astronomia y Astrofisica Conference Series*, volume 4 of *Revista Mexicana de Astronomia y Astrofisica Conference Series*, page 75, Nov. 1996. → page 54

[52] S. Gossage et al. Age Determinations of the Hyades, Praesepe, and Pleiades via MESA Models with Rotation. *ApJ*, 863(1):67, Aug. 2018. doi:10.3847/1538-4357/aad0a0. → pages 50, 64, 74, 75

[53] J. Guo et al. White dwarfs identified in LAMOST DR 2. *MNRAS*, 454(3): 2787–2797, Dec. 2015. doi:10.1093/mnras/stv2104. → pages xiv, 76, 78

[54] M. Hajduk et al. The cooling-down central star of the planetary nebula SwSt 1: a late thermal pulse in a massive post-AGB star? *MNRAS*, 498(1): 1205–1220, Oct. 2020. doi:10.1093/mnras/staa2274. → page 14

[55] J. Heyl, I. Caiazzo, H. Richer, and D. R. Miller. Reconstructing Nearby Young Clusters with Gaia EDR3. *arXiv e-prints*, art. arXiv:2110.04296, Oct. 2021. → pages v, 48, 73

[56] J. Heyl, I. Caiazzo, and H. B. Richer. Reconstructing the Pleiades with Gaia EDR3. *ApJ*, 926(2):132, Feb. 2022. doi:10.3847/1538-4357/ac45fc. → pages v, vi, 43, 86

[57] N. R. Hinkel et al. Stellar Abundances in the Solar Neighborhood: The Hypatia Catalog. *AJ*, 148(3):54, Sept. 2014. doi:10.1088/0004-6256/148/3/54. → page 36

[58] T. Hoang. Effect of Dust Rotational Disruption by Radiative Torques on Radiation Pressure Feedback from Massive Protostars. *ApJ*, 921(1):21, Nov. 2021. doi:10.3847/1538-4357/ac185d. → page 5

[59] E. Høg et al. The Tycho-2 catalogue of the 2.5 million brightest stars. *A&A*, 355:L27–L30, Mar. 2000. → page 74

[60] J. B. Holberg et al. A New Look at the Local White Dwarf Population. *AJ*, 135(4):1225–1238, Apr. 2008. doi:10.1088/0004-6256/135/4/1225. → page 26

[61] S. Horiuchi et al. The Cosmic Core-collapse Supernova Rate Does Not Match the Massive-star Formation Rate. *ApJ*, 738(2):154, Sept. 2011. doi:10.1088/0004-637X/738/2/154. → page 1

[62] J. Iben, I., J. B. Kaler, J. W. Truran, and A. Renzini. On the evolution of those nuclei of planetary nebulae that experiencea final helium shell flash. *ApJ*, 264:605–612, Jan. 1983. doi:10.1086/160631. → page 13

[63] J. Iben, Icko. Single and Binary Star Evolution. *ApJS*, 76:55, May 1991. doi:10.1086/191565. → page 7

[64] J. Isern, S. Torres, and A. Rebassa-Mansergas. White dwarfs as Physics laboratories: lights and shadows. *Frontiers in Astronomy and Space Sciences*, 9:6, Jan. 2022. doi:10.3389/fspas.2022.815517. → page 15

[65] A. G. Istrate, T. M. Tauris, N. Langer, and J. Antoniadis. The timescale of low-mass proto-helium white dwarf evolution. *A&A*, 571:L3, Nov. 2014. doi:10.1051/0004-6361/201424681. → page 18

[66] Ž. Ivezić et al. Sloan Digital Sky Survey Standard Star Catalog for Stripe 82: The Dawn of Industrial 1% Optical Photometry. *AJ*, 134(3):973–998, Sept. 2007. doi:10.1086/519976. → page 31

[67] I. Jordan, George C., H. B. Perets, R. T. Fisher, and D. R. van Rossum. Failed-detonation Supernovae: Subluminous Low-velocity Ia Supernovae and their Kicked Remnant White Dwarfs with Iron-rich Cores. *ApJL*, 761 (2):L23, Dec. 2012. doi:10.1088/2041-8205/761/2/L23. → page 19

[68] J. S. Kalirai et al. The CFHT Open Star Cluster Survey. III. The White Dwarf Cooling Age of the Rich Open Star Cluster NGC 2099 (M37). *AJ*, 122(6):3239–3257, Dec. 2001. doi:10.1086/324463. → page 25

[69] J. S. Kalirai, G. G. Fahlman, H. B. Richer, and P. Ventura. The CFHT Open Star Cluster Survey. IV. Two Rich, Young Open Star Clusters: NGC 2168 (M35) and NGC 2323 (M50). *AJ*, 126(3):1402–1414, Sept. 2003. doi:10.1086/377320. → page 25

[70] J. S. Kalirai et al. The Initial-Final Mass Relation: Direct Constraints at the Low-Mass End. *ApJ*, 676(1):594–609, Mar. 2008. doi:10.1086/527028. → page 2

[71] A. I. Karakas. Stellar evolution from the main sequence to the post-AGB phase. In A. A. Zijlstra, F. Lykou, I. McDonald, and E. Lagadec, editors, *Asymmetric Planetary Nebulae 5 Conference*, page 144, Jan. 2011. → pages 5, 9, 11, 13

[72] M. Kilic et al. The ELM Survey. II. Twelve Binary White Dwarf Merger Systems. *ApJ*, 727(1):3, Jan. 2011. doi:10.1088/0004-637X/727/1/3. → page 26

[73] M. Kilic et al. The 100 pc White Dwarf Sample in the SDSS Footprint. *ApJ*, 898(1):84, July 2020. doi:10.3847/1538-4357/ab9b8d. → pages 76, 82, 84

[74] M. Kilic, P. Bergeron, S. Blouin, and A. Bédard. The most massive white dwarfs in the solar neighbourhood. *MNRAS*, 503(4):5397–5408, June 2021. doi:10.1093/mnras/stab767. → page 22

[75] D. Koester, B. T. Gänsicke, and J. Farihi. The frequency of planetary debris around young white dwarfs. *A&A*, 566:A34, June 2014. doi:10.1051/0004-6361/201423691. → page 18

[76] M. G. H. Krause et al. The Physics of Star Cluster Formation and Evolution. *SSR*, 216(4):64, June 2020. doi:10.1007/s11214-020-00689-4. → page 22

[77] P. Kroupa. The Initial Mass Function of Stars: Evidence for Uniformity in Variable Systems. *Science*, 295(5552):82–91, Jan. 2002. doi:10.1126/science.1067524. → pages xi, xiv, 8, 25, 37, 63, 67

[78] P. Kroupa and C. Weidner. Galactic-Field Initial Mass Functions of Massive Stars. *ApJ*, 598(2):1076–1078, Dec. 2003. doi:10.1086/379105. → pages 1, 3, 25, 65

[79] S. K. Leggett et al. Distant White Dwarfs in the US Naval Observatory Flagstaff Station Parallax Sample. *ApJS*, 239(2):26, Dec. 2018. doi:10.3847/1538-4365/aae7ca. → page 76

[80] Z. Li, X. Chen, H.-L. Chen, and Z. Han. Formation of Extremely Low-mass White Dwarfs in Double Degenerates. *ApJ*, 871(2):148, Feb. 2019. doi:10.3847/1538-4357/aaf9a1. → page 19

[81] J. Liebert, P. Bergeron, and J. B. Holberg. The Formation Rate and Mass and Luminosity Functions of DA White Dwarfs from the Palomar Green Survey. *ApJS*, 156(1):47–68, Jan. 2005. doi:10.1086/425738. → page 35

[82] S. Liljegren, S. Höfner, W. Nowotny, and K. Eriksson. Dust-driven winds of AGB stars: The critical interplay of atmospheric shocks and luminosity variations. *A&A*, 589:A130, May 2016. doi:10.1051/0004-6361/201527885. → page 26

[83] L. Lindegren et al. Gaia Early Data Release 3. The astrometric solution. *A&A*, 649:A2, May 2021. doi:10.1051/0004-6361/202039709. → page 31

[84] N. Lodieu, R. L. Smart, A. Pérez-Garrido, and R. Silvotti. A 3D view of the Hyades stellar and sub-stellar population. *A&A*, 623:A35, Mar. 2019. doi:10.1051/0004-6361/201834045. → pages xiii, 51, 52, 74

[85] A. V. Loktin and M. E. Popova. Updated version of the 'homogeneous catalog of open cluster parameters'. *Astrophysical Bulletin*, 72(3):257–265, July 2017. doi:10.1134/S1990341317030154. → pages 67, 68

[86] I. McDonald and A. A. Zijlstra. Pulsation-triggered Mass Loss from AGB Stars: The 60 Day Critical Period. *ApJL*, 823(2):L38, June 2016. doi:10.3847/2041-8205/823/2/L38. → pages 26, 27

[87] D. R. Miller et al. The Ultramassive White Dwarfs of the Alpha Persei Cluster. *ApJL*, 926(2):L24, Feb. 2022. doi:10.3847/2041-8213/ac50a5. → page v

[88] D. R. Miller et al. The Ultramassive White Dwarfs of the Alpha Persei Cluster. *ApJL*, 926(2):L24, Feb. 2022. doi:10.3847/2041-8213/ac50a5. → pages 49, 63, 74, 81

[89] J. J. Moré. The Levenberg-Marquardt algorithm: Implementation and theory. In *Lecture Notes in Mathematics*, volume 630, pages 105–116. Berlin Springer Verlag, 1978. doi:10.1007/BFb0067700. → page 35

[90] G. R. I. Moyano Loyola and J. R. Hurley. Stars on the run: escaping from stellar clusters. *MNRAS*, 434(3):2509–2528, Sept. 2013. doi:10.1093/mnras/stt1190. → page 27

[91] R. Napiwotzki and T. Rauch. The Balmer line problem of hot stars and the impact of ion-dynamical effects on the Stark broadening of HI and HeII lines. *A&A*, 285:603–608, May 1994. → page 35

[92] M. Netopil and E. Paunzen. Towards a photometric metallicity scale for open clusters. *A&A*, 557:A10, Sept. 2013. doi:10.1051/0004-6361/201321829. → page 73

[93] M. Netopil, E. Paunzen, U. Heiter, and C. Soubiran. On the metallicity of open clusters. III. Homogenised sample. *A&A*, 585:A150, Jan. 2016. doi:10.1051/0004-6361/201526370. → pages 63, 65, 69, 70

[94] K. Nomoto. Evolution of 8–10 M_{sun} Stars toward Electron Capture Supernovae. II. Collapse of an O + NE + MG Core. *ApJ*, 322:206, Nov. 1987. doi:10.1086/165716. → page 1

[95] W. Nowotny, S. Höfner, and B. Aringer. Line formation in AGB atmospheres including velocity effects. Molecular line profile variations of long period variables. *A&A*, 514:A35, May 2010. doi:10.1051/0004-6361/200911899. → page 27

[96] K. Ohnaka, G. Weigelt, and K. H. Hofmann. Clumpy dust clouds and extended atmosphere of the AGB star W Hydrae revealed with VLT/SPHERE-ZIMPOL and VLTI/AMBER. II. Time variations between pre-maximum and minimum light. *A&A*, 597:A20, Jan. 2017. doi:10.1051/0004-6361/201629761. → page 27

[97] J. B. Oke and J. E. Gunn. An Efficient Low Resolution and Moderate Resolution Spectrograph for the Hale Telescope. *PASP*, 94:586, June 1982. doi:10.1086/131027. → page 57

[98] J. B. Oke et al. The Keck Low-Resolution Imaging Spectrometer. *PASP*, 107:375, Apr. 1995. doi:10.1086/133562. → page 57

[99] H. Olofsson, D. González Delgado, F. Kerschbaum, and F. L. Schöier. Mass loss rates of a sample of irregular and semiregular M-type AGB-variables. *A&A*, 391:1053–1067, Sept. 2002. doi:10.1051/0004-6361:20020841. → page 27

[100] E. M. O'Malley, C. Gilligan, and B. Chaboyer. Absolute Ages and Distances of 22 GCs Using Monte Carlo Main-sequence Fitting. *ApJ*, 838 (2):162, Apr. 2017. doi:10.3847/1538-4357/aa6574. → page 23

[101] B. Paxton et al. Modules for Experiments in Stellar Astrophysics (MESA). *ApJS*, 192(1):3, Jan. 2011. doi:10.1088/0067-0049/192/1/3. → pages 3, 36

[102] B. Paxton et al. Modules for Experiments in Stellar Astrophysics (MESA): Planets, Oscillations, Rotation, and Massive Stars. *ApJS*, 208(1):4, Sept. 2013. doi:10.1088/0067-0049/208/1/4. → pages 3, 36

[103] B. Paxton et al. Modules for Experiments in Stellar Astrophysics (MESA): Binaries, Pulsations, and Explosions. *ApJS*, 220(1):15, Sept. 2015. doi:10.1088/0067-0049/220/1/15. → pages 3, 36

[104] B. Paxton et al. Modules for Experiments in Stellar Astrophysics (MESA): Convective Boundaries, Element Diffusion, and Massive Star Explosions. *ApJS*, 234(2):34, Feb. 2018. doi:10.3847/1538-4365/aaa5a8. → pages 3, 36

[105] B. Paxton et al. Modules for Experiments in Stellar Astrophysics (MESA): Convective Boundaries, Element Diffusion, and Massive Star Explosions. *ApJS*, 234(2):34, Feb. 2018. doi:10.3847/1538-4365/aaa5a8. → pages 3, 36

[106] M. Prišegen et al. White dwarf-open cluster associations based on Gaia DR2. *A&A*, 645:A13, Jan. 2021. doi:10.1051/0004-6361/202039276. → page 2

[107] C. Pryor and G. Meylan. Velocity Dispersions for Galactic Globular Clusters. In S. G. Djorgovski and G. Meylan, editors, *Structure and Dynamics of Globular Clusters*, volume 50 of *Astronomical Society of the Pacific Conference Series*, page 357, Jan. 1993. → page 23

[108] S. Rappaport et al. Discovery of Two New Thermally Bloated Low-Mass White Dwarfs Among the Kepler Binaries. *ApJ*, 803(2):82, Apr. 2015. doi:10.1088/0004-637X/803/2/82. → page 19

[109] G. Rau et al. The adventure of carbon stars. Observations and modeling of a set of C-rich AGB stars. *A&A*, 600:A92, Apr. 2017. doi:10.1051/0004-6361/201629337. → page 27

[110] H. B. Richer, G. G. Fahlman, J. Rosvick, and R. Ibata. The White Dwarf Cooling Age of M67. *ApJL*, 504(2):L91–L94, Sept. 1998. doi:10.1086/311586. → page 25

[111] H. B. Richer et al. A Massive Magnetic Helium Atmosphere White Dwarf Binary in a Young Star Cluster. *ApJ*, 880(2):75, Aug. 2019. doi:10.3847/1538-4357/ab2874. → page 2

[112] H. B. Richer et al. Massive White Dwarfs in Young Star Clusters. *ApJ*, 912 (2):165, May 2021. doi:10.3847/1538-4357/abdeb7. → pages v, 2, 23, 25, 86

[113] M. Riello et al. Gaia Early Data Release 3. Photometric content and validation. *A&A*, 649:A3, May 2021. doi:10.1051/0004-6361/202039587. → pages 30, 31

[114] A. D. Romero, F. Campos, and S. O. Kepler. The age-metallicity dependence for white dwarf stars. *MNRAS*, 450(4):3708–3723, July 2015. doi:10.1093/mnras/stv848. → page 36

[115] D. M. Rowan, M. A. Tucker, B. J. Shappee, and J. J. Hermes. Detections and constraints on white dwarf variability from time-series GALEX observations. *MNRAS*, 486(4):4574–4589, July 2019. doi:10.1093/mnras/stz1116. → page 37

[116] M. Salaris and L. R. Bedin. A Gaia DR2 view of white dwarfs in the Hyades. *MNRAS*, 480(3):3170–3176, Nov. 2018. doi:10.1093/mnras/sty2096. → page 25

[117] M. Salaris and S. Cassisi. *Evolution of Stars and Stellar Populations*. Wiley-VCH, 2005. → page 3

[118] M. Salaris, L. G. Althaus, and E. García-Berro. Comparison of theoretical white dwarf cooling timescales. *A&A*, 555:A96, July 2013. doi:10.1051/0004-6361/201220622. → page 36

[119] E. Schatzman. Spectrum of White Dwarfs. *Nature*, 161(4080):61–62, Jan. 1948. doi:10.1038/161061b0. → pages 17, 33

[120] D. Scilla. Introduction to stellar evolution. In *Journal of Physics Conference Series*, volume 703 of *Journal of Physics Conference Series*, page 012002, Apr. 2016. doi:10.1088/1742-6596/703/1/012002. → pages 3, 7, 19

[121] A. M. Serenelli and S. Basu. Determining the Initial Helium Abundance of the Sun. *ApJ*, 719(1):865–872, Aug. 2010. doi:10.1088/0004-637X/719/1/865. → page 3

[122] L. Siess. Evolution of massive AGB stars. I. Carbon burning phase. *A&A*, 448(2):717–729, Mar. 2006. doi:10.1051/0004-6361:20053043. → page 19

[123] L. Siess. Evolution of massive AGB stars. II. model properties at non-solar metallicity and the fate of Super-AGB stars. *A&A*, 476(2):893–909, Dec. 2007. doi:10.1051/0004-6361:20078132. → page 36

[124] V. Silva Aguirre. Stellar Evolution and Modelling Stars. In T. L. Campante, N. C. Santos, and M. J. P. F. G. Monteiro, editors, *Asteroseismology and Exoplanets: Listening to the Stars and Searching for*

New Worlds, volume 49 of *Astrophysics and Space Science Proceedings*, page 3, Jan. 2018. doi:10.1007/978-3-319-59315-9_1. → pages 5, 6

[125] C. Soubiran et al. Open cluster kinematics with Gaia DR2. *A&A*, 619: A155, Nov. 2018. doi:10.1051/0004-6361/201834020. → page 23

[126] P. B. Stetson. Homogeneous Photometry for Star Clusters and Resolved Galaxies. II. Photometric Standard Stars. *PASP*, 112(773):925–931, July 2000. doi:10.1086/316595. → page 31

[127] P. N. Stewart et al. The weather report from IRC+10216: evolving irregular clouds envelop carbon star. *MNRAS*, 455(3):3102–3109, Jan. 2016. doi:10.1093/mnras/stv2454. → page 27

[128] J. Su et al. New ZZ Ceti Stars from the LAMOST Survey. *ApJ*, 847(1):34, Sept. 2017. doi:10.3847/1538-4357/aa88a8. → page 37

[129] K. D. Temmink et al. Looks can be deceiving. Underestimating the age of single white dwarfs due to binary mergers. *A&A*, 636:A31, Apr. 2020. doi:10.1051/0004-6361/201936889. → pages 80, 82

[130] D. Tody. The IRAF Data Reduction and Analysis System. In D. L. Crawford, editor, *Instrumentation in astronomy VI*, volume 627 of *Society of Photo-Optical Instrumentation Engineers (SPIE) Conference Series*, page 733, Jan. 1986. doi:10.1117/12.968154. → page 55

[131] S. Toonen, M. Hollands, B. T. Gänsicke, and T. Boekholt. The binarity of the local white dwarf population. *A&A*, 602:A16, June 2017. doi:10.1051/0004-6361/201629978. → page 26

[132] P. E. Tremblay, P. Bergeron, and A. Gianninas. An Improved Spectroscopic Analysis of DA White Dwarfs from the Sloan Digital Sky Survey Data Release 4. *ApJ*, 730(2):128, Apr. 2011. doi:10.1088/0004-637X/730/2/128. → pages xiv, 35, 66

[133] P. E. Tremblay et al. Core crystallization and pile-up in the cooling sequence of evolving white dwarfs. *Nature*, 565(7738):202–205, Jan. 2019. doi:10.1038/s41586-018-0791-x. → page 16

[134] D. Veras, Z. M. Leinhardt, A. Bonsor, and B. T. Gänsicke. Formation of planetary debris discs around white dwarfs - I. Tidal disruption of an extremely eccentric asteroid. *MNRAS*, 445(3):2244–2255, Dec. 2014. doi:10.1093/mnras/stu1871. → page 18

[135] V. Weidemann. Mass loss towards the white dwarf stage. *A&A*, 59(3): 411–418, Aug. 1977. → page 25

[136] V. Weidemann and D. Koester. The upper mass limit for white dwarf progenitors and the initial-final mass relation for low and intermediate mass stars. *A&A*, 121:77–84, May 1983. → pages 1, 82

[137] V. Weidemann, S. Jordan, J. Iben, Icko, and S. Casertano. White Dwarfs in the Halo of the Hyades Cluster: The Case of the Missing White Dwarfs. *AJ*, 104:1876, Nov. 1992. doi:10.1086/116364. → page 25

[138] K. Werner. On the Balmer Line Problem. *ApJL*, 457:L39, Jan. 1996. doi:10.1086/309889. → page 35

[139] K. A. Williams and M. Bolte. A Photometric and Spectroscopic Search for White Dwarfs in the Open Clusters NGC 6633 and NGC 7063. *AJ*, 133(4): 1490–1504, Apr. 2007. doi:10.1086/511675. → page 25

[140] M. Wittkowski et al. Aperture synthesis imaging of the carbon AGB star R Sculptoris. Detection of a complex structure and a dominating spot on the stellar disk. *A&A*, 601:A3, May 2017. doi:10.1051/0004-6361/201630214. → page 27

[141] D. G. York et al. The Sloan Digital Sky Survey: Technical Summary. *AJ*, 120(3):1579–1587, Sept. 2000. doi:10.1086/301513. → page 20

[142] J. Ziółkowski and A. A. Zdziarski. The nature of the Schönberg-Chandrasekhar limit. *MNRAS*, 499(4):4832–4837, Dec. 2020. doi:10.1093/mnras/staa3088. → page 8

Appendix A

Supporting Materials

Here we include the full results of the wide search described in Sec. 3.1.

Table A.1. Wide Search Escapee Candidates

Cluster	Gaia DR2 Source ID	M_G [mag]	$(Bp-Rp)_0$	Dist. [Cl_{rad}]	Mass [$M_\odot$]			Cooling Age [Myr]		
					Est.	Upper	Lower	Est.	Upper	Lower
(1)	(2)	(3)	(4)	(5)	(6)	(7)	(8)	(9)	(10)	(11)
Alessi 5	5352954771936845440	11.02	-0.51	18.04	1.07	> 1.28	0.81	55.48	...	89.14
Alessi 8	5887666586717940224	10.07	-0.48	16.18	0.69	0.93	0.53	10.55	3.14	18.92
	5982381370178315904	9.95	-0.73	9.50	>1.28	>1.28	1.13	...	...	0.14
Alessi 12	1762939111272873216	11.08	-0.58	16.10	1.20	>1.28	1.06	6.55	...	68.19
	1805484267034684672	10.98	-0.30	19.39	0.68	0.87	0.50	98.47	74.50	136.19
	1817445136772265856	11.20	-0.27	6.22	0.72	0.95	0.50	142.19	101.40	198.14
	1832754079548398848	11.22	-0.35	10.54	0.85	1.00	0.70	120.30	98.30	150.07
	1840424272662732544	11.36	-0.20	16.57	0.67	0.94	0.46	203.37	136.24	290.33
	1847749287845442176	11.21	-0.34	17.46	0.85	1.02	0.67	120.86	95.56	156.95
	1862286485141695104	11.29	-0.43	14.03	1.01	1.17	0.82	108.81	50.06	143.76
	1865111023126770560	10.68	-0.48	19.45	0.90	1.06	0.76	39.81	22.95	44.38
	1865156034384396672	10.89	-0.55	19.35	1.10	1.25	0.97	18.12	0.17	58.36
Alessi 19	4376049337883929984	10.43	-0.40	17.70	0.64	0.92	0.44	27.70	18.68	56.15
	4468178417905732864	10.78	-0.41	14.45	0.80	1.18	0.48	53.28	0.68	99.17
	4470497631525396864	10.64	-0.35	10.21	0.64	0.98	0.39	49.12	32.76	103.30
	4477802370166728192	10.13	-0.47	7.24	0.68	1.12	0.43	12.11	0.25	33.54
	4480180961719293056	11.16	-0.25	4.28	0.66	1.08	0.36	143.71	69.92	268.44
	4480191681947797632	11.01	-0.12	4.00	0.42	0.79	0.25	176.59	90.46	280.19
	4480458519688606848	10.31	-0.33	3.15	0.49	0.76	0.31	35.59	16.04	96.42
	4482142280001910400	10.63	-0.87	3.09	>1.28	>1.28	>1.28	...	...	...
	4484494994368242944	10.74	-0.32	1.34	0.62	0.88	0.41	64.99	46.48	113.69
	4486590599105841408	10.80	-0.39	14.05	0.76	1.06	0.51	58.71	35.23	94.01
	4499995393896134400	10.82	-0.46	9.98	0.91	>1.28	0.59	53.48	...	81.83
	4502033686597154560	10.62	-0.38	8.04	0.69	0.88	0.52	42.18	34.92	61.96
	4507419403783827584	10.84	-0.30	10.25	0.62	1.00	0.35	82.25	50.79	173.90
	4508142156589768448	10.87	-0.32	4.76	0.67	0.91	0.47	79.31	58.98	121.61
	4508653399438645632	10.52	-0.57	4.83	1.07	>1.28	0.79	7.16	...	28.47
	4510989208806897792	10.74	-0.39	10.80	0.74	>1.28	0.26	52.32	...	209.78
	4527635157714872960	11.24	-0.36	11.90	0.88	1.08	0.66	120.64	78.70	167.26
	4535822945927846528	10.73	-0.37	18.10	0.71	0.95	0.51	53.73	42.60	81.90
	4537315605983651072	10.95	-0.43	20.25	0.90	1.14	0.66	69.10	10.99	96.18
	4549137859941184256	10.53	-0.50	15.59	0.89	1.13	0.68	26.39	0.64	33.07
	4549299821847911680	10.58	-0.41	16.56	0.72	0.99	0.51	35.17	25.39	57.45
	4551088943325443712	11.13	-0.33	12.71	0.80	0.98	0.62	112.27	88.04	147.45
	4575935024190275328	10.53	-0.46	13.84	0.81	1.06	0.61	28.91	11.53	39.15
	4576926710662025472	10.92	-0.27	14.98	0.60	0.77	0.46	100.42	76.99	137.91
	4580243696729381888	10.93	-0.25	18.05	0.58	0.78	0.41	107.69	77.56	156.51
Alessi 21	2949405787932448384	11.16	-0.46	11.22	1.04	1.20	0.84	86.94	11.50	110.89
	2951717579847688960	10.28	-0.63	18.55	1.18	>1.28	1.00	0.14	...	4.95
	2953180617506290048	11.07	-0.31	10.96	0.74	1.03	0.48	108.61	75.60	168.00
	3028302962770764416	11.23	-0.49	17.03	1.08	1.27	0.89	79.62	1.33	116.93
	3033651678824971264	11.37	-0.47	12.00	1.08	1.26	0.90	103.91	13.29	145.36
	3041793008368326784	10.99	-0.37	16.80	0.81	1.15	0.48	82.98	11.56	143.64
	3045185929454409856	11.38	-0.54	6.26	1.17	>1.28	1.00	66.59	...	127.50
	3047918903045538944	10.01	-0.57	1.91	0.91	1.08	0.75	2.78	0.34	7.34
	3049634312983990272	11.20	-0.45	4.33	1.02	>1.28	0.69	94.28	...	148.66
	3049898092693361792	10.96	-0.47	5.19	0.98	1.21	0.74	65.90	0.92	86.77
	3050876554961550848	11.19	-0.57	6.37	1.20	>1.28	0.96	14.96	...	99.89
	3052133335414358784	11.00	-0.37	4.80	0.81	1.07	0.56	83.94	47.89	125.61

Table A.1 (cont'd)

Cluster	Gaia DR2 Source ID	M_G [mag]	$(Bp-Rp)_0$	Dist. [Cl_{rad}]	Mass [$M_\odot$]			Cooling Age [Myr]		
					Est.	Upper	Lower	Est.	Upper	Lower
(1)	(2)	(3)	(4)	(5)	(6)	(7)	(8)	(9)	(10)	(11)
	3057432667921034752	11.05	-0.36	19.56	0.81	0.98	0.63	95.38	77.24	123.25
	3058657901831394432	10.58	-0.45	12.06	0.80	1.05	0.60	32.78	18.17	44.64
	3099313168902595840	10.93	-0.40	9.98	0.85	1.07	0.63	71.17	41.47	98.10
	3102498320947143296	11.32	-0.68	12.89	>1.28	>1.28	0.95	…	…	124.89
	3103735576466830208	11.18	-0.32	16.32	0.79	1.13	0.46	122.97	47.09	209.30
Alpha Per	408144424247559680	9.36	-0.61	4.77	0.92	>1.28	0.86	0.25	…	0.34
ASCC 113	1853507876918946432	11.04	-0.32	15.50	0.73	1.01	0.48	103.66	73.22	159.69
	1854288087800311552	11.25	-0.22	13.13	0.65	0.82	0.51	172.22	134.56	215.47
	1858474645820394240	11.28	-0.47	19.95	1.07	1.22	0.90	95.91	19.86	125.86
	1866829323581231616	11.11	-0.43	10.75	0.96	1.16	0.75	86.39	26.02	115.41
	1866921476396272256	11.22	-0.20	9.91	0.60	0.78	0.46	175.59	134.40	226.94
	1867163472040641280	11.02	-0.24	8.21	0.58	0.84	0.39	125.11	84.63	191.35
	1867327471071322240	10.10	-0.63	8.82	>1.28	>1.28	0.94	…	…	3.25
	1870421359346313088	11.42	-0.17	15.49	0.65	0.90	0.46	227.16	157.65	311.00
	1949768165721708544	11.57	-0.44	19.61	1.08	>1.28	0.86	140.33	…	216.22
	1963968770715879680	11.51	-0.33	4.31	0.93	1.13	0.68	175.97	110.07	253.51
	1965199570908941568	11.36	-0.30	2.60	0.83	1.14	0.50	159.50	77.12	262.13
	2064173102208150912	11.27	-0.30	17.38	0.79	1.07	0.53	144.65	93.15	216.48
	2064364623389656576	11.44	-0.20	14.27	0.71	0.99	0.49	218.18	144.12	311.61
	2067097223322941184	11.12	-0.21	15.66	0.59	0.76	0.45	151.58	115.74	198.42
	2067450024818993152	11.17	-0.32	20.00	0.80	1.09	0.50	119.60	63.95	188.70
	2068194806504634240	11.17	-0.38	18.33	0.90	1.21	0.57	103.97	9.49	170.87
Collinder 121	2899802695231620992	10.60	-0.44	10.12	0.78	1.09	0.52	35.12	3.03	58.88
	2921327769947744000	10.47	-0.54	3.04	0.99	>1.28	0.70	16.61	…	26.93
	2924675400598744704	10.70	-0.49	5.85	0.94	1.21	0.69	40.16	0.28	51.74
	3033651678824971264	10.36	-0.49	19.56	0.81	1.14	0.56	17.43	0.29	30.14
	5584168976198163328	10.77	-0.41	9.69	0.79	1.16	0.48	52.55	0.90	95.60
	5588351484074655232	10.36	-0.68	18.58	>1.28	>1.28	1.03	…	…	5.42
	5608976535503258496	10.44	-0.50	6.37	0.86	>1.28	0.44	21.11	…	57.76
	5609238734667240064	9.96	-0.73	8.24	>1.28	>1.28	1.09	…	…	0.24
	5610515714344370560	10.31	-0.56	5.26	0.99	>1.28	0.66	6.34	…	19.63
	5610628139404763904	10.60	-0.41	4.31	0.73	1.19	0.40	37.68	0.28	92.06
	5611082753112158976	10.06	-0.49	5.06	0.70	1.07	0.49	9.78	0.55	22.39
	5613411170843319168	9.53	-0.76	10.83	>1.28	>1.28	>1.28	…	…	…
	5616150058598869248	10.70	-0.72	8.19	>1.28	>1.28	0.52	…	…	74.95
	5616446858022119936	10.50	-0.58	7.63	1.08	>1.28	0.67	5.24	…	31.37
	5717606115367003136	10.51	-0.46	18.60	0.80	1.12	0.54	27.46	0.68	45.75
Collinder 132	2892194903699687552	10.57	-0.45	18.10	0.80	1.20	0.49	32.27	0.24	60.55
	2924675400598744704	11.14	-0.46	19.21	1.01	1.20	0.80	85.78	9.61	112.91
	5511212943722649344	10.57	-0.40	19.99	0.70	1.06	0.43	36.22	13.69	77.32
	5511542792916930048	10.79	-0.30	20.03	0.60	1.18	0.28	74.35	0.70	214.71
	5546969680338155136	10.45	-0.56	19.63	1.04	>1.28	0.72	9.42	…	25.46
	5559843823326236416	10.62	-0.48	19.26	0.88	>1.28	0.54	34.70	…	58.93
	5559937350535040384	10.64	-0.43	18.11	0.79	1.09	0.54	38.92	7.93	61.81
	5584168976198163328	11.20	-0.37	11.61	0.90	1.17	0.59	110.92	35.35	173.20
	5584360119422916736	10.58	-0.41	11.76	0.71	1.13	0.40	35.74	0.79	85.47
	5588351484074655232	10.79	-0.64	6.60	>1.28	>1.28	1.05	…	…	39.18
	5589923235942686848	10.68	-0.59	6.25	1.15	>1.28	0.87	0.71	…	39.91
	5595074928959659136	10.63	-0.47	8.08	0.87	>1.28	0.57	35.69	…	55.97

Table A.1 (cont'd)

Cluster	Gaia DR2 Source ID	M_G [mag]	$(Bp-Rp)_0$	Dist. [Cl_{rad}]	Mass [$M_\odot$]			Cooling Age [Myr]		
					Est.	Upper	Lower	Est.	Upper	Lower
(1)	(2)	(3)	(4)	(5)	(6)	(7)	(8)	(9)	(10)	(11)
	5597663797814959488	11.10	-0.47	14.92	1.02	>1.28	0.61	80.10	…	138.66
	5597782441987499520	10.60	-0.54	12.41	1.02	>1.28	0.71	23.77	…	38.05
	5604794508666591232	10.91	-0.37	1.04	0.77	1.18	0.43	74.58	2.02	145.95
	5605936450274462208	9.78	-0.57	3.43	0.84	1.08	0.65	2.46	0.23	7.21
	5606544450148104576	10.87	-0.49	3.81	0.98	>1.28	0.69	54.91	…	76.05
	5608976535503258496	10.88	-0.46	10.45	0.94	>1.28	0.53	58.63	…	105.08
	5609238734667240064	10.39	-0.69	5.47	>1.28	>1.28	1.08	…	…	2.74
	5610515714344370560	10.74	-0.52	8.05	1.02	>1.28	0.75	38.25	…	52.28
	5611516884103827328	10.03	-0.51	3.62	0.74	1.04	0.54	8.16	0.63	16.41
	5613261190584162048	10.36	-0.58	7.52	1.06	>1.28	0.73	3.80	…	19.67
	5614341602495158144	10.43	-0.57	12.26	1.05	>1.28	0.59	6.70	…	32.05
	5618530084662423808	10.33	-0.52	11.58	0.87	1.09	0.69	14.21	1.45	19.13
	5644308826265337600	10.90	-0.39	19.92	0.82	1.10	0.54	69.27	18.04	107.95
	5697651426736462592	11.23	-0.38	18.07	0.91	1.21	0.58	113.96	16.22	185.37
	5710639373476492032	10.85	-0.55	14.30	1.09	>1.28	0.81	16.11	…	61.74
IC 2391	5317454079808243456	11.19	-0.50	4.73	1.08	1.16	1.01	71.72	36.65	93.01
NGC 2422	3028302962770764416	11.51	-0.54	7.17	1.19	>1.28	1.05	80.04	…	141.78
	3028924221197888768	11.78	-0.41	10.09	1.10	>1.28	0.87	186.51	…	297.74
	3028937037380440448	11.41	-0.37	9.43	0.97	1.10	0.79	142.38	100.77	185.62
	3029069940849870720	11.59	-0.35	5.43	0.99	1.17	0.76	181.28	115.45	257.71
	3030482160458326784	11.47	-0.22	7.82	0.74	1.00	0.53	218.32	149.11	305.02
	3030544832620996224	11.62	-0.31	12.43	0.94	1.09	0.75	204.09	146.06	270.58
	3031106030224132608	11.85	-0.46	16.85	1.17	>1.28	1.01	181.18	…	265.69
	3033489943235297280	11.80	-0.35	12.45	1.06	1.26	0.79	221.09	93.50	343.38
	3033552443600454784	11.65	-0.39	15.02	1.06	1.23	0.85	172.65	85.80	250.48
	3039980222933652096	11.74	-0.30	16.81	0.97	1.15	0.74	238.22	158.18	337.64
NGC 2451B	5428728474760340352	11.97	-0.62	20.18	>1.28	>1.28	1.21	…	…	191.38
	5532546561683429888	12.06	-0.66	5.81	>1.28	>1.28	1.18	…	…	236.79
	5534595188067100032	11.36	-0.55	4.92	1.19	>1.28	1.05	52.67	…	113.83
	5551243031058471808	11.68	-0.62	18.19	>1.28	>1.28	1.13	…	…	150.11
	5575674041987286400	11.93	-0.63	13.00	>1.28	>1.28	1.12	…	…	223.55
	5591693965064811776	11.53	-0.57	5.66	1.24	>1.28	1.09	49.38	…	131.09
	5609107476168766848	11.45	-0.72	15.74	>1.28	>1.28	>1.28	…	…	…
	5610083052220844800	11.69	-0.51	14.04	1.20	>1.28	1.07	122.13	…	176.88
	5616906690102297600	11.34	-0.48	15.95	1.08	1.18	1.00	95.11	52.19	118.99
	5694411367829835136	11.40	-0.50	15.54	1.12	1.23	1.05	89.61	34.10	121.00
NGC 2516	5276965113864595200	11.35	-0.37	18.39	0.94	1.04	0.83	134.49	116.51	156.50
	5289447182180342016	11.23	-0.24	5.94	0.68	0.82	0.56	158.61	129.12	193.08
	5290719287073728128	11.13	-0.30	0.72	0.73	0.85	0.62	122.89	103.82	146.34
	5290834387897642624	10.89	-0.35	1.21	0.73	0.87	0.60	75.76	63.63	93.87
	5294015515555860608	11.18	-0.42	5.92	0.96	1.11	0.78	96.54	55.12	123.77
	5294686526884585600	11.92	-0.28	11.52	1.01	1.15	0.81	295.28	207.13	403.04
NGC 5662	5879516284965902720	9.72	-0.49	18.81	0.57	0.98	0.38	9.09	0.52	25.42
NGC 6025	5829676281875471616	10.07	-0.71	17.65	>1.28	>1.28	0.85	…	…	5.71
	5832578511570131200	10.49	-0.54	14.82	0.99	>1.28	0.36	17.71	…	92.64
NGC 7063	1963968770715879680	11.00	-0.40	17.41	0.87	1.15	0.58	78.65	11.45	121.65
Pismis 4	5329969103416108032	10.99	-0.31	11.71	0.70	0.98	0.47	97.66	69.90	151.42
	5331602526709717760	10.88	-0.36	18.30	0.74	1.05	0.48	73.41	47.24	122.13
	5525116852370580864	11.00	-0.38	13.72	0.83	1.18	0.49	82.20	5.70	143.64

Table A.1 (cont'd)

Cluster	Gaia DR2 Source ID	M_G [mag]	$(Bp-Rp)_0$	Dist. [Cl_{rad}]	Mass [$M_\odot$]			Cooling Age [Myr]		
					Est.	Upper	Lower	Est.	Upper	Lower
(1)	(2)	(3)	(4)	(5)	(6)	(7)	(8)	(9)	(10)	(11)
Pleiades	66697547870378368	10.74	-0.53	1.53	1.03	1.06	1.00	37.52	29.21	40.65
vdB Hagen 164	5795934499101239552	10.55	-0.53	13.22	0.98	1.17	0.80	24.05	0.35	30.79
	5823612299144570368	10.54	-0.72	9.71	>1.28	>1.28	>1.28	...	...	...
	5823613334236349568	11.09	-0.52	9.49	1.09	>1.28	0.90	52.41	...	88.91

Notes. As in Tab. 3.2, but for all of the 151 candidate escapee WDs identified in wide search.

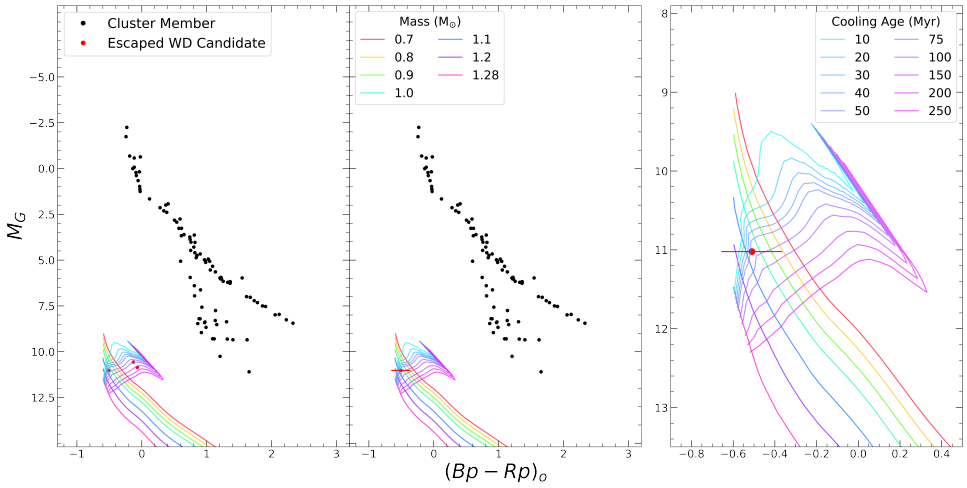

Figure A.1: As in Fig. 3.3, but for Alessi 5.

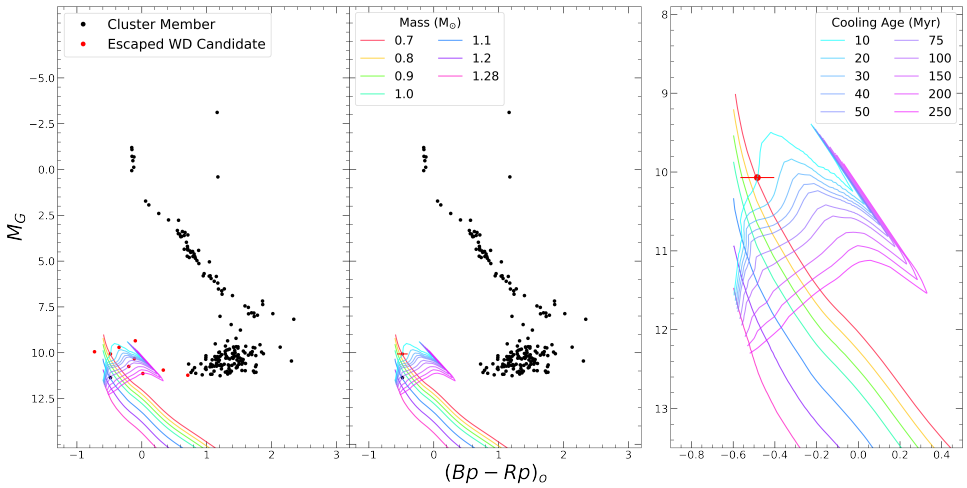

Figure A.2: As in Fig. 3.3, but for Alessi 8.

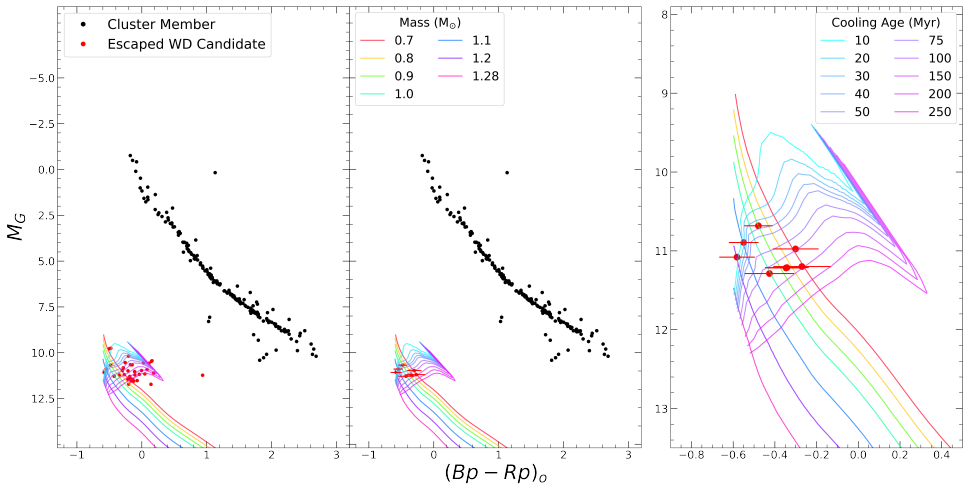

Figure A.3: As in Fig. 3.3, but for Alessi 12.

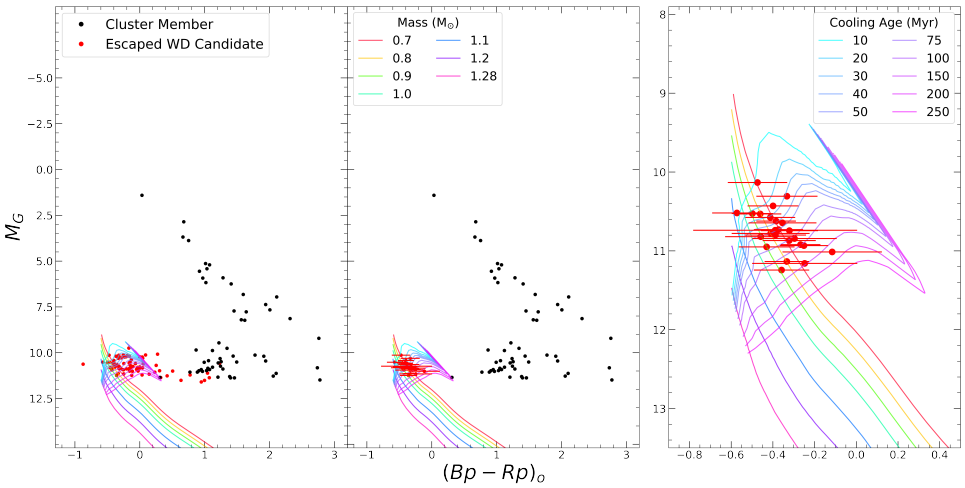

Figure A.4: As in Fig. 3.3, but for Alessi 19.

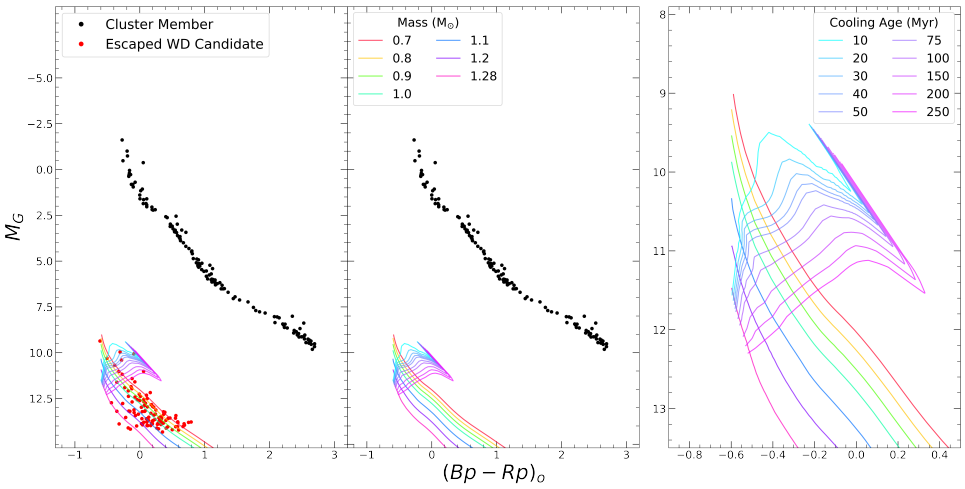

Figure A.5: As in Fig. 3.3, but for Alpha Persei.

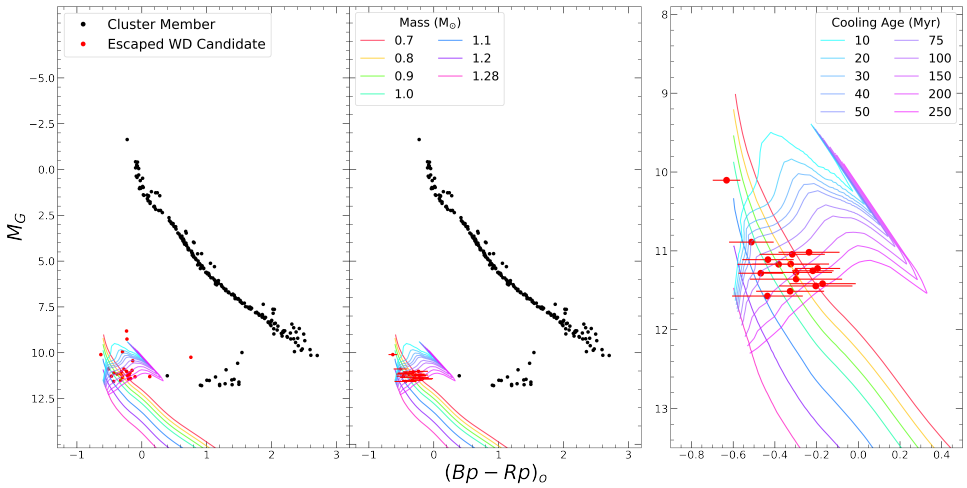

Figure A.6: As in Fig. 3.3, but for ASCC 113.

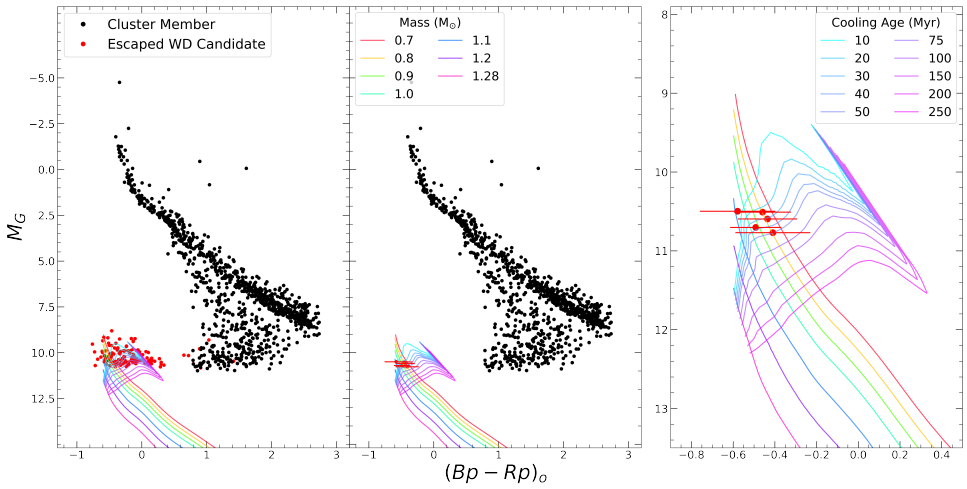

Figure A.7: As in Fig. 3.3, but for Collinder 121.

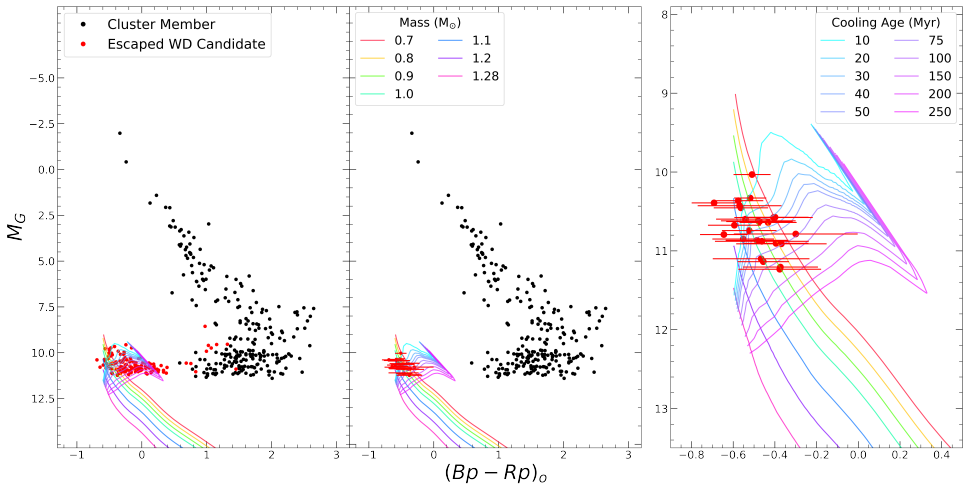

Figure A.8: As in Fig. 3.3, but for Collinder 132.

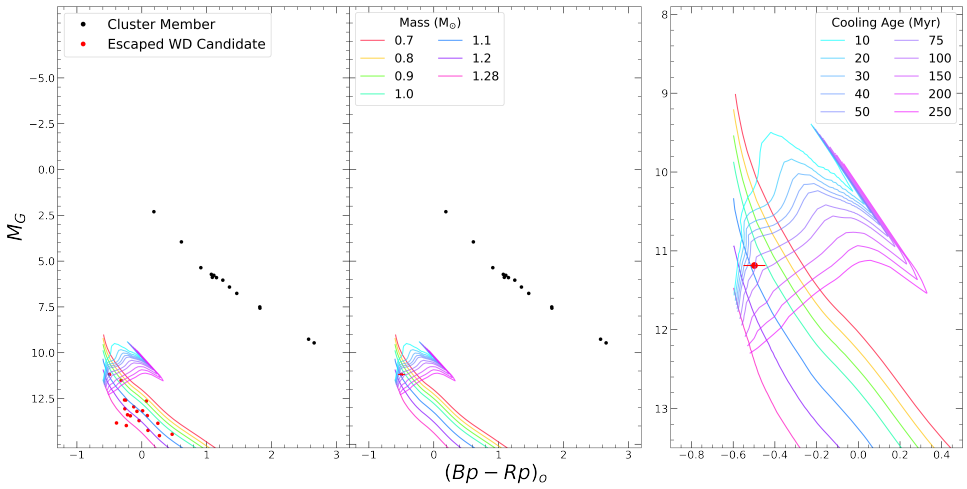

Figure A.9: As in Fig. 3.3, but for IC 2391.

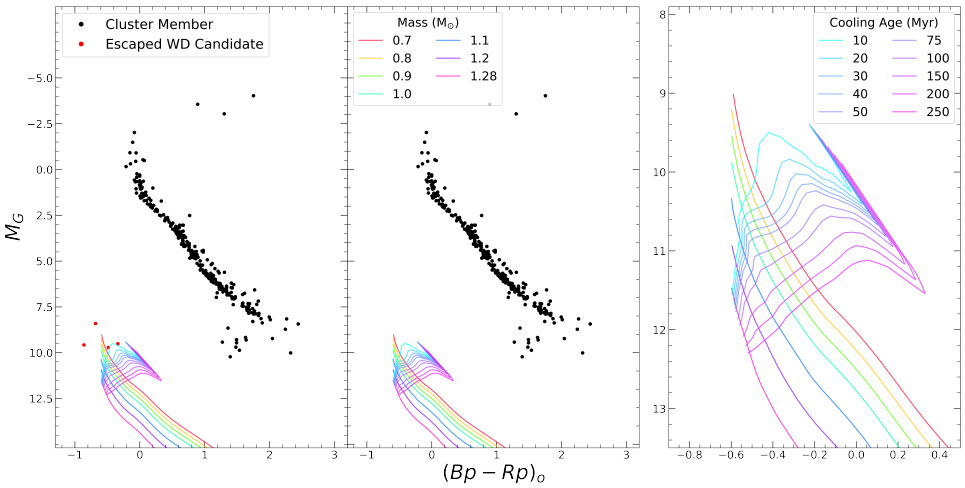

Figure A.10: As in Fig. 3.3, but for NGC 5662.

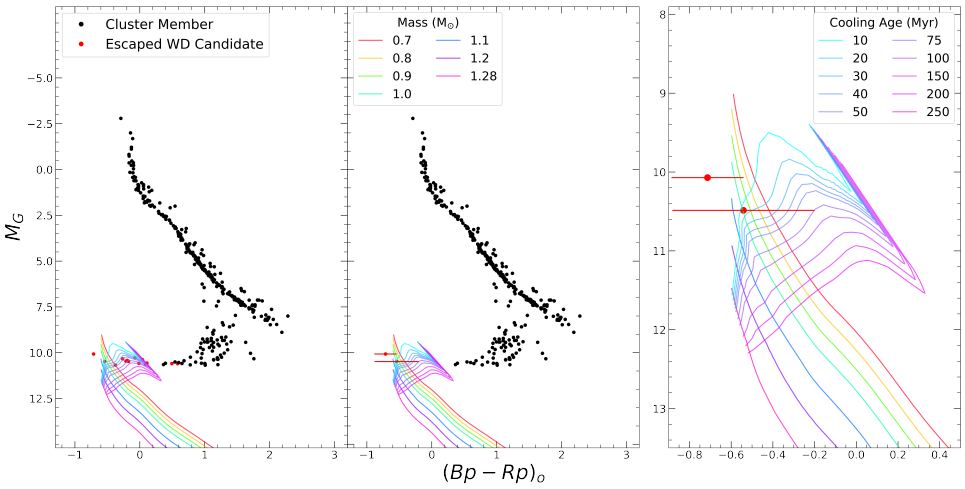

Figure A.11: As in Fig. 3.3, but for NGC 6025.

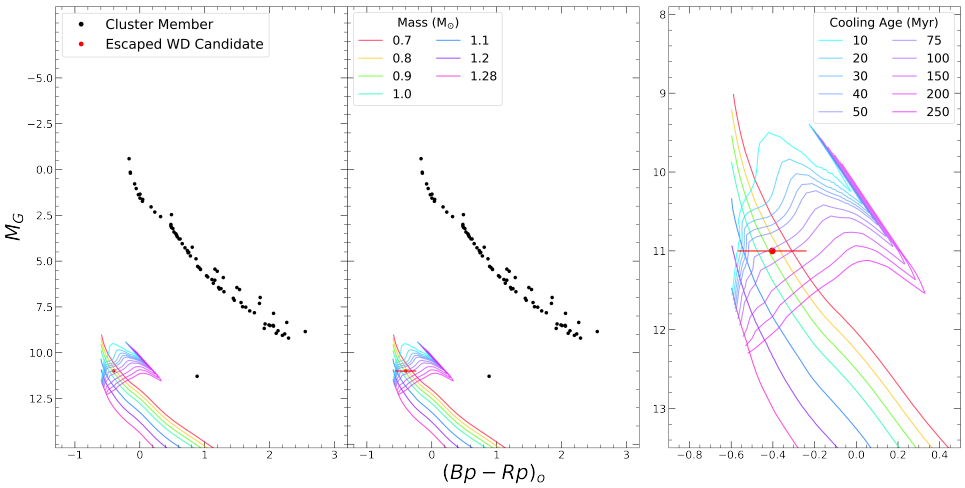

Figure A.12: As in Fig. 3.3, but for NGC 7063.

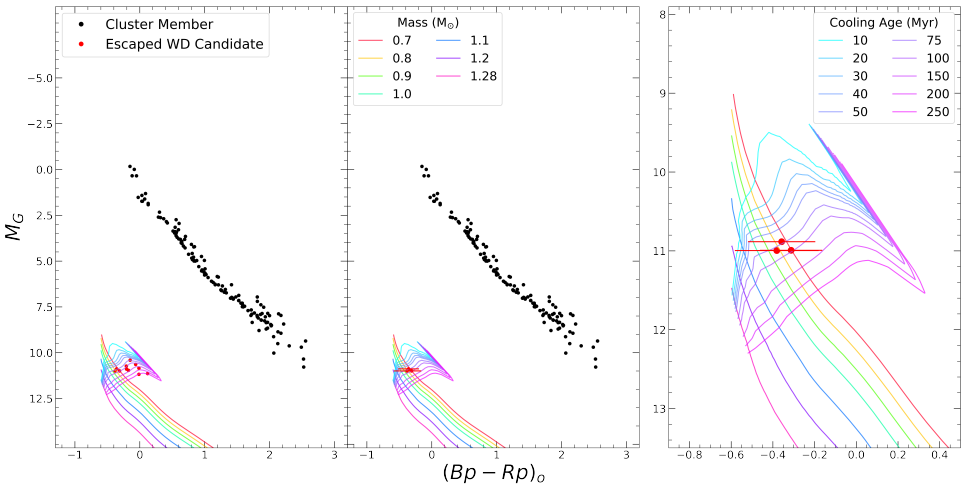

Figure A.13: As in Fig. 3.3, but for Pismis 4.

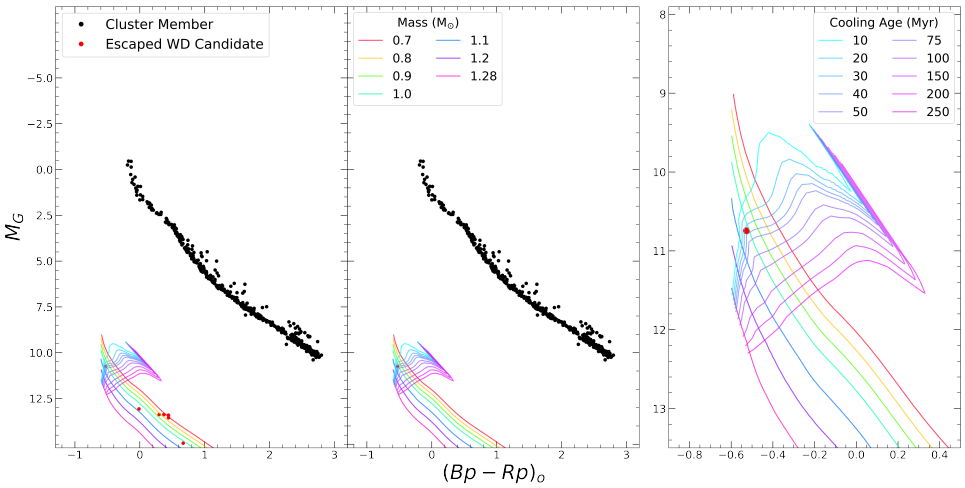

Figure A.14: As in Fig. 3.3, but for Pleiades.

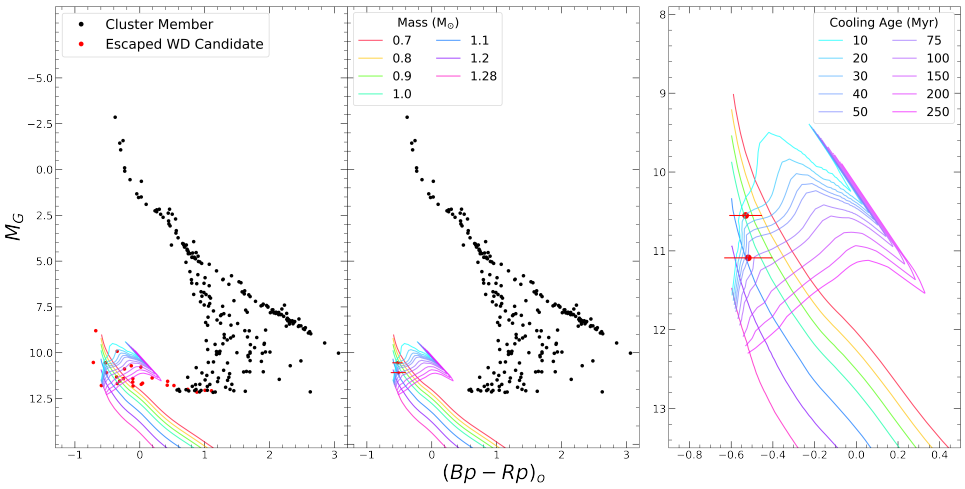

Figure A.15: As in Fig. 3.3, but for vdB Hagen 164.